

AWARD NUMBER: W81XWH-13-1-0288

TITLE: Microenvironment-Sensitive Multimodal Contrast Agent for Prostate Cancer Diagnosis

PRINCIPAL INVESTIGATOR: Allan E. David

CONTRACTING ORGANIZATION: Auburn University
Auburn AL 36849

REPORT DATE: October 2017

TYPE OF REPORT: Annual

PREPARED FOR: U.S. Army Medical Research and Materiel Command
Fort Detrick, Maryland 21702-5012

DISTRIBUTION STATEMENT: Approved for Public Release;
Distribution Unlimited

The views, opinions and/or findings contained in this report are those of the author(s) and should not be construed as an official Department of the Army position, policy or decision unless so designated by other documentation.

REPORT DOCUMENTATION PAGE				Form Approved OMB No. 0704-0188	
Public reporting burden for this collection of information is estimated to average 1 hour per response, including the time for reviewing instructions, searching existing data sources, gathering and maintaining the data needed, and completing and reviewing this collection of information. Send comments regarding this burden estimate or any other aspect of this collection of information, including suggestions for reducing this burden to Department of Defense, Washington Headquarters Services, Directorate for Information Operations and Reports (0704-0188), 1215 Jefferson Davis Highway, Suite 1204, Arlington, VA 22202-4302. Respondents should be aware that notwithstanding any other provision of law, no person shall be subject to any penalty for failing to comply with a collection of information if it does not display a currently valid OMB control number. PLEASE DO NOT RETURN YOUR FORM TO THE ABOVE ADDRESS.					
1. REPORT DATE October 2017		2. REPORT TYPE Annual		3. DATES COVERED 9Sep2016 - 8Sep2017	
4. TITLE AND SUBTITLE Microenvironment-Sensitive Multimodal Contrast Agent for Prostate Cancer Diagnosis				5a. CONTRACT NUMBER	
				5b. GRANT NUMBER W81XWH-13-1-0288	
				5c. PROGRAM ELEMENT NUMBER	
6. AUTHOR(S) Allan E. David E-Mail: aedavid@auburn.edu				5d. PROJECT NUMBER	
				5e. TASK NUMBER	
				5f. WORK UNIT NUMBER	
7. PERFORMING ORGANIZATION NAME(S) AND ADDRESS(ES) Auburn University 107 Samford Hall Auburn AL 36849-0001				8. PERFORMING ORGANIZATION REPORT NUMBER	
9. SPONSORING / MONITORING AGENCY NAME(S) AND ADDRESS(ES) U.S. Army Medical Research and Materiel Command Fort Detrick, Maryland 21702-5012				10. SPONSOR/MONITOR'S ACRONYM(S)	
				11. SPONSOR/MONITOR'S REPORT NUMBER(S)	
12. DISTRIBUTION / AVAILABILITY STATEMENT Approved for Public Release; Distribution Unlimited					
13. SUPPLEMENTARY NOTES					
14. ABSTRACT The goal of this work is to develop the materials and methods to non-invasively monitor the aggressiveness of prostate cancer. Prostate cancer is the second leading cause of death among men in the United States, yet no reliable diagnostic tools or effective therapies are currently available. There is increased focus on the development of tools for improved detection and monitoring of prostate cancer. In this work, we have developed magnetic nanoparticles that are able to detect and bind to PC3 prostate cancer cells. Using the particles' magnetic properties, they can be localized in the body using MRI. The addition of a fluorescent marker on the nanoparticle that is sensitive to proteolytic activity then provides a means to detect and quantify the aggressiveness of the cancer. The feasibility of this system for detection of proteolytic activity has been demonstrated with <i>in vitro</i> studies.					
15. SUBJECT TERMS Prostate cancer, nanomedicine, diagnosis, cancer staging, proteolytic activity; non-invasive detection; MRI					
16. SECURITY CLASSIFICATION OF:			17. LIMITATION OF ABSTRACT Unclassified	18. NUMBER OF PAGES 79	19a. NAME OF RESPONSIBLE PERSON USAMRMC
a. REPORT Unclassified	b. ABSTRACT Unclassified	c. THIS PAGE Unclassified			19b. TELEPHONE NUMBER (include area code)

Table of Contents

	<u>Page</u>
1. Introduction.....	4
2. Keywords.....	4
3. Accomplishments.....	4
4. Impact.....	22
5. Changes/Problems.....	22
6. Products.....	22
7. Participants & Other Collaborating Organizations.....	23
8. Special Reporting Requirements.....	25
9. Appendices.....	25

1. Introduction

Prostate cancer (PCa) is the most diagnosed non-skin malignancy, and the second leading cause of death, among men in the United States. On January 1, 2007 there were approximately 2,276,112 men alive in the United States who had a history of prostate cancer, and 1 in 6 men born today will be diagnosed with prostate cancer during their lifetime. In order to achieve more effective therapy, focus has recently shifted to the early detection of PCa. While prostate-specific antigen (PSA) monitoring has enabled earlier detection of prostate cancer, the high variability in PSA levels has limited its diagnostic value. Additionally, dynamic changes in molecular, cellular and tissue level processes occur during disease progression and remission, and their quantitative assessment is important for treatment planning and monitoring of treatment efficacy. Measurement techniques currently in use (e.g. biopsy) are invasive, and provide limited spatial and temporal sampling. Improved molecular imaging techniques, that are both quantitative and sensitive, and that can detect processes deep within the human body are required to monitor these changes which may be predictors of treatment outcomes. Hence, the need for a non-invasive, highly sensitive and accurate diagnostic tool for measuring the aggressiveness of prostate cancer is both acute and imperative. Taking all these facts into account, the U.S. Preventive Services Task Force (USPSTF) has recommended that, “research is urgently needed to identify new screening methods that can distinguish nonprogressive or slowly progressive disease from disease that is likely to affect the quality or length of life.” Improved molecular imaging techniques, that are both quantitative and sensitive, and that can detect processes deep within the human body are required to monitor these changes which may be predictors of treatment outcomes. The primary objective of this application is to confirm the feasibility of a microenvironment-responsive multimodal contrast agent (MMCA) for non-invasive, 3D measurement of prostate cancer aggressiveness.

2. Keywords

prostate cancer; cancer staging; imaging; MRI; nanomedicine; proteolytic activity; non-invasive detection

3. Accomplishments

The goal of the funded project is to develop multimodal and bioprocess-sensitive “smart” magnetic nanoparticles (MNP) capable of detecting dynamic changes in molecular and tissue level processes that occur during prostate cancer progression. Specifically, we are developing MNPs that respond to and are able to monitor and quantify overexpressed proteolytic activity in the tumor microenvironment. Proteolytic processes have been shown to be important for cancer growth, progression, extracellular matrix remodeling and metastasis. The ability to non-invasively monitor this activity would not only enable better treatment planning, but also provide a means to monitor therapeutic effect. The specific aims of this project are: **Aim 1** – Synthesize the microenvironment responsive multi-modal imaging agent (MMIA) and characterize its physical properties (e.g. magnetic susceptibility, particle size distribution, zeta potential, etc); **Aim 2** – *In vitro* characterization of the target selectivity, protease

specificity, and detection sensitivity of the MMIA using low- and high proteolytic activity cell lines; and **Aim 3** – Conduct a pilot *in vivo* animal study to demonstrate the utility of this system for monitoring tumor progression.

According to our statement of work, the objectives for the period of work to date are:

Task 1 – Synthesis and characterization of the microenvironment-responsive MMIA.

The subtasks to be done included:

- a. Synthesis of the MMIA components
- b. Optimization of MMIA stability
- c. Assembly of the MMIA/fluorescent probe/targeting agent complex
- d. Characterize the physical properties of the MMIA

Task 2 – In vitro characterization of target selectivity, protease specificity, and detection sensitivity. The subtasks to be done included:

- a. Optimization of cancer cell targeting selectivity
- b. Optimization of protease response
- c. Measure selectivity and proteolytic response of MMIA

Task 3 – Pilot in vivo animal study. The subtasks to be done included:

- a. Pharmacokinetics and Biodistribution
- b. Evaluation of proteolytic activity

The accomplishments for each of these subtasks are briefly summarized below. Those completed within the current reporting period are indicated with brackets as “**{current period}**” along with a line down the left margin.

Task 1 – Synthesis and characterization of the MMIA

The MMIA to be developed in this project is comprised of superparamagnetic nanoparticles (SPIONs), which serve as a contrast agent for Magnetic Resonance Imaging (MRI), coated with a biopolymer (i.e. starch) to improve biocompatibility, and tagged with prostate cancer-targeting ligands. A significant challenge to translation of nanomedicine from lab bench to the clinical setting arises due to variations in particle behavior *in vivo* as a function of nanoparticle size distribution and surface properties. The vast majority of research in nanomedicine is conducted using particles having a broad size distribution; leading to uncertainty in the pharmacokinetics, biodistribution, and safety risks of the formulations. In order to reduce this barrier, we have developed synthesis and purification procedures that would produce SPIONs of a relatively narrow size distribution.

Our approach was to utilize the size-dependent magnetic properties of the SPIONs and the drag force exerted on a particle, which is also size dependent, to separate a MNP population with a wide size distribution into sub-populations with a more narrow distribution. The feasibility of this approach was first evaluated using a simulation developed in Matlab (MathWorks, Natick, MA). Using this simulation, we were able to determine the conditions required to “purify” particles of a particular size.

Figure 1 provides the predicted traces of MNP ranging in size from 40 nm to 400 nm, under the influence of a magnetic field. Using these results, a prototype separate process was established to take a sample of MNP having a broad size distribution and to produce SPIONs with tighter size control, as shown in **Figure 2**.

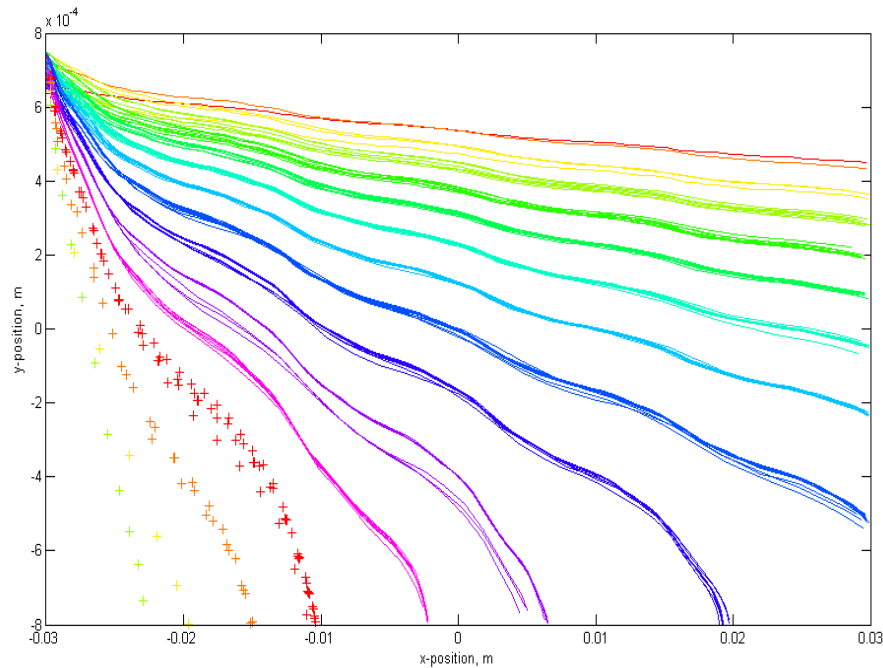


Figure 1. Predicted particle trajectories for magnetic nanoparticles in the size range of 44 nm (top, orange trace) to 400 nm (bottom, green markers) under the influence of drag and magnetic forces.

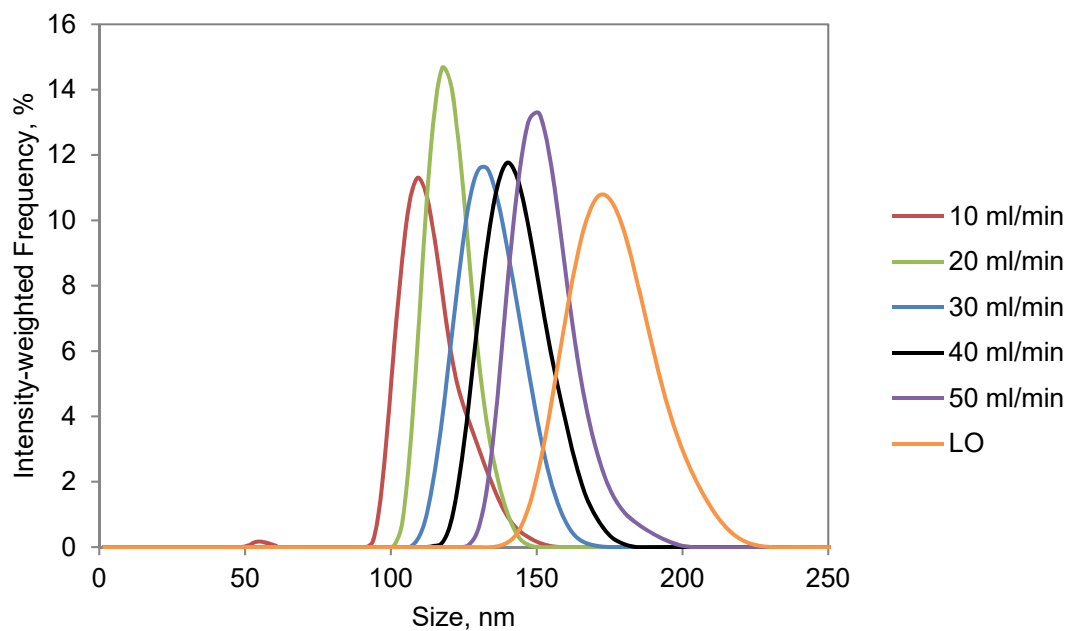


Figure 2. Average MNP size distributions of six fractions obtained using a prototype device to size-selectively separate SPIONs from a sample having a broad size distribution.

3b. Optimization of MMIA stability

For the probe to be effective, it has to be long circulating; accumulate selectively at the tumor site; and respond sensitively to a specific protease activity. To enhance the pharmacokinetic (PK) properties of the probe, we modified the surface of the MNP with polyethylene glycol, a polymer frequently utilized to improve stability of nanoparticles. We assessed size stability of the PEGylated MNP (PEG-MNP) in complete culture media, which contains proteins and other components found in blood plasma, using dynamic light scattering and performed *in vitro* experiments to mimic the first two steps (protein adsorption and macrophage uptake) of the reticuloendothelial system (RES) clearance process.

The starch coating of 50 nm and 100 nm SPIONs was crosslinked and coated with amine groups, and then functionalized with NHS-polyethylene glycol (PEG) of varying molecular weight (i.e., 2k, 5k or 20k Da) as shown in **Scheme 1**.



Scheme 1. Surface modification of starch-coated SPIONs into aminated and PEGylated SPIONs.

PEG coatings are often utilized on nanoparticles for their good biocompatibility and favorable chemical properties that enable further modifications. Since the coating itself may completely change the toxicity profile of SPIONs, SPIONs with a variety of surface coatings were tested, including starch-coated SPIONs, aminated SPIONs and finally PEGylated SPIONs. Analysis of SPIONs by transmission electron microscopy (TEM) and Fourier transform infrared spectroscopy (FTIR), and measurement of their magnetic properties provided results similar to that already in the literature, confirming successful modification, and are not repeated here. Some physicochemical characteristics of the 10 different SPIONs tested, however, are summarized in **Table 1**.

Table 1. Mean hydrodynamic diameter (HD) and zeta-potential (ZP) of SPIONs in deionized water and in Ham's F-12K culture media supplemented with 10% FBS.

Sample	In deionized water, at 37°C			In supplemented Ham's F-12K cultre media, at 37 °C					
	HD (nm)	PdI	ZP (mV)	1hr		24hrs		72hrs	
				HD (nm)	PdI	HD (nm)	PdI	HD (nm)	PdI
50 nm SPIONs									
Starch-coated	47 ± 1	0.12	-23 ± 3	36 ± 1	0.25	68 ± 2	0.28	148 ± 4	0.30
Aminated	90 ± 2	0.18	+13 ± 1	57 ± 1	0.32	55 ± 5	0.38	50 ± 3	0.38
2k-PEG	72 ± 3	0.20	+36 ± 1	41 ± 1	0.30	40 ± 1	0.30	40 ± 1	0.31
5k-PEG	71 ± 1	0.20	+34 ± 1	37 ± 2	0.42	36 ± 2	0.41	36 ± 2	0.44
20k-PEG	72 ± 4	0.20	+33 ± 2	35 ± 1	0.48	36 ± 1	0.47	33 ± 2	0.47
100 nm SPIONs									
Starch-coated	92 ± 1	0.09	-4 ± 1	117 ± 1	0.29	461 ± 4	0.70	1133 ± 30	0.19
Aminated	127 ± 5	0.17	+43 ± 1	119 ± 4	0.30	110 ± 3	0.22	108 ± 3	0.22
2k-PEG	117 ± 2	0.14	+36 ± 1	93 ± 1	0.24	95 ± 3	0.23	95 ± 2	0.24
5k-PEG	126 ± 4	0.14	+37 ± 1	103 ± 2	0.25	102 ± 2	0.24	114 ± 2	0.29
20k-PEG	154 ± 5	0.12	+32 ± 1	122 ± 3	0.26	117 ± 3	0.26	146 ± 2	0.36

The hydrodynamic diameters of both starch SPIONs were in close agreement with specifications provided by the manufacturer. After crosslinking of the starch coating and its amination, the mean hydrodynamic diameter of both 50 and 100 nm SPIONs increased significantly, possibly due to aggregation and/or due to loss of smaller particles during the processing. PEGylation further increased the hydrodynamic diameter as expected, but the effect of PEG molecular weight (2k, 5k, or 20k) varied between the 50nm and 100nm SPIONs. The effect on 50 nm particles was especially non-uniform as the aminated particles yielded the largest size, possibly due to aggregation. The hydrodynamic diameters of SPIONs were also evaluated when suspended in supplemented Ham's F-12K culture media at 37°C, the conditions employed for in vitro studies, with incubation times of 1, 24 and 72 hours. The hydrodynamic diameters of starch-coated 50nm and 100nm SPIONs were observed to increase with time, whereas the size of aminated, 2k-PEG and 5k-PEG SPIONs, and 50nm 20k-PEG SPIONs remained relatively constant over time. A moderate increase of the hydrodynamic diameter was noticed for 100 nm 20k-PEG SPIONs.

The surface charge of SPIONs gives an indication of their colloidal stability and may also further affect their cellular uptake. In one study, it was demonstrated that anionic nanoparticles, showing a high affinity for cell membranes, were captured more efficiently by cells than bare (dextran-coated) iron-oxide nanoparticles. In deionized (DI) water, starch-coated SPIONs displayed a negative to near neutral zeta potential while the aminated and PEGylated particles showed a high positive surface charge. Surprisingly, a higher zeta potential was observed for the PEGylated 50nm SPIONs compared to the aminated 50nm SPIONs. The PEG layer would be expected to mask some of the surface charge and it is unclear why this was not observed, although measurements were repeated. Aggregation seen with the aminated SPIONs may have had some contribution to this result.

It was confirmed that the SPIONs had a PEG content of up to 245 ± 7 nmol PEG/mg Fe. Next, *in vitro* size stability studies were conducted to validate the improved stability of our PEGylated SPIONs. The particles were incubated in cell culture media containing fetal bovine serum (FBS), to mimic their exposure to opsonizing proteins in the blood, and the particle size measured by dynamic light scattering (DLS) for a period of 24 hours. The results shown in **Figure 3** clearly demonstrate the improved stability of PEGylated particles while the unmodified control, starch particles are observed to rapidly increase in size.

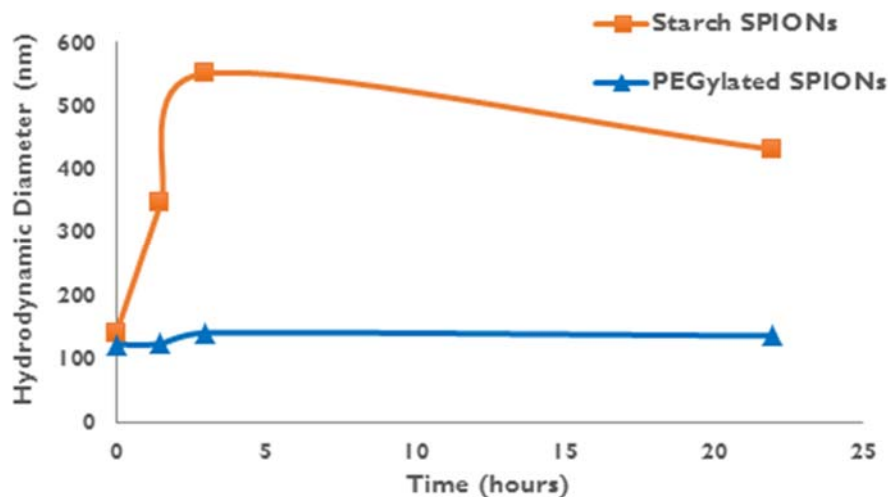


Figure 3. Size stability in complete RAW 264.7 cell culture medium (DMEM + 10% FBS + 1% antibiotics) at 37 °C was assessed over a period of 22 hours using dynamic light scattering. As shown, PEGylated SPIONs displayed much better size stability over starch SPIONs.

Colloidal stability is a very important feature that is necessary for successful tumor targeting. Particles that aggregate quickly get cleared from circulation quickly. PEGylated SPIONs also demonstrated significantly lower protein binding and markedly reduced macrophage uptake (**Figure 4a**) than the unmodified starch SPIONs. Among “normal” cells, macrophages have one of the highest rates of particle uptake; uptake of PEGylated SPIONs by healthy cells is therefore expected to be negligible.

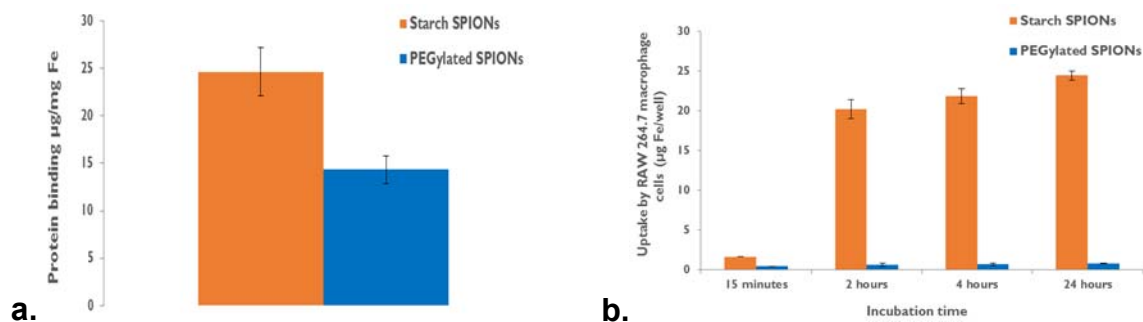


Figure 4. a) Protein binding in 60% FBS was studied to simulate the first step of SPION clearance from plasma. PEGylation caused a significant drop in protein adsorption; **b)** RAW 264.7 macrophage uptake of starch-coated and PEGylated SPIONs was measured over 24 hours to assess the impact of PEGylation on pharmacokinetic properties.

Our results indicated that PEG-MNPs showed significantly better size stability (i.e. resisted aggregation) and lower protein binding than the unmodified MNP. The MNPs were also incubated for varying time periods with macrophages. As shown in **Figure 4b**, the unmodified MNP were rapidly taken up by the RAW 264.7 macrophage cells, while only limited uptake of PEG-MNP was observed even after 24 hours. Among “normal” cells found in the body, macrophages have one of the highest rates of particle uptake. The synthesized particles are therefore expected to be very stable in

physiological media and uptake of PEG-MNPs by healthy cells is expected to be negligible.

3c. Assembly of the MMIA/fluorescent probe/targeting agent complex

While the previously stated results showed that stable MNPs have been developed and their uptake by “normal” cells minimized, it is also necessary that these particles target and accumulate in cancer cells. To induce uptake of MNPs by prostate cancer cells, we functionalized the surface with a tumor-targeting peptide (F3 peptide), which selectively binds to nucleolin present on the surface of tumor cells and endothelial cells of angiogenic tumor blood vessels. While nucleolin is present in all cells, it is only found on the extracellular surface of cancer cells – providing a means to target these cells. In order to determine whether the density of the targeting peptide affects the targeting efficiency, MNPs with a high density of F3-peptide, an intermediate density, and no targeting peptide were incubated with PC3 prostate cancer cells and the particle uptake measured after 1 and 4 hours. As shown in **Figure 5**, the F3-labelled MNPs should significantly greater targeting of the PC3 cells compared to the non-targeted, PEG-MNP. It should be noted that the F3-MNP did not show significant uptake by “normal” cells (data not shown), demonstrating our ability to maximize the target selectivity of the MNP to cancer cells.

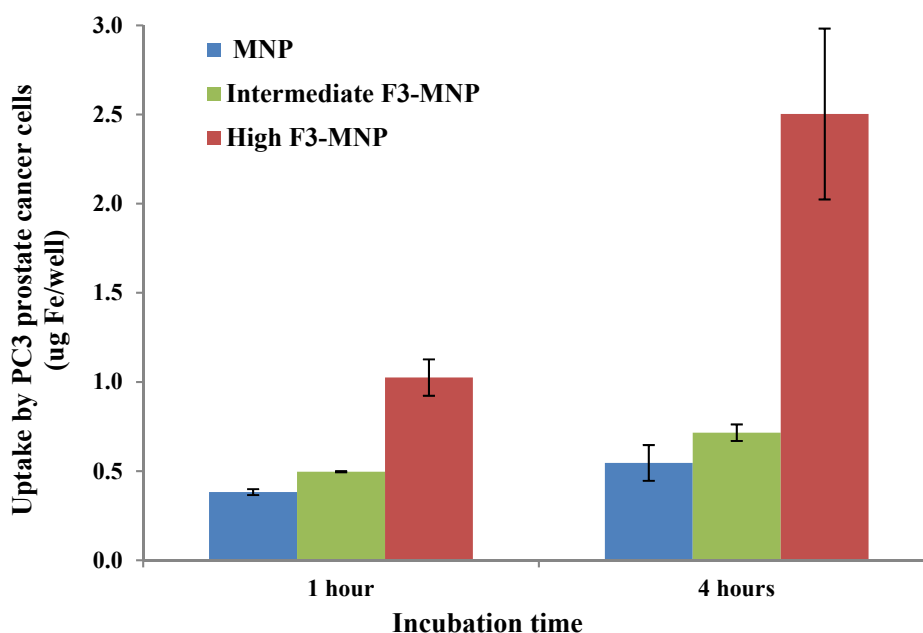


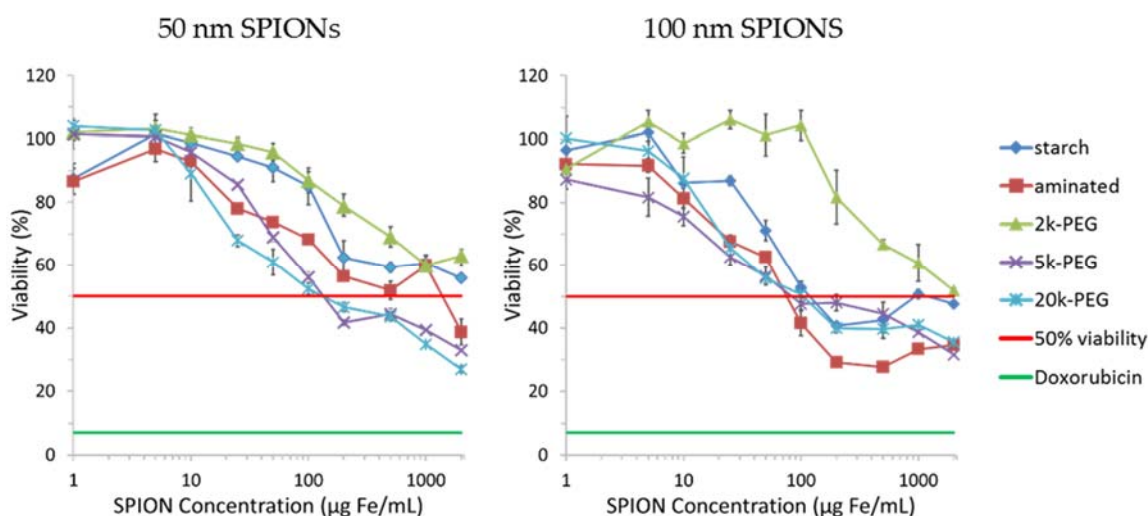
Figure 5. The conjugation of F3 tumor targeting peptide enhances MNP uptake by PC3 prostate cancer cells compared to the non-targeted PEG-MNP.

Task 2 – *In vitro* characterization of selectivity, protease specificity, and detection sensitivity

In order to insure that administered doses of MNP do not elicit toxic effects, the cytotoxicity of the MNPs were measured against the Chinese hamster ovary (CHO-K1) cell line. CHO cells were selected for this particular assay because of their extensive

use in evaluating cytotoxicity of active agents for approval by the U.S. Food & Drug Administration (FDA). As shown in **Figure 6**, the results indicate that toxicity of the MNP is dependent on particle size, surface chemistry, concentration, and duration of exposure. No significant toxicity was observed after a relatively short exposure of just 24 hrs with any of the MNPs. While significant toxicity was observed when MNP were incubated with cells for 72 hours, this was strongly concentration dependent. In order to minimize background signal, it is desirable that the MNP clear from blood circulation relatively quickly but remain sufficiently long for tumor accumulation. Future *in vivo* studies will determine the plasma pharmacokinetics of the MNP but, according to past experience, the circulation half-life is expected to be less than 12 hours. Additionally, particle concentration is expected to be less than 100 $\mu\text{g Fe/mL}$, a concentration below which the MNP modified with 2kDa PEG showed negligible toxicity.

A. 72 hour incubation



B. 24 hour incubation

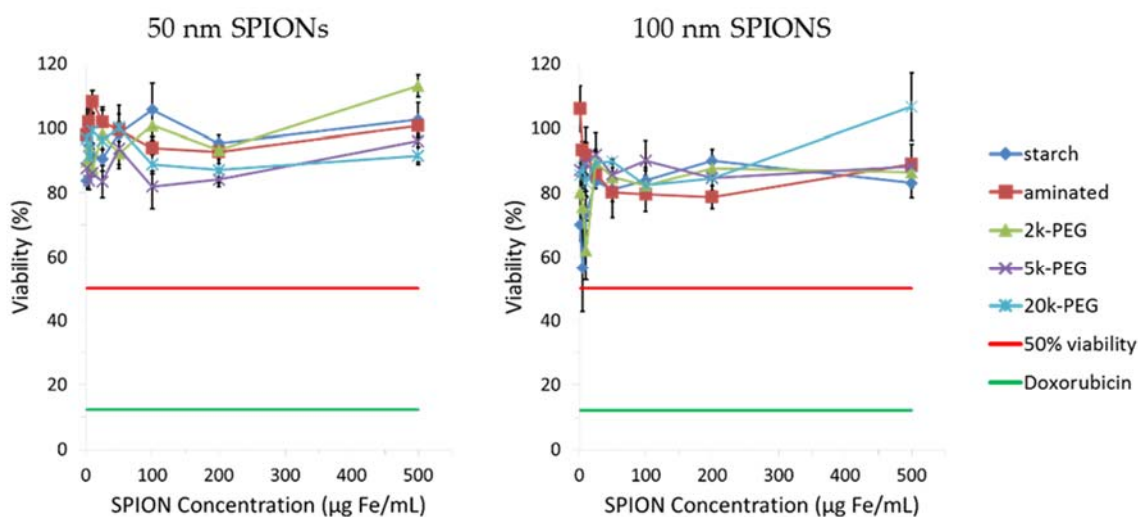


Figure 6. Cytotoxicity of superparamagnetic iron-oxide nanoparticles (SPIONs) in Chinese Hamster Ovary (CHO-K1) cells evaluated with the (a) tetrazolium dye 3-(4,5-dimethylthiazol-2-yl)-2,5-diphenyltetrazolium bromide (MTT) after a) 72 hour and b) 24 hour incubation with MNPs having a

“starch” coating, a positively-charged “aminated” coat, or PEG (MW 2k, 5k, or 20k Daltons) coating. The 50% viability line and a doxorubicin positive control are shown for comparison.

For prostate cancer targeting, in the event that the F3 peptide proves to be non-specifically taken up by non-target cells during *in vivo* studies, additional peptides were identified for possible targeting of the MMIA. Several targeting ligands that demonstrate high affinity for PC3M and LNCaP prostate cancer cells, while showing minimum binding to RWPE-1 normal prostate cells. In this study, phage particles having a specific peptide sequence on the surface, as listed below, were incubated for one hour with: 1) highly metastatic PC3-M prostate cancer cells; 2) slow growing LNCaP prostate cancer cells; 3) normal prostate cells (RWPE-1); and 4) serum control. The cells were then rinsed with PBS and the amount of bound phage determined as a ratio of the initial loading, as shown in **Figure 7**. These results provide us with candidate targeting ligands that would enable the targeting of both metastatic PC3-M and slow-growing LNCaP prostate cancer cells. This would enable the use of a single targeted MMIA for detection of proteolytic in aggressive PC3-M tumors as well as non-aggressive controls. The ligands labeled P1-P6 were found to have especially high affinity for the PC-3M cells, while also showing varying specificity for the LNCaP and RWPE-1 cells.

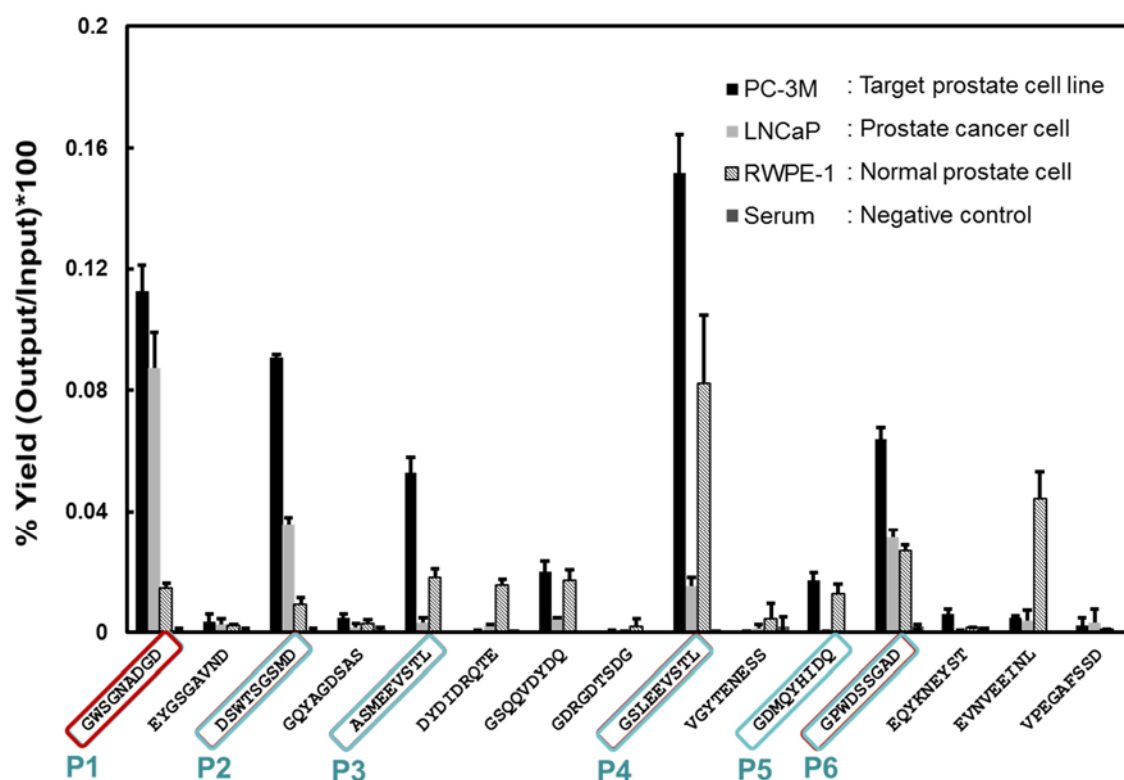


Figure 7. Relative binding affinity of prospective targeting ligands with PC3-M and LNCaP prostate cancer cells, compared to normal prostate cells and serum controls. Several ligands with high selectivity for prostate cancer have been identified.

Binding of targeting ligands, labeled P1-P6 in Figure 7, to PC3M cells was further visualized using fluorescence microscopy, as shown in **Figure 8**. The results indicated that particles P3, P4, and P5 bound to the PC3-M cells to a greater extent than the other particles. Further visualization and characterization of their binding to the LNCaP and normal prostate cells are ongoing but these promise to be good alternatives to F3 for targeting of MNPs.

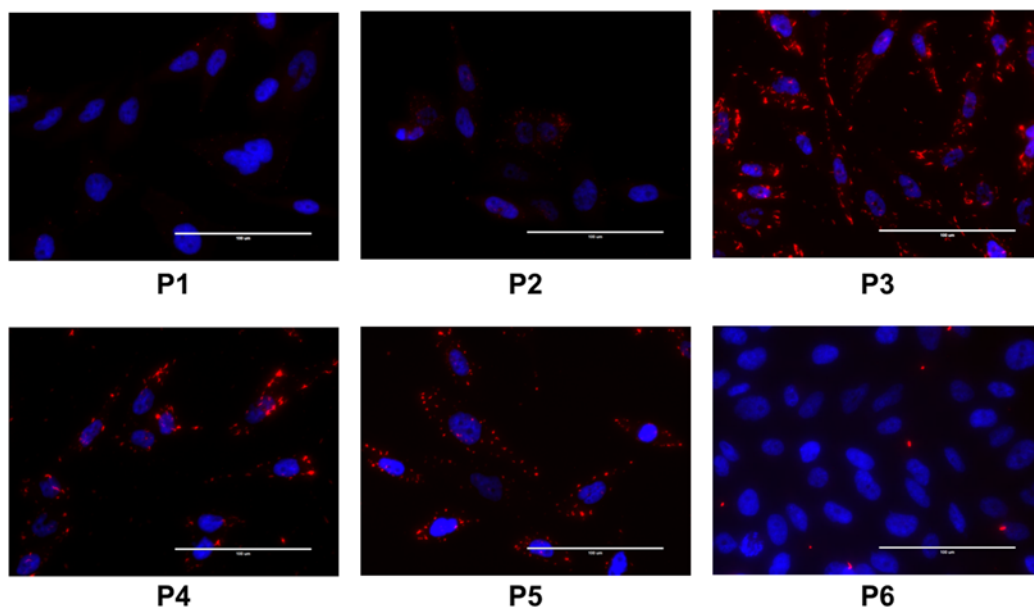


Figure 8. Fluorescent images showing the *in vitro* binding of six different targeting ligands (red markers) to PC3-M cells (nucleus stained blue).

In addition to the targeting of the MNP to cancer cells, an important component of the proposed work is to label the particles with a fluorescent dye whose release is triggered by proteolytic activity. The fluorescently labeled peptide 5-TAMRA-SGKGPRQITAGGC-amide was conjugated to the surface of the MNP using maleimide chemistry. To determine its response to proteolytic activity, the MNP-peptide was incubated with varying concentrations of the protease TrypLE Express (Life Technologies, Grand Island, NY) for 15 minutes, centrifuged, and the fluorescence of the supernatant measured at 546/579 (characteristic of 5-TAMRA fluorescent dye). As seen in **Figure 9**, the concentration of the protease correlated with the release of 5-TAMRA from the surface of the MNP. Based on these preliminary results, we are currently evaluating the ability of this system to detect activity of legumain and matrix metalloproteinase 9 (MMP-9). Legumain and MMP-9 are important tumor-associated proteases, overexpressed in the prostate cancer microenvironment, and the level of which is associated with metastatic potential of the cancer.

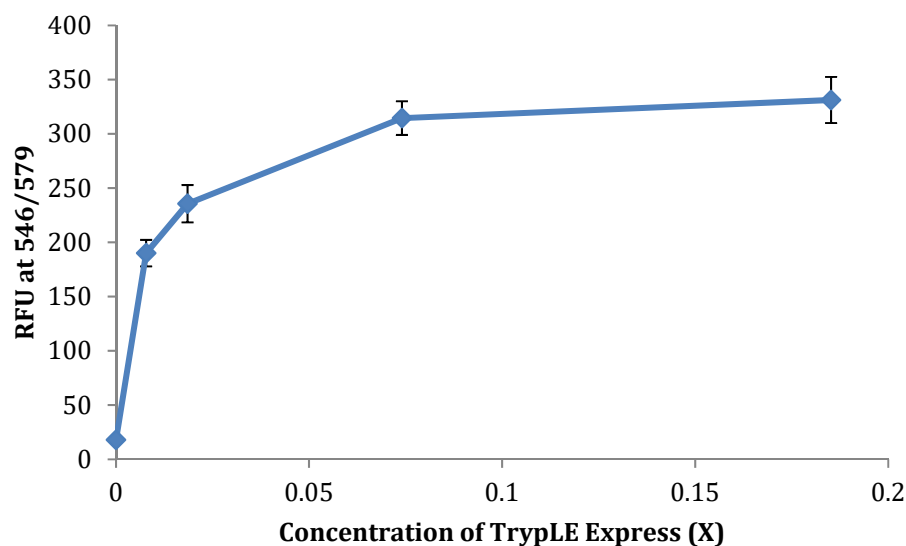


Figure 9. Fluorescently labeled peptides were conjugated to the surface of MNP and their initial release rate measured, as ratio of fluorescence signal at 546 nm and 579 nm, with varying concentrations of trypsin protease. Fluorescence intensity was measured after a 15 minute incubation.

The next step would be to evaluate the MMIA with an appropriate cell line expressing matrix metalloproteinase (MMP). While MMP has been shown to be highly expressed by PC3 cells *in vivo*, PC3 do not secrete measurable quantities of MMP in *in vitro* cultures. While the ultimate goal is to target prostate cancer cells, the human fibrosarcoma HT-1080 cell line is one of the most frequently used cell types for MMP research *in vitro* and *in vivo*. This is primarily because it is one of the few cell lines to express MMP *in vitro*. Moreover, HT-1080 tumors grow quickly *in vivo* and are very well vascularized, enabling penetration by nanoparticles. We conducted gelatin zymography studies on HT-1080 serum-free conditioned media, which confirmed the secretion of gelatinase, an MMP, as shown in **Figure 10**.



Figure 10. A) Illustrates the main steps in gelatin zymography. **B)** Gelatin zymography on serum-free conditioned media and lysate of HT-1080 cells confirmed gelatinase secretion by HT-1080 cells.

Having confirmed the secretion of MMP by HT-1080 cells, we then sought to select an appropriate targeting ligand for HT-1080 cells. This would enable the use of HT-1080 cells as a well-characterized, positive control for the *in vivo* studies. The overexpression of $\alpha_v\beta_3$ integrin, an important tumor biomarker, on the surface of HT-1080 cells has been previously reported in the literature. The RGD motif, found in several extracellular proteins, is known to be a potent integrin $\alpha_v\beta_3$ antagonist and cyclic forms of the RGD (cRGD) peptide has been widely utilized as an $\alpha_v\beta_3$ integrin targeting ligand. To induce uptake by HT-1080 cells, the surface of MNPs were functionalized with cRGD through a heterobifunctional PEG (MAL-PEG-NHS). The particles were labeled cRGD-PEG-SPION and a control that lacked cRGD was also synthesized, and labeled PEG-SPION.

Prior to running cell uptake studies, we tested the size stability of cRGD-PEG-SPION in HT-1080 complete culture medium. **Figure 11A** shows that the particles were very stable over a period of 72 hours. Next, we investigated whether the quantitative BCA protein assay can be used to measure HT-1080 cell number. An excellent linear fit was generated (**Figure 11B**), which ensured that we are able to correct for the number of cells in different wells. Finally, cellular uptake of the SPION by HT-1080 cells was conducted using the ferrozine assay for SPION quantification and the BCA assay for cell quantification. cRGD-PEG-SPION displayed significantly higher uptake over control PEG-SPION (**Figure 11C**). This was an important result that confirmed our ability to actively target HT1080 cells and provided a positive control for future studies.

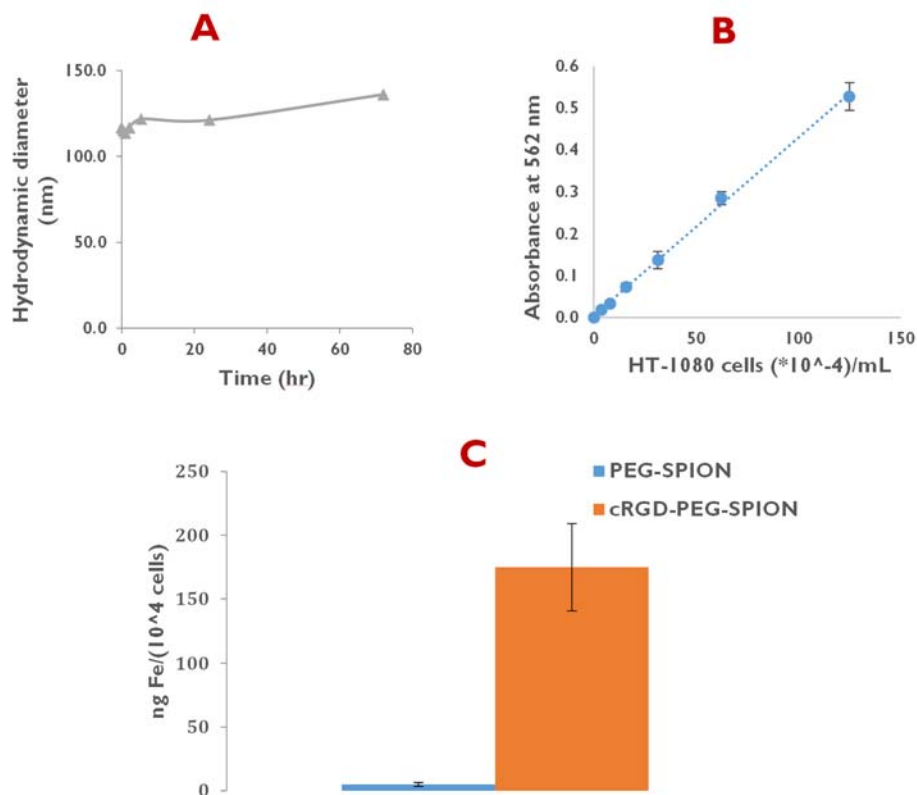


Figure 11. cRGD studies - **A.** cRGD-PEG-SPION showed excellent size stability in HT-1080 complete culture medium over a period of 72 hours. **B.** Standard curve for BCA protein quantification at different

HT-1080 cell number. **C.** cRGD-PEG-SPION displayed significant HT1080 cell uptake versus control PEG-SPION.

We evaluated the ability of our system to detect the activity of matrix metalloproteinase 2 and 9 (MMP-2/9). We conjugated a fluorescently (5-FAM) labeled MMP-2/9 specific peptide (sequence: 5-FAM-GPLGVRGC) to the surface of the MNP using maleimide chemistry. The resulting MMP-specific-peptide-MNP was labeled (MSP-PEG-MNPs). To determine its response to proteolytic activity, MSP-PEG-MNPs were incubated with varying concentrations of activated MMP-2 and MMP-9 for 3 hours, centrifuged, and the fluorescence of the supernatant measured at 495/525 (characteristic of 5-FAM fluorescent dye). As seen in **Figure 12**, the concentration of the protease correlated with the release of 5-FAM from the surface of the MNP.

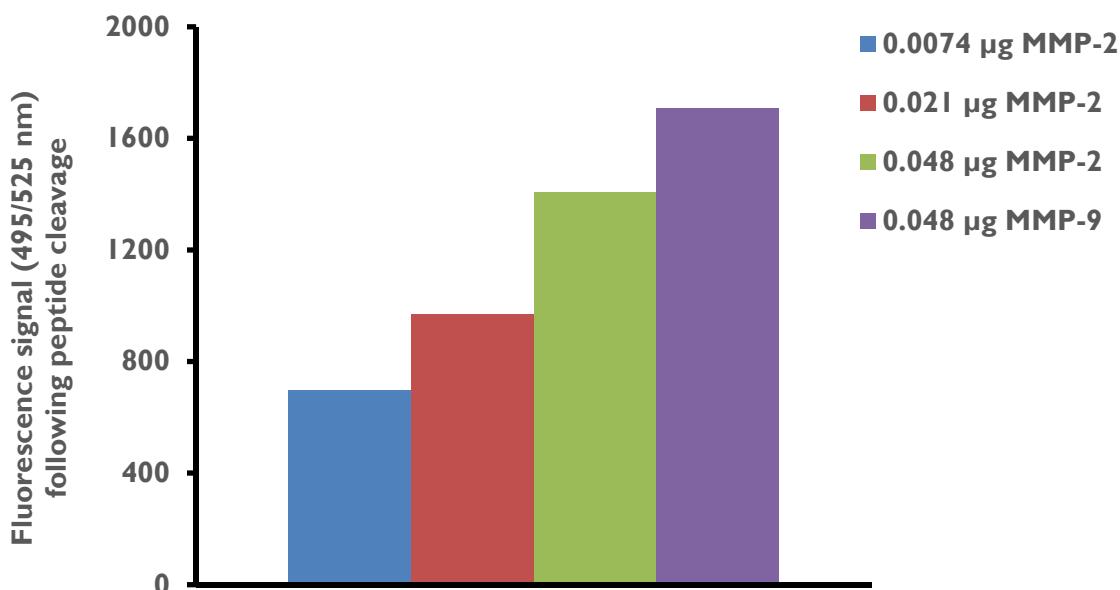


Figure 12. Conjugation of an MMP-2/9 cleavable peptide allows us to quantify MMP-2/9 concentrations in solution

The toxicity of SPIONs with different surface properties were assessed *in vitro*. The size of PEG, which alters the surface properties of SPIONs, can significantly affect the pharmacokinetics and biodistribution profiles of SPIONs. Figure 13 demonstrates a schematic for obtaining the different sized PEG-SPIONs.

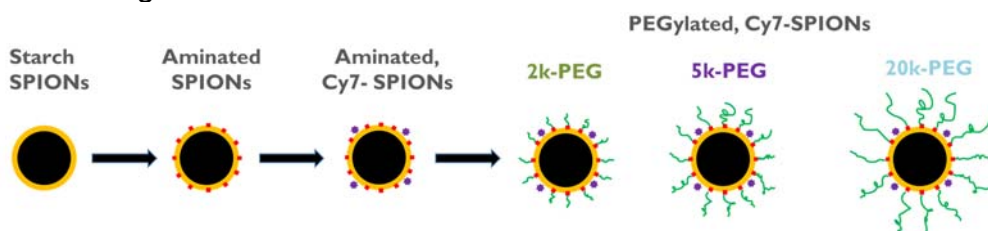


Figure 13. Synthesizing PEGylated, Cy7-SPIONs

All three PEGylated SPIONs (2K, 5K and 20K-PEG SPIONs) demonstrated markedly reduced macrophage uptake (**Figure 14**) than aminated SPIONs. However, the size of PEG didn't cause a significant difference in macrophage uptake.

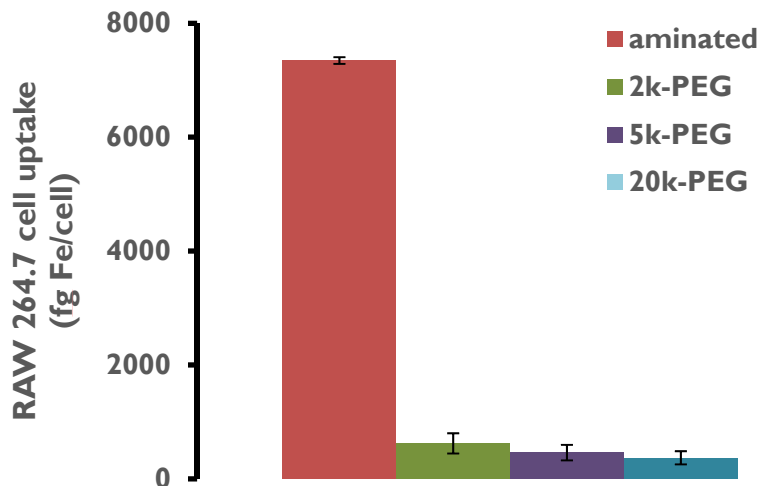


Figure 14. PEGylation of SPIONs drastically reduces uptake by macrophage cells compared to unmodified SPIONs. However, the size of PEG (2k, 5K, 20K) didn't significantly impact uptake.

Multispectral optoacoustic tomography (MSOT) imaging will be used to compare the *in vivo* pharmacokinetics, i.e. disappearance rate from circulation, and biodistribution profiles of Cy 7 fluorophore conjugated superparamagnetic iron oxide nanoparticles (Cy7-SPIONs) coated with three different sizes (2, 5 and 20 kDa) of polyethylene glycol (PEG). MSOT image reconstruction and spectral unmixing algorithms will be used to visualize and quantify the concentration of Cy7-SPION in circulation (in visible arteries/veins) and in organs of elimination, which include the liver, spleen and kidneys. Before we can conduct the *in vivo* studies, we needed to confirm the photoacoustic properties of the PEGylated, Cy7 SPIONs. We also needed to make sure that the size of PEG doesn't have an impact on the photoacoustic signal. We optimized the Cy7 to PEG surface density on the surface of SPIONs that balanced nanoparticle size stability with its photoacoustic property. Afterwards, we conducted MSOT phantom studies on various concentrations of each type of SPIONs. The photoacoustic signal correlated strongly with nanoparticle concentration (strong linear fit), as shown in **Figure 15**. MSOT could also detect very low nanoparticle concentrations (0.005 mg Fe/mL). Lastly, PEG size did not affect the photoacoustic signal.

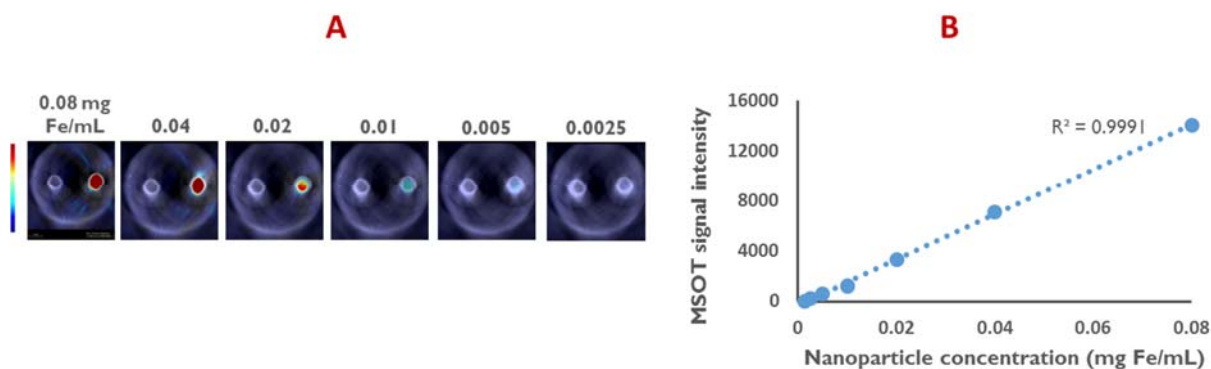


Figure 15. The photoacoustic signal obtained from MSOT (A) correlates strongly with nanoparticle concentration (B).

{current period: We previously showed that PEGylation of the SPION surface prevent uptake, and thereby clearance, of particles by macrophages. However, any changes to surface chemistry, such as the addition of a fluorescent dye, could potentially shift this stability. It was, therefore, important to assess the impact of incorporating the Cy7 fluorescent dye on macrophage uptake for all three PEGylated SPIONs (i.e. SPIONs modified with 2kDa, 5kDa and 20kDa PEG). All three PEGylated SPIONs (2K, 5K and 20K-SPIONs) had demonstrated markedly reduced macrophage uptake (**Figure 14**) than aminated SPIONs in the absence of Cy7. When the Cy7 dye was added, however, uptake of 20K-SPIONs by macrophage cells was markedly higher than that for 2K and 5K-SPIONs. We hypothesize that, due to its larger hydrodynamic diameter and surface footprint, the resulting low density of PEG coverage on the particle surface with the 20kDa PEG does not sufficiently hinder inter-particle, hydrophobic interactions and this leads to aggregation and subsequent macrophage uptake. The, 20K-SPIONs were therefore removed from future studies.

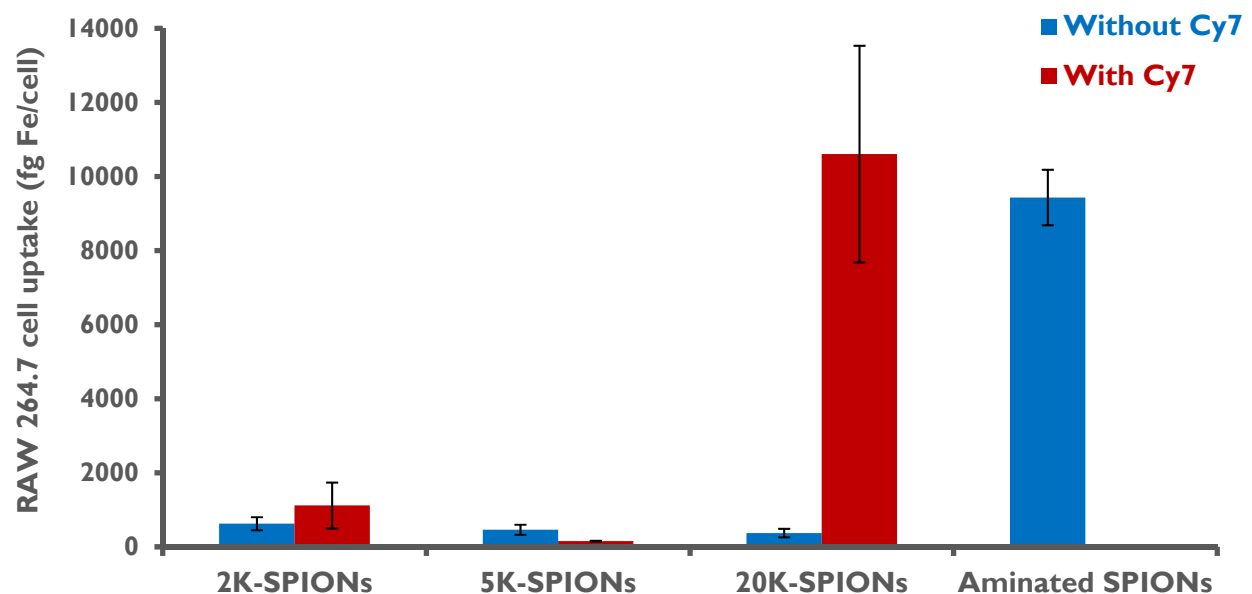


Figure 16. Macrophage uptake of SPIONs modified with 2kDa, 5kDa and 20kDa PEG, with and without the addition of Cy7 fluorescent dye.

Since the goal is to develop an imaging agent what would enable the detection of cancer-related protease activity, it is also important to determine the response of the agent to non-specific proteases found within physiological fluids. Therefore, the selectivity of the MMP-specific nanoparticles (MSP-PEG-MNPs) was evaluated against various tumor-associated proteases. These proteases were incubated with a fixed amount of MSP-PEG-MNPs for 10 minutes, centrifuged, and the fluorescence of the supernatant at 495/525 nm measured to quantify the amount of hydrolyzed peptide. MSP-PEG-MNPs displayed significantly higher selectivity towards MMPs compared to trypsin, cathepsin B, a variety of caspases and legumain (**Figure 17A**). When comparing between MMPs, there was a statistically greater response of the particles towards MMP-2 (**Figure 17B**).

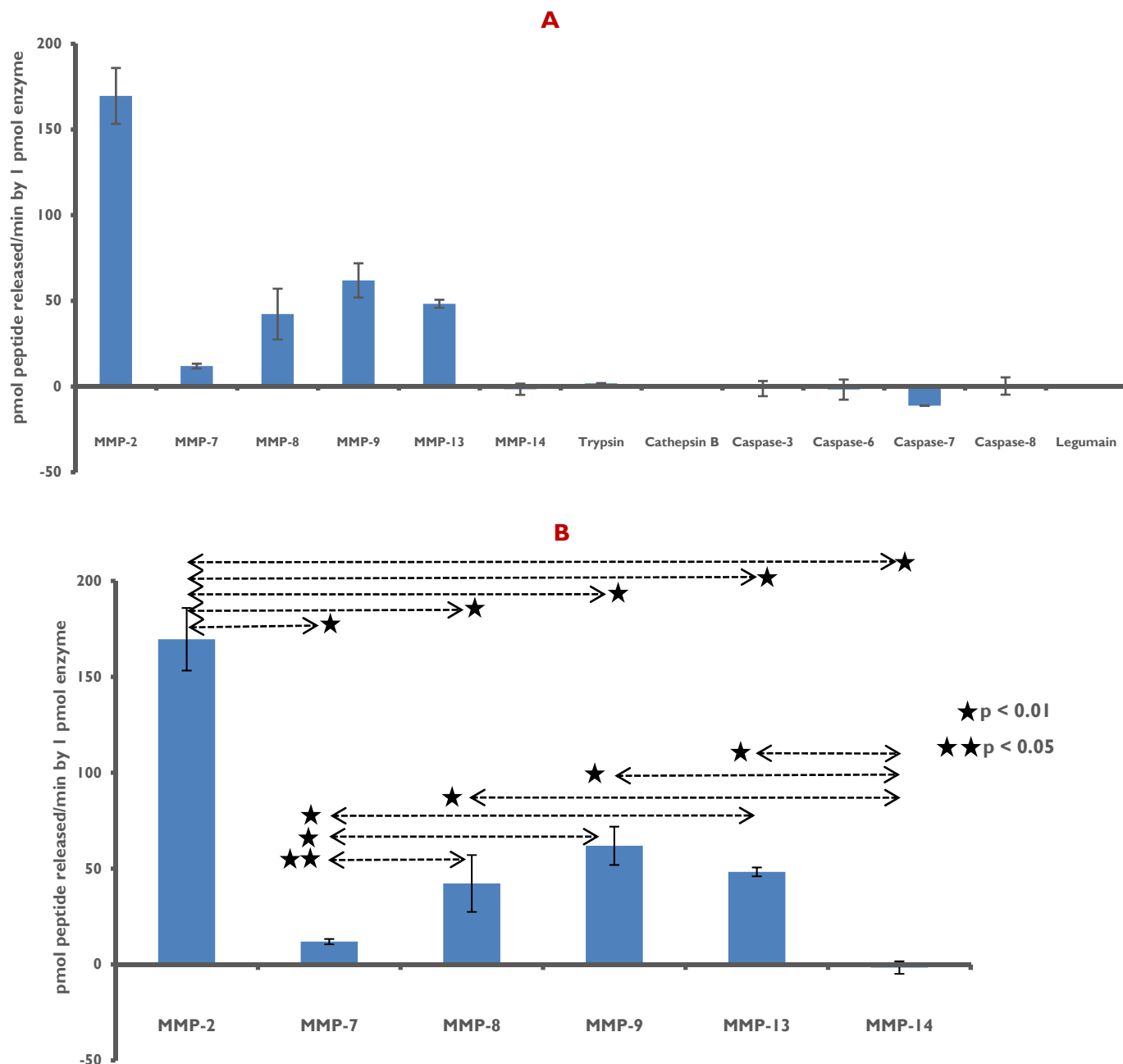


Figure 17. pmol peptide on surface of MNP hydrolyzed per minute by 1 pmol of several tumor-associated proteases (A); only showing results for MMPs (B).

Next, we studied the Michaelis-Menten kinetics for the MMPs by measuring the initial reaction rate as a function of various MSP-PEG-MNP concentrations (**Figure 18A**). The experimental data was fitted to the Michaelis-Menten reaction model and the parameter k_{cat}/K_m , a measure of catalytic efficiency, was calculated. MMP-2 had a significantly higher ($p < 0.01$) catalytic efficiency towards MSP-PEG-MNPs than all the other MMPs tested (**Figure 18B**).

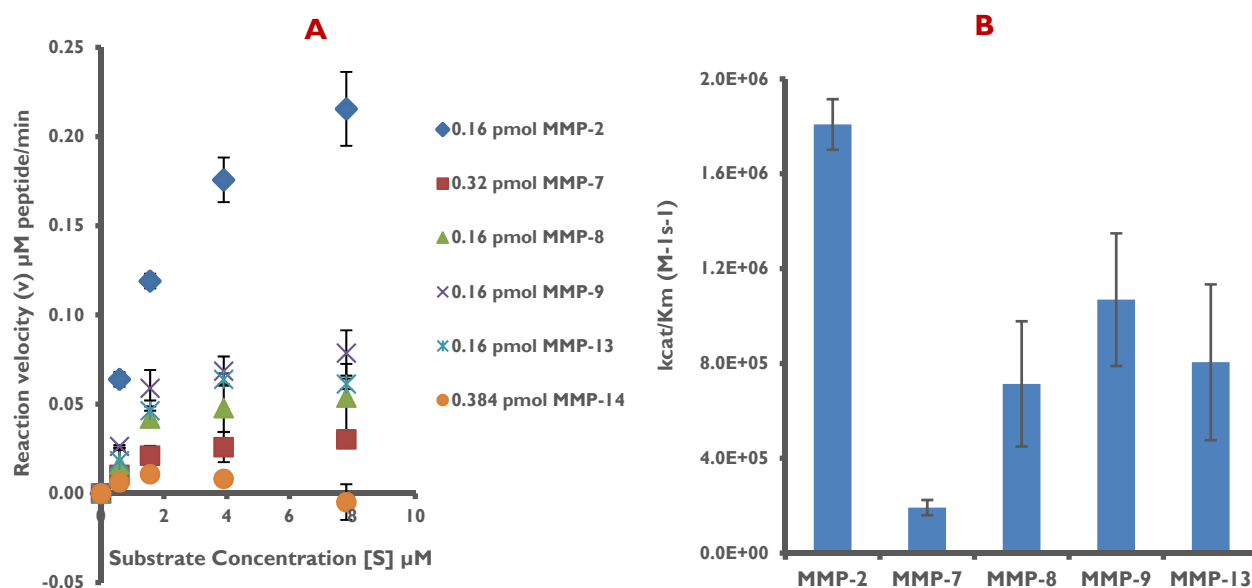


Figure 18. Michaelis-Menten reaction kinetics. (A) Initial reaction rate at different substrate concentrations for all MMPs tested; and (B) K_{cat}/K_m , a measure of catalytic efficiency, for MMP-2,7,8,9 and 13.

Next, the specificity of the MMP specific peptide 5-FAM-GPLGVRGC towards MMP-2, was compared to a scrambled version of the peptide (FAM-GVRLGPGC); particles with the scrambled peptide were labeled as MSCRP-PEG-SPIONs. A second MMP-specific peptide, with the amino acid sequence FAM-GGPRQITAGC, was also tested (labeled as MSP2-PEG-SPIONs). All three particles were incubated with 1 pmol MMP-2, and the amount of hydrolyzed peptide was quantified through a fluorescence measurement of the supernatant. Results are shown in **Figure 19A**. MMP-2 displayed a significantly higher affinity towards the nanoparticles carrying MMP-specific peptides as opposed to the ones carrying the scrambled peptide.

The results indicate that we have successfully synthesized SPIONs with a specific affinity to MMPs, specifically MMP-2, versus other proteases. It is also essential that the conjugated peptide remains stable in circulation prior to reaching the tumor microenvironment. The hydrolytic release of labeled peptides on the particles were therefore tested in the presence of 1 pmol MMP-2 versus 100% fetal bovine serum (FBS) and complete culture media (**Figure 19B**). The amount of peptide released per minute was significantly higher in the presence of MMP-2 versus than in FBS and culture media.

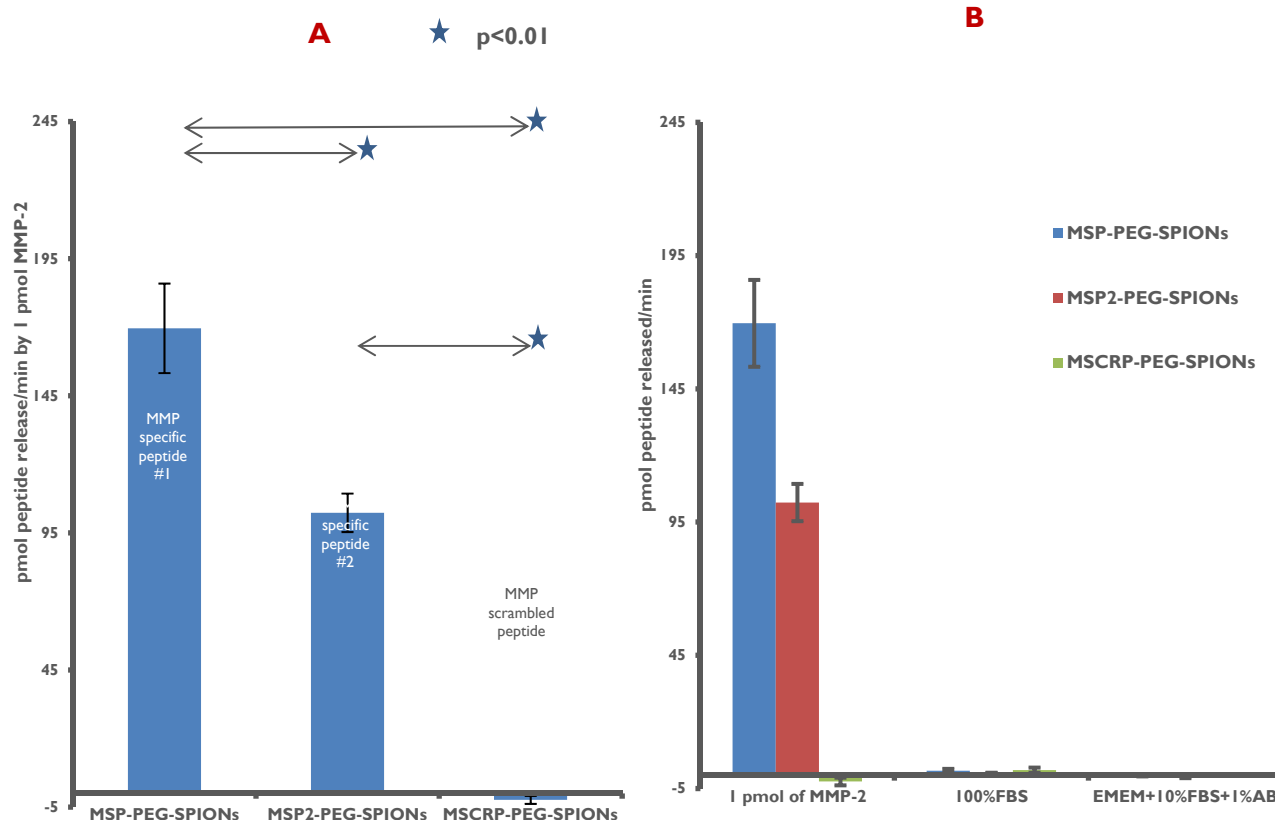


Figure 19. Pmol peptide hydrolyzed per minute for MSP-PEG-SPIONs (with MMP specific peptide #1), MSP2-PEG-SPIONs (with MMP specific peptide #2), and MSCRP-PEG-SPIONs (with MMP scrambled peptide to #1) in (A) with 1 pmol MMP-2, and (B) in various conditions to assess stability in physiological mimicking conditions }

Opportunities for training and professional development

During this project, two graduate students, a Master student and one PhD student, have been trained in the synthesis and characterization of MNPs, as well as in the techniques of cell culture work. The graduate students have also presented their work and attended talks at several conferences, including:

- 2013 AIChE Annual Meeting, San Francisco, CA
- 2014 AIChE Annual Meeting, Atlanta, GA
- 2015 Science and Technology Open House, Montgomery, AL
- 2015 Auburn Univ. Research Initiative in Cancer (AURIC) Meeting, Auburn, AL
- 2016 Alabama Regional NanoBio Meeting, Auburn, AL
- 2016 AIChE Annual Meeting, San Francisco, CA

The Master's student has graduated and is currently pursuing a PhD degree at Northwestern University.

Additionally, six undergraduate students have been mentored in the lab during the funded period. One undergraduate student has since graduated and is currently attending the medical school at the University of Alabama - Birmingham. Two other

undergraduate students graduate recently and accepted positions in the commercial sector. The fourth student has been accepted into the PhD program in chemical engineering at the University of Notre Dame. The remaining two students are currently seniors in the chemical engineering program.

Dissemination of results to communities of interest

Nothing to report

Plan for the next report period

Much of the work proposed for Task 1 (i.e. synthesis and optimization of the MNP) and Task 2 (i.e. *in vitro* studies of cancer cell target specificity and protease specificity) have been completed. During the next report period, we will continue to evaluate the MNP with *in vitro* assays and also plan to initiate the proposed *in vivo* work. **The project is currently on schedule with the timeline provided in the statement of work.**

4. Impact

Nothing to report.

5. Changes/Problems

Nothing to report.

6. Products

Journal Publications:

Zhou C, Qian Z, Choi YS, David AE, Todd P, Hanley TR. Application of magnetic carriers to two examples of quantitative cell analysis. *Journal of Magnetism and Magnetic Materials* (2017) 427:25-28. *acknowledgement of federal support (yes)*

Anani T, Panizzi P, David AE. Nanoparticle-based probes to enable noninvasive imaging of proteolytic activity for cancer diagnosis. *Nanomedicine* (2016) 11(15):2007-2022. *acknowledgement of federal support (yes)*

Hanot CC, Choi YS, Anani T, Soundarrajan D, David AE. Effects of iron-oxide nanoparticle surface chemistry on uptake kinetics and cytotoxicity in CHO-K1 cells. *Int. J. Mol. Sci.* (2016) 17(54). *acknowledgement of federal support (yes)*

Rogers HB, Anani T, Choi YS, Beyers RJ, David AE. Exploiting size-dependent drag and magnetic forces for size-specific separation of magnetic nanoparticles. *Intl J of Molecular Sciences* (2015) 16:20001-19. *acknowledgement of federal support (yes)*

Conference Presentation:

Yeh B, David AE. Utilizing magnetic and diffusive properties to improve size homogeneity of superparamagnetic nanoparticles. 2016 AIChE Annual Meeting, San Francisco CA. 2016 Nov. (oral)

Anani T, Choi YS, Panizzi P, David AE. Multispectral optoacoustic tomography (MSOT) for imaging of pharmacokinetics and biodistribution of pegylated superparamagnetic iron oxide nanoparticles. 2016 AIChE Annual Meeting, San Francisco CA. 2016 Nov. (oral)

Anani T, Choi YS, Panizzi P, David AE. Magnetic nanoparticles for multispectral optoacoustic imaging of proteolytic activity in the tumor microenvironment. 2015 AIChE Annual Meeting, Salt Lake City UT. 2015 Nov. (oral)

Anani T, Choi YS, David AE. Magnetic nanoparticles for non-invasive quantification of prostate cancer aggressiveness. 2014 AIChE Annual Meeting, Atlanta GA. 2014 Nov. (oral presentation)

Rogers HB, Anani T, Read C, David AE. Magnetic nanoparticles as multimodal contrast agents for the diagnosis of prostate cancer. 2013 AIChE Annual Meeting, San Francisco CA. 2013 Nov. (poster presentation)

Anani T, Read C, Rogers H, Choi YS, David AE. Magnetic nanoparticles as multimodal contrast agents for measuring prostate cancer aggressiveness. 2013 AIChE Annual Meeting, San Francisco CA. 2013 Nov. (poster presentation)

7. Participants & Other Collaborating Organizations

Individual Participants:

Name:	Allan E. David
Project Role:	PI
Person month worked:	1
Contribution to project:	Overall planning, data analysis, trouble shooting, and monitoring of graduate students

Name:	Tareq Anani
Project Role:	Graduate student
Person month worked:	12
Contribution to project:	Synthesis of MNPs and cell culture studies
Funding support:	Partially supported by Auburn University

Research Initiative in Cancer Fellowship

Name: Alan Hanley
Project Role: Graduate student
Person month worked: 6
Contribution to project: Synthesis and characterization of nanoparticles

Name: Young Suk Choi
Project Role: Postdoctoral fellow
Person month worked: 2
Contribution to project: Training of graduate students in cell culture techniques and identification of prostate cancer targeting ligands
Funding support: Partially supported by Auburn University Research Initiative in Cancer

Active other support of PI

Sponsor: Auburn University Research Initiative in Cancer (AURIC)
Project Title: Nanoencapsulation to enhance the tumor suppressing effects of checkpoint inhibitors and immunostimulants
PI/Co-PIs: David AE (PI); Baker HJ; Johnson AJ; Smith AN; Roberts S (Altimmune); Georges B (Altimmune)
Amount: \$200,000
Period: 10/1/2017 – 9/30/2019

Sponsor: Auburn University Intramural Grants Program
Project Title: Targeting of LipDox to prostate cancer cells
PI/Co-PIs: David AE (PI)
Amount: \$40,000
Period: 5/1/2017 – 5/1/2019

Sponsor: NIH
Project Title: Advances in Contact Lens Materials to Extend Wear Time for a New Standard in Vision Correction and Future Medical Devices
PI/Co-PIs: Domszy R (ISTN Inc); David AE (co-I)
Amount: \$225,000 (AU Portion: \$50,000)
Period: 4/1/2017 – 3/31/2018

Sponsor: NIH
Project Title: Ophthalmic drug delivery using a multi-layer contact lens design that enables targeting, constant-rate release and failure protection
PI/Co-PIs: Yang AJ (Lynthera Corp); David AE (co-I)
Amount: \$225,000 (AU Portion: \$50,000)
Period: 5/1/2016 – 4/30/2018

Involved organizations as partners

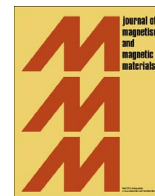
Nothing to report

8. Special Reporting Requirements

Nothing to report

9. Appendices:

Original copy of manuscript (see next page)



Application of magnetic carriers to two examples of quantitative cell analysis



Chen Zhou^a, Zhixi Qian^a, Young Suk Choi^a, Allan E. David^a, Paul Todd^{b,*}, Thomas R. Hanley^a

^a Department of Chemical Engineering, 212 Ross Hall, Auburn University, Auburn, AL 36849, USA

^b Techshot, Inc., 7200 Highway 150, Greenville, IN 47124, USA

ARTICLE INFO

Keywords:

Magnetophoretic mobility
Nanoparticle uptake
Cell separation
Cell velocimeter

ABSTRACT

The use of magnetophoretic mobility as a surrogate for fluorescence intensity in quantitative cell analysis was investigated. The objectives of quantitative fluorescence flow cytometry include establishing a level of labeling for the setting of parameters in fluorescence activated cell sorters (FACS) and the determination of levels of uptake of fluorescently labeled substrates by living cells. Likewise, the objectives of quantitative magnetic cytometry include establishing a level of labeling for the setting of parameters in flowing magnetic cell sorters and the determination of levels of uptake of magnetically labeled substrates by living cells. The magnetic counterpart to fluorescence intensity is *magnetophoretic mobility*, defined as the velocity imparted to a suspended cell per unit of magnetic ponderomotive force. A commercial velocimeter available for making this measurement was used to demonstrate both applications. Cultured *Gallus* lymphoma cells were immunolabeled with commercial magnetic beads and shown to have adequate magnetophoretic mobility to be separated by a novel flowing magnetic separator. Phagocytosis of starch nanoparticles having magnetic cores by cultured Chinese hamster ovary cells, a CHO line, was quantified on the basis of magnetophoretic mobility.

1. Introduction

When cells are to be separated by fluorescence activated cell sorters (FACS) it is customary to determine the distribution of fluorescence intensity in a fluorophore-labeled population of cells and to set flow parameters that select the desired cell population [1]. Likewise the measurement of magnetophoretic mobility has been used historically to set flow parameters in a quadrupole magnetic cell sorter [2–5] and a very early version of a magnetic flow sorter [6,7]. This approach does not appear to have been applied to a wider variety of magnetic cell sorters. The magnetophoretic mobility requirements for almost any magnetic separation can be determined by computational fluid dynamic analysis [8,9]. In a separation with flow-rate requirements, for example, a minimum required mobility can be calculated. Tumor cells were chosen as an example of cells to be labeled for magnetic separation owing to interest in magnetically separating tumor cells from circulating blood [10,11].

Fluorescence flow cytometry is also used to determine levels of uptake of fluorescently labeled substrates by living cells. Fluorescent substrates are usually antibodies identifying cell surface markers and may or may not be internalized by receptor-mediated endocytosis and/or due to cell-membrane regeneration. The determination of levels of

uptake of magnetically labeled substrates by living cells can be assessed by the measurement of magnetophoretic mobility [12]. There is considerable interest in the phagocytosis of nanomaterials [13], and nanomaterials used in MRI have magnetic cores [14]. Micro- and nanoparticles are ingested by cells by mechanisms dependent on particle size and surface composition including targeting moieties such as antibody labels [15] and can be ingested by a plethora of cell uptake mechanisms (phagocytosis, pinocytosis, receptor and non-receptor mediated endocytosis). Fluorescent labels modify the surface properties of most types of particles (with the possible exception of particles coated with fluorescent antibodies), whereas magnetic cores do not necessarily modify particle surface chemistry. One unintended consequence of labeling of blood and bone marrow with beads is the non-specific ingestion of labeling particles by phagocytic cells in the environment either by direct uptake or by released endocytotic vesicles [16]. In this study a commercial velocimeter was used to measure magnetophoretic mobility distributions in two example applications: flowing magnetic cell separation and nanoparticle phagocytosis. The adequacy of tumor cell labeling to meet the requirements of a particular flowing separator was established, and the kinetics of starch-particle phagocytosis were characterized.

* Corresponding author.

E-mail addresses: ptodd@hotmail.com, ptodd@techshot.com (P. Todd).

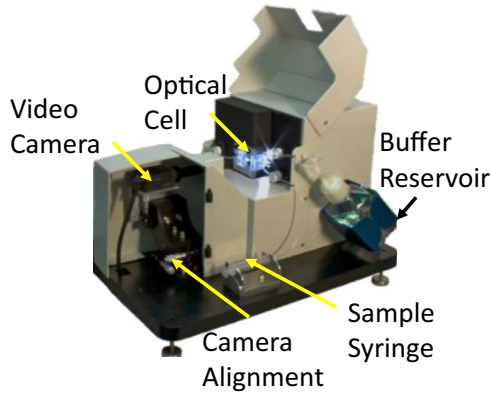


Fig. 1. Labeled photograph of the Hyperflux™ magnetic velocimeter demonstrated in this study.

2. Experimental

2.1. Cells

The tumor cell line used in all tests is CRL-211, DT40, obtained from ATCC, a chicken B-cell lymphoma cell line. These cells were maintained in suspension culture by twice-weekly passage in culture medium consisting of 69% Dulbecco's modified eagle's medium (DMEM), 10% tryptose phosphate broth solution, 5% chicken serum, and 1% ABAM (Antibiotic-Antimycotic mixture, all produced by SIGMA™, St. Louis, MO, USA, plus 10% fetal bovine serum (FBS) produced by ATCC. Cells were counted by hemacytometer and diluted in Dulbecco's phosphate-buffered saline (PBS) to about 5×10^4 cells/mL for reaction with bead reagent and evaluation in the Hyperflux™ velocimeter.

CHO Cells (Chinese Hamster Ovary cells, line CHO-K1) were maintained in monolayer culture in T-75 flasks at a passage ratio of about 1:8 every two days. For endocytosis experiments cells were trypsinized and counted for plating at about 1×10^6 cells per well in 6-well plates and incubated at 37 C for one day. They were then switched to complete medium containing various concentrations of magnetic nanoparticles for various times from 1 to 24 h. They were then trypsinized and suspended in Hanks' Balanced Salts Solution for analysis using materials and protocols as previously described [17].

2.2. Particles

Medium to high mobility particles were required for tumor cell labeling for the separator proposed for use. Beads were magnetically selected according to manufacturer's instructions before and after antibody labeling. The antibody used is Mouse monoclonal M-1 Anti-Chicken IgM mu chain (Biotin), Abcam™ product id ab99719. Labeling of beads with this antibody was achieved before mixing particles with cells following manufacturers' instructions. Magnetic beads used in the testing are 2.8 μm diameter Dynabeads® Biotin Binder (Invitrogen/Dynal) with measured magnetophoretic mobility range of $1.3\text{--}2.0 \times 10^{-11} \text{ m}^3/\text{TAs}$, the concentration of beads is 4×10^8 beads/mL. Nonspecific particle internalization was avoided by reacting label with cells at 8 C or 23 C. Phagocytosis (deliberate internalization) studies utilized 50 and 100 nm superparamagnetic iron-oxide nanoparticles with magnetite core and starch matrix and coating (Chemicell FluidMAG-D, Berlin, Germany, Article Number: 4101-1 (1 mL)) [16]. The concentration of nanoparticles is expressed as $\mu\text{g/mL}$ of iron.

2.3. Magnetophoretic mobility measurement

Magnetophoretic mobility is the ratio of the terminal velocity of the particle, v_m , to the gradient of the magnetic energy, $\frac{\nabla B_0^2}{2\mu_0}$, with B being the local magnetic flux density at the point of the particle or cell:

$$U_m = v_m / \frac{\nabla B_0^2}{2\mu_0} \quad (1)$$

The units of U_m are $\text{m s}^{-1}/\text{T A m}^{-2}$ or $\text{m}^3\text{T}^{-1} \text{A}^{-1} \text{s}^{-1}$ (meters cubed per Tesla-Ampere-second), expressed in this work as m^3/TAs . The Hyperflux™ velocimeter (IKOTECH, LLC, New Albany IN, USA) measures v_m by image velocimetry and divides it by the denominator in Eq. (1), which is an adjustable constant in the velocimeter software. The Hyperflux™ image velocimeter, in brief, consists of a stopped-flow sample cell connected to sample, supply and waste fluid reservoirs and served by an automated pump, which transfers a fresh volume of sample into the optical cell after each "set" of a specified number of video frames has been recorded by a high-resolution camera. Raw video frames are maintained in a file that can then be analyzed using operator-selected parameters, especially including an intensity threshold setting that is adjusted interactively on the basis of simultaneous image and graphical display. For every recorded event at least 20 parameters are calculated and stored including velocity, magnetophoretic mobility, size, shape and image processing parameters. Additional details are given in [18], and a view of the Hyperflux™ velocimeter is given in Fig. 1. An example of a data display screen is shown in Fig. 2.

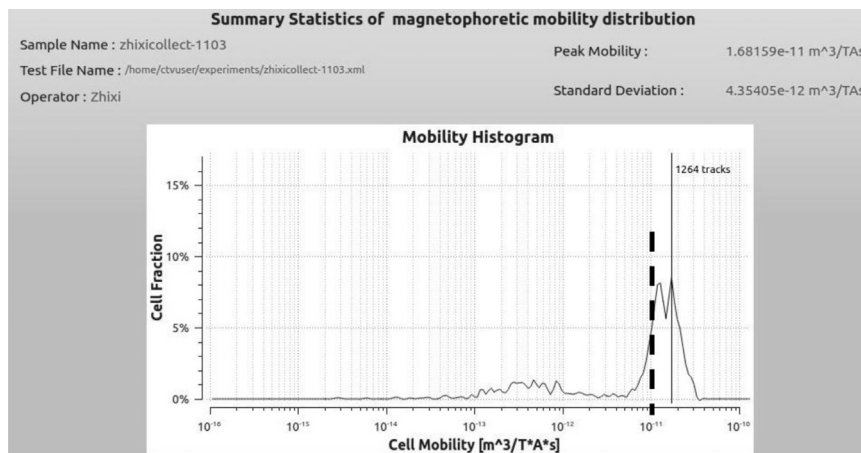


Fig. 2. Screen shot of mobility histogram generated automatically by the Hyperflux™ velocimeter for magnetically labeled chicken lymphoma cells. Vertical solid line indicates peak mobility. Vertical dashed line indicates minimum magnetophoretic mobility ($1.3 \times 10^{-11} \text{ m}^3/\text{TAs}$) for 100% capture of cells in a modeled cell separator flowing at 1.0 mL/min.

3. Results and Discussion

3.1. Magnetophoretic mobility of tumor cells labeled for flowing separation

Magnetophoretic mobility distributions were determined on the basis of several thousand analyzed cell tracks, and an example is given in Fig. 2, a screen shot of the Hyperflux™ velocimeter output. For the flowing magnetic separator in question, a compact multistage capture device with a desired flow rate of 1.0 mL/min, the minimum required magnetophoretic mobility for 100% cell capture was calculated to be $1.3 \times 10^{-11} \text{ m}^3/\text{TAs}$. This is marked as a dashed vertical line in Fig. 2. From the mobility data set it may be calculated that the separator in question would capture about 90% of the labeled cells.

3.2. Magnetophoretic mobility and nanoparticle phagocytosis

In order to use magnetophoretic mobility as a robust indicator of particle ingestion, instrument settings that provide reproducible results were established. The most significant operator-controlled setting is a threshold intensity value used by the Hyperflux™ image analysis package to accept or reject imaged objects for calculation of their average magnetophoretic mobilities. The range of intensity values is 0–255. In Fig. 3 it is seen that mid-range values, 130 and 190 for example, provide essentially reproducible mobility distributions for magnetically labeled CHO cells.

Cells were fed several concentrations (based on $\mu\text{g/mL}$ Fe) of 100 nm starch-coated Chemicell Fluid MAG-D magnetic particles for 24 h in kinetic studies, and mobility histograms were determined on the basis of velocities calculated from several thousand tracks.

Histograms of cells' magnetophoretic mobilities are given in Fig. 4. The clear trend to higher mobility is seen by visual comparison of the five histograms, and peak mobilities plotted vs. particle concentration in Fig. 5 follow a monotonic trend up to $200 \mu\text{g/mL}$ Fe. These observations using magnetophoretic mobility as a measurement of phagocytosis are consistent with quantifications using other, traditional chemical and cytological methods [17].

4. Conclusions

Labeled tumor cells have been magnetically characterized, and phagocytosis kinetics studies have been performed in a user laboratory by measuring magnetophoretic mobility distributions using the Hyperflux™ magnetic velocimeters. The ability of labeled tumor cells to be captured by a flowing cell separator was predicted. The kinetics of starch nanoparticle phagocytosis was characterized quantitatively, providing data suitable for theoretical model fitting. Such measurements can now be achieved on a rapid, convenient and routine basis using commercial instrumentation.

Acknowledgments

We thank Dr. Eugene Boland for setting up tumor cell culture and particle labeling protocols. Research support was provided by graduate research assistantships from Auburn University, and Dr. Y.S. Choi has been partially funded by a Department of Defense FY2012 Prostate Cancer Research Program (PCRP) Idea Development Award (Award #W81XWH-13-1-0288) and by a grant from the Auburn University Research Initiative in Cancer (AURIC). Statement of Interest: Dr. Hanley and Dr. Todd are former shareholders in IKOTECH, LLC.

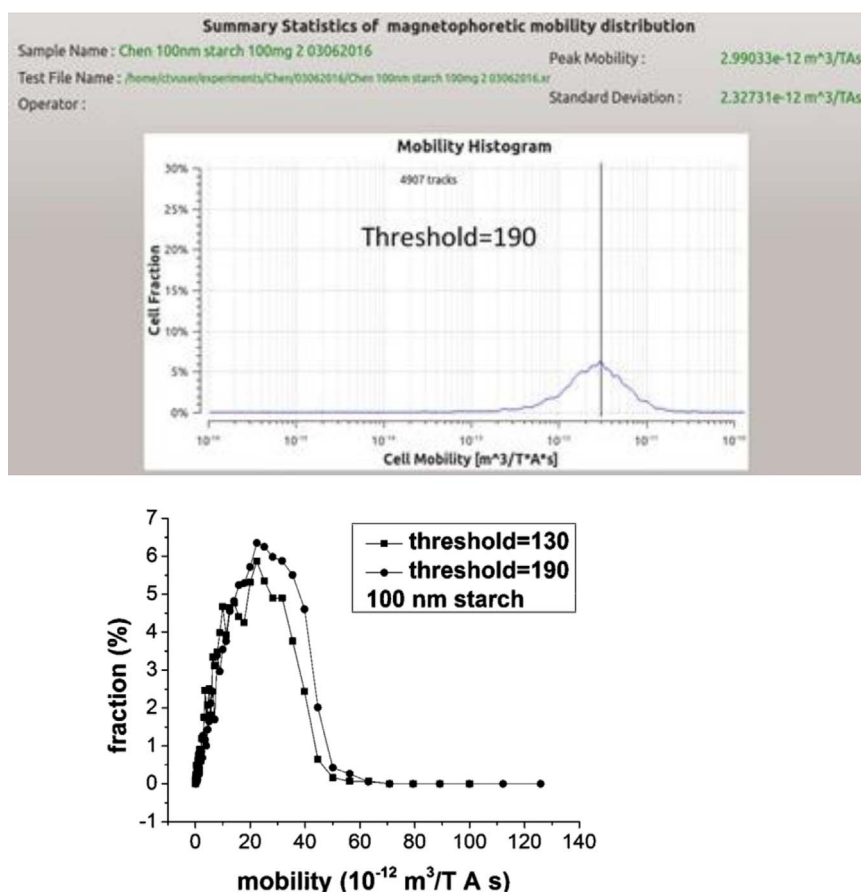


Fig. 3. Magnetophoretic mobility distributions of CHO cells labeled for 24 h with 100 nm starch-coated Chemicell Fluid MAG-D magnetic particles measured using two intensity threshold settings of the Hyperflux™ velocimeter. Top: Screen shot of image analysis data at Threshold=190. Lower: Mobility distributions at threshold =130 and 190 on a linear mobility scale.

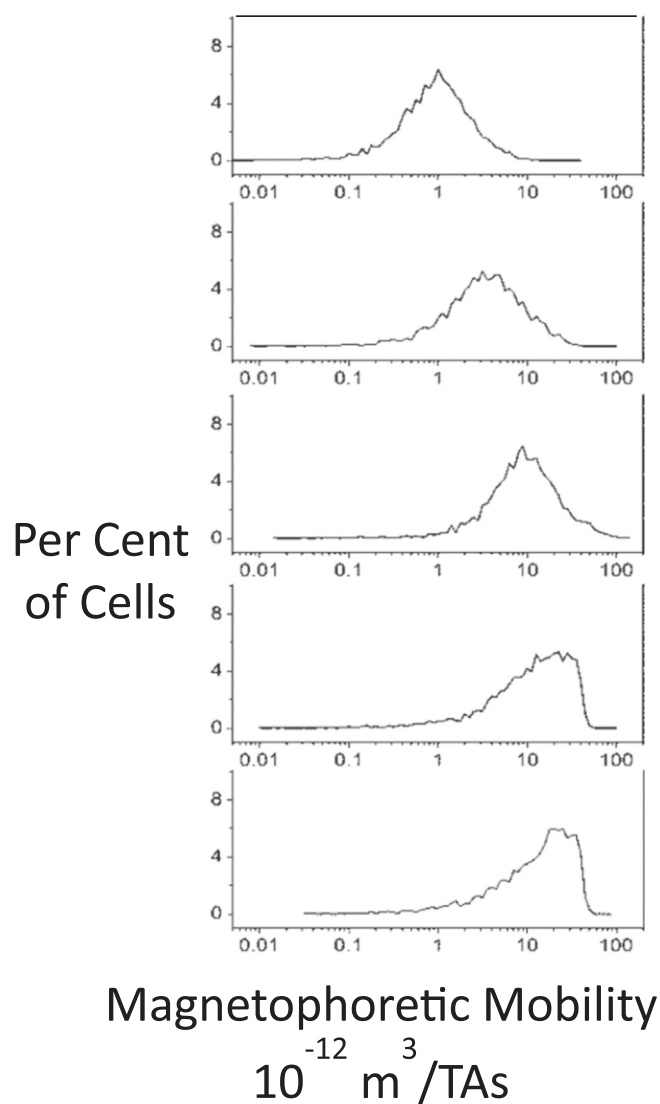


Fig. 4. Magnetophoretic mobility distributions of CHO cells labeled for 24 h with five concentrations of 100 nm starch-coated beads. There is a 15-fold increase in beads/cell over this concentration range. Unlabeled cells have no magnetophoretic mobility.

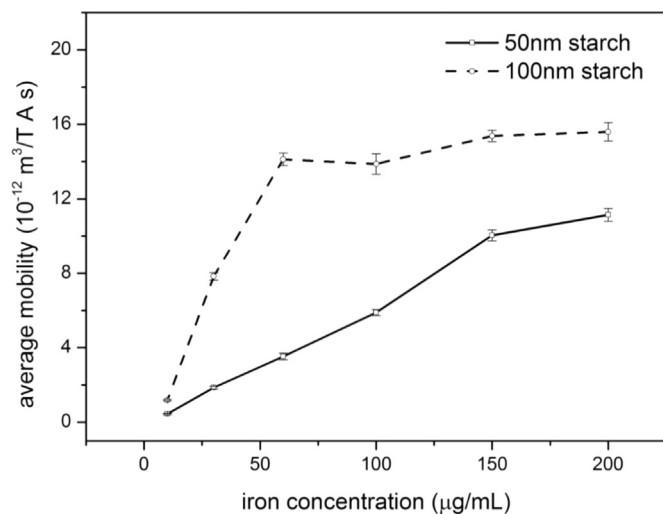
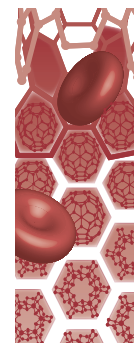


Fig. 5. Average magnetophoretic mobility of CHO cells that ingested five concentrations of 50 nm or 100 nm starch-coated beads vs. concentration of beads as measured by iron content.

References

- [1] H.M. Shapiro, *Practical Flow Cytometry*, 4th ed., Wiley, New York, 2003.
- [2] K.E. McCloskey, L.R. Moore, M. Hoyos, A. Rodrigues, J.J. Chalmers, M. Zborowski, *Biotechnol. Prog.* 19 (2003) 899–907.
- [3] D.J. Kennedy, P. Todd, S. Logan, M. Becker, K.K. Papas, L.R. Moore, *J. Magn. Mag. Mater.* 311 (2007) 388–395.
- [4] V.S.K. Sajja, T.R. Hanley, H. Gapsis, B. Guernsey, M. Taylor, D.J. Kennedy, M.J. Taylor, K.K. Papas, P.W. Todd, *Biotechnol. Bioeng.* 108 (2011) 2107–2117.
- [5] L.M. Reece, L. Sanders, D. Kennedy, B. Guernsey, P. Todd, J.F. Leary, *Proc. SPIE* 7568 (2010) 75680P.
- [6] S.S. Yen, A. Rembaum, R.S. Molday, *Cell Sorting Apparatus*, US PATENT 4,219,411, 1980.
- [7] R.S. Molday, S.P.S. Yen, A. Rembaum, *Nature* 268 (1977) 437–438.
- [8] Y. Zhang, R.W. Barber, D.R. Emerson, *Curr. Anal. Chem.* 1 (3) (2004) 345–354.
- [9] V.S.K. Sajja, D.J. Kennedy, P.W. Todd, T.R. Hanley, *Canad. J. Chem. Eng.* 89 (2011) 1068–1075.
- [10] M. Nakamura, K. Decker, J. Chosy, K. Comella, K. Melnick, L. Moore, L.C. Lasky, M. Zborowski, J.J. Chalmers, *Biotechnol. Prog.* 17 (2001) 1145–1155.
- [11] D.F. Hayes, et al., *Clin. Cancer Res.* 12 (2006) 4218–4224.
- [12] K.E. McKloskey, M. Zborowski, *Cytometry* 40 (2000) 307–315.
- [13] A.J. Cole, A.E. David, J.X. Wang, C.J. Galban, H.L. Hill, V.C. Yang, *Biomaterials* 32 (2011) 2183–2193.
- [14] A. Lindemann, K. Ludtke-Buzug, B.M. Fraderich, K. Grafe, R. Pries, B. Wollenberg, *Int. J. Nanomed.* 9 (2014) 5025–5040.
- [15] C. Rosales, *Molecular Mechanisms of Phagocytosis* (Chapter 2), Steven Greenberg, Springer, New York, 2005.
- [16] A.K. Andriola Silva, C. Wilhelm, J. Kolosnjaj Tabi, F. Gazeau, *Pharm. Res.* 29 (2012) 1392–1403.
- [17] C.C. Hanot, Y.S. Choi, T.B. Anani, D. Soundararajan, A.E. David, *Int. J. Mol. Sci.* 17 (2016) 15–27.
- [18] C. Zhou, E.D. Bolland, P.W. Todd, T.R. Hanley, *Cytom. Part A* 89A (2016) 589–593.



Nanoparticle-based probes to enable noninvasive imaging of proteolytic activity for cancer diagnosis

Proteases play a key role in tumor biology, with high expression levels often correlating with poor prognosis for cancer patients – making them excellent disease markers for tumor diagnosis. Despite their significance, quantifying proteolytic activity *in vivo* remains a challenge. Nanoparticles, with their ability to serve as scaffolds having unique chemical, optical and magnetic properties, offer the promise of merging diagnostic medicine with material engineering. Such nanoparticles can interact preferentially with proteases enriched in tumors, providing the ability to assess disease state in a noninvasive and spatiotemporal manner. We review recent advances in the development of nanoparticles for imaging and quantification of proteolytic activity in tumor models, and prognosticate future advancements.

First draft submitted: 20 January 2016; Accepted for publication: 23 May 2016; Published online: 28 July 2016

Keywords: cancer diagnosis • imaging probes • *in vivo* imaging • molecular imaging • proteases • surface modification • tumor microenvironment

It is predicted that by 2030 there will be more than 22 million new cancer cases each year worldwide [1]. Successful management of cancer hinges on its early and accurate detection and subsequent treatment [2]. In many instances, both diagnosis and treatment planning rely on data gathered through biomedical imaging techniques. Conventional anatomical imaging modalities, which include magnetic resonance imaging (MRI), ultrasound and computed tomography, provide morphological information on the location and size of tumor lesion. Anatomical imaging, however, lacks specificity and sensitivity [3], and provides no information about abnormalities at the cellular and molecular level [4]. As a result, clinically utilized anatomical imaging techniques only detect tumors when the lesion diameter exceeds approximately 1 cm, at which point the tumor comprises more than a billion cells [5]. Molecular imaging, on the other hand, offers the potential to visualize and quantify the

molecular and cellular processes associated with early stages of disease progression and its remission [6]. For example, differential physiological characteristics, which include the overexpression of several cell receptors such as EGFRs [7], low pH, hypoxia and increased proteolytic activity, between tumor and normal tissues can be exploited in the development of tools for diagnosis and monitoring of disease state [6,8,9].

Imaging of tumor proteolytic activity is attractive for several reasons: protease expression can be elevated at even the early stages of tumor progression [10]; catalytic amplification provides for enhanced sensitivity [11]; the potential for improved signal-to-noise ratio through ON/OFF switching of probes by proteolytic activity; and the presence of proteases at the invasive front of tumors and at sites of angiogenesis – regions readily accessible to imaging probes [12]. Tumor progression and invasion makes significant use of proteases at the primary and meta-

Tareq Anani¹, Peter Panizzi² & Allan E. David^{*1}

¹Department of Chemical Engineering, Samuel Ginn College of Engineering, 212 Ross Hall, Auburn University, Auburn, AL 36849, USA

²Department of Drug Discovery & Development, Harrison School of Pharmacy, 4306 Walker Building, Auburn University, Auburn, AL 36849, USA

*Author for correspondence:

Tel.: +334 844 8119

Fax: +334 844 2063

aedavid@auburn.edu

Future
Medicine

part of
fsg

static sites [2]. In addition to degrading the extracellular matrix, proteases release growth factors and chemokines, which directly or indirectly affect tumor invasion, and they also activate latent proteins on the cell surface [13]. Matrix metalloproteinases (MMP), a family of extracellular, zinc-dependent enzymes involved in extracellular matrix remodeling, are of special interest as their increased activity is associated with the aggressiveness of many cancers [14,15]. Other proteases, including the lysosomal cysteine protease cathepsin B and the serine protease urokinase-type plasminogen activator have also been implicated in tumor progression [16].

Numerous molecular probes, including those based on peptides [17,18], polymers [19,20], polymeric nanoparticles [21,22], protein nanoparticles [14] or inorganic nanoparticles [23–25], have been developed to image proteolytic activity. Recent interest in nanoparticle-based probes to quantify *in vivo* proteolytic activity is driven by attempts to overcome the limitations of small molecule probes, which tend to have poor pharmacokinetics, high background noise due to nonspecific uptake by tissues and relatively poor detection limits [26]. Nanoparticles are able to overcome some of these limitations due to their size and vast surface area, which is readily functionalized with imaging agents for molecular imaging, cell targeting ligands for active targeting of the tumor site, and biocompatible surface coatings that can modulate pharmacokinetics and biodistribution [27]. Each nanoparticle has the potential to deliver numerous imaging agents, which enhances sensitivity for detection of the targeted molecular event [28]. Proper sizing of nanoparticles can also lead to preferential accumulation at tumor sites due to the enhanced permeability and retention effect [10,29]. Nanoparticles can also be designed to change size, charge and/or surface coating in response to environmental cues in order to optimize transport across the many physiological barriers encountered *in vivo* [9].

The various types of probes discussed in this review are summarized in **Table 1**. This discussion is focused on nanoprobe that provide the potential for noninvasive, spatial and temporal imaging of *in vivo* biological activity in tumor microenvironments [30].

Magnetic resonance imaging

MRI is a noninvasive imaging modality that provides high spatial resolution and deep-tissue imaging [32,48]. Hydrogen protons, which are most frequently imaged in MRI because of its abundance, are normally found in the body with their spin axes randomly aligned. When exposed to a strong magnetic field, the spin axes of protons align with the applied field, which is the low energy state for the system. This alignment is then displaced by application of a radiofrequency pulse,

which excites the protons to a higher energy level. Subsequent relaxation of the excited nuclei back into alignment with the applied magnetic field is characterized by a relaxation time, which varies based on tissue properties and is the means for discrimination between healthy and malignant tissues [50,51]. Contrast agents are used to improve the sensitivity and contrast of MR images by shortening either the T_1 (longitudinal) or T_2 (transverse) relaxation times. Standard MRI contrast agents used in the clinic are gadolinium chelates (T_1) and magnetic nanoparticles (T_2) [48]. Some clinical success has been achieved with magnetic nanoparticles as targetable MRI contrast agents [29]. The high magnetic susceptibility of iron oxide cores leads to noticeable enhancement of transverse (T_2 and T_2^*) relaxivity, which is observed as a darkening of T_2 -weighted MR images (hypointensity) [52].

While MRI allows for whole-body imaging [32], it generally suffers from poor sensitivity for measuring molecular events [53]. Since magnetic susceptibility and r_2 -relaxivity depend on particle size, the growth of single iron oxide crystals into larger aggregate structures is one method that has been explored to enhance the sensitivity of T_2 -weighted MRI. Growth of particle size, however, can also negatively affect the pharmacokinetic properties and biodistribution of the particles. A potential strategy to overcome this problem is to design particles that are initially stable in the blood but which then form aggregates in response to proteolytic activity. One approach utilizes two sets of complementary, colloidally stable superparamagnetic iron oxide nanoparticles (SPIONs) that only self-assemble in response to proteolytic cleavage, as depicted in **Figure 1**. To accomplish this, Gallo *et al.* designed two families of SPIONs that undergo a bi-orthogonal, copper-free click conjugation following MMP cleavage [25]. The nanoparticles were tagged with cyclopentapeptide, a C-X-C chemokine receptor type 4 (CXCR4) targeting ligand, for enhanced targeting of metastatic tumors, an MMP 2/9 cleavable peptide (PLGMWSR), PEG for enhanced *in vivo* stability, and either azide or alkyne moieties. The particles were colloidally stable in the absence of MMP 2/9, but proteolytic cleavage exposed the alkyne and azide moieties, which led to a [3+2] cycloaddition reaction that crosslinked the particles and altered magnetic relaxivity. Simultaneous administration of the two SPIONs in tumor-bearing mice displayed T_2 signal enhancement, which dropped significantly with inhibition of MMP.

The ability to simultaneously monitor the activity of multiple molecular targets associated with a given disease has tremendous diagnostic value. Von Maltzahn and colleagues developed a nanoprobe capable of simultaneously monitoring the activity of two

Table 1. Summary of nanoparticle-based systems for imaging *in vivo* proteolytic activity.

Imaging modality	Target proteases	Nanoparticle type	Ref.
MRI			
¹ H MRI	MMP-2, -7, -9 and -14, and legumain	SPION	[25,31–34]
¹⁹ F MRI	Legumain	¹⁹ F nanoparticles	[35]
Optical imaging			
Prequenched fluorophores	MMP, cathepsin B, caspase-3, -8 and -9, matriptase, trypsin and uPA	Ferritin protein, glycol chitosan, AuNP and Au-Fe ₃ O ₄ nanocomposites	[14,21,36–41]
Bioluminescence	Trypsin, MMP-2 and caspase-3	Poly (phenylene ethynylene) nanoparticles, AuNP and UCNPs	[42–44]
Theranostic nanoparticles	MMP	AuNP and AuNR	[45,46]
Photoacoustic	MMP	Copper sulfide	[47]
Secondary Cerenkov-induced fluorescent imaging	MMP-2	AuNP	[23]
Multimodal imaging			
MRI/optical	MMP	SPIONs and Gadolinium-labeled dendrimeric nanoparticles	[12,23,48]
PET/optical	MMP	⁶⁴ Cu-radiolabeled glycol chitosan	[49]
CT/optical	MMP	AuNP	[24]

AuNP: Gold nanoparticle; AuNR: Gold nanorod; MMP: Matrix metalloproteinase; SPION: Superparamagnetic iron oxide nanoparticle; UCNPs: Lanthanide-doped upconversion nanoparticle; uPA: Urokinase-type plasminogen activator.

matrix-metalloproteinases, MMP-2 and MMP-7 [31]. The SPIONs were designed to aggregate in response to logical ‘AND’ or ‘OR’ functions, causing an amplification of the T_2 relaxation rate and enabling MRI-based detection. In the AND case, two sets of nanoparticles, one with an MMP-2 specific substrate (GPLGVRG) and biotin and the other with an MMP-7 substrate (VPLSLTM) and neutravidin, self-assembled by biotin-neutravidin interactions only if both enzymes were present. In the OR case, two sets of nanoparticles, one having both MMP substrates in series and tethered with biotin while the other nanoparticle was tethered with only neutravidin, would self-assemble in the presence of either one or both proteases.

A significant limitation of the enzyme-activated MRI-nanoprobes discussed so far is that they require separate sets of SPIONs, which can exhibit different circulation times and biodistribution patterns *in vivo*. The co-delivery issue can be eliminated if a single nanoparticle is used. Schellenberger *et al.* designed protease-specific iron oxide nanoparticles (PSOP), which upon activation by MMP-9, switch from an electrostatically stabilized, low-relaxivity stealth state to aggregating, high- T_2^* relaxivity particles [32]. Initially, peptides comprising an arginine-rich coupling domain with an MMP-9-cleavable domain linked by a glycine bridge (NH₂-GGPRQITAG-K(FITC)-GGGG-RRRRR-G-RRRRR-amide) were reacted with amine-reactive *N*-hydroxysuccinimide-methyl-

PEG (NHS-mPEG). The resulting positively charged mPEG-peptide was electrostatically adsorbed onto the surface of negatively charged citrate iron oxide particles to yield PSOP. Cleavage of the peptide by MMP-9 results in the release of PEG and a loss of steric stabilization, causing aggregation due to both magnetic attraction as well as the electrostatic attraction between the positively charged arginine-rich coupling domain and the negatively charged citrate coat, as shown in **Figure 2**. While the probes discussed so far perform well in an *in vitro* setting, their *in vivo* application is limited by our inability to determine whether the increase in MRI contrast is due to proteolytic cleavage and subsequent aggregation of particles or if it is simply due to increased accumulation of particles at the target site, thus complicating quantitative analysis.

In one application, activity of the protease legumain was utilized to tag tumor-associated macrophages (TAM) with magnetic nanoparticles. Legumain is a lysosomal/vacuolar cysteine protease that cleaves substrates at the C-terminal of asparagine, and is overexpressed in prostate, breast and colon cancers [54,55]. TAMs overexpress legumain on their surface and play an important role in the progression of certain cancers [56,57]. Yan *et al.* designed a Y-shaped legumain-targeting peptide (Y-Leg) with the sequence AANLHK(HK)₂ and grafted it onto oxidized carbon nanotubes (OCNTs) loaded with Fe₃O₄ nanoparticles for *in vivo* targeting and MRI of TAMs [33]. T_2^* -

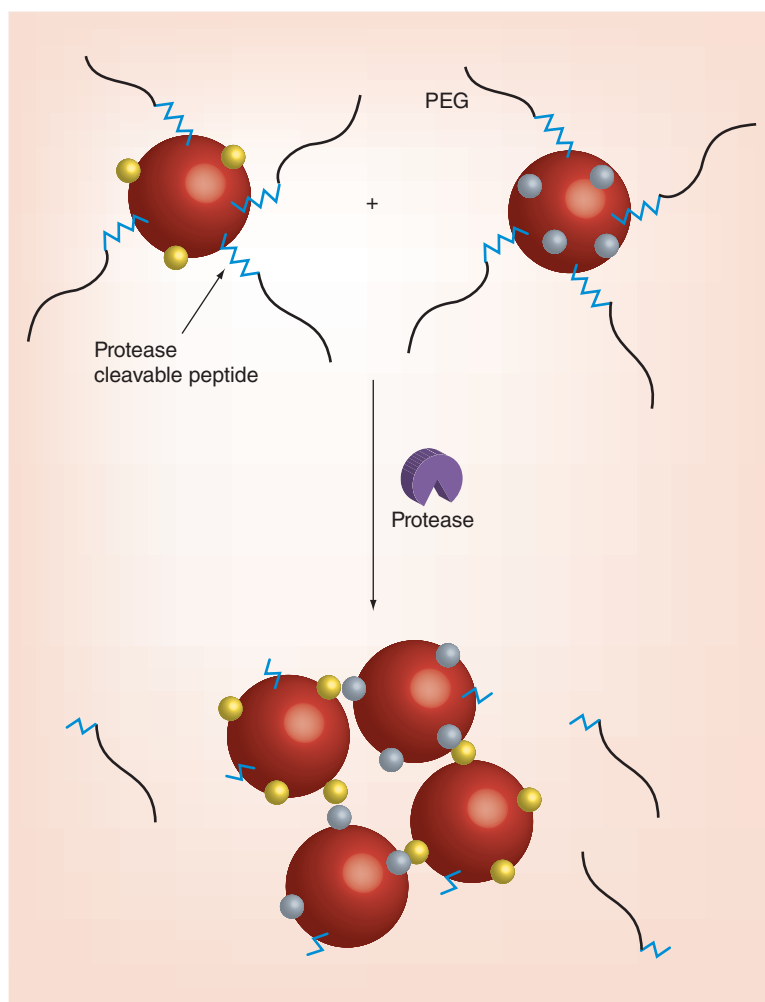


Figure 1. Two sets of complimentary, sterically stabilized iron oxide nanoparticles aggregate (e.g., through neutravidin/biotin interactions) following proteolytic cleavage of peptide substrate and removal of polyethylene glycol (PEG). Cluster formation enhances magnetic susceptibility and r_2 relaxivity to allow MRI detection of proteolytic activity.

weighted MRI images following intravenous administration of Y-Leg-OCNT/ Fe_3O_4 to 4T1 tumor-bearing mice revealed targeting of the nanotubes toward the TAM-infiltrated tumor microenvironment. On the other hand, control peptide-conjugated nanotubes showed no significant change in the MRI signal.

Chemotherapeutics are hindered by undesired systemic toxicity to healthy tissues. Ansari and colleagues developed an MMP-14 activatable theranostic probe (TNP) based on US FDA approved ferumoxytol nanoparticles conjugated to an MMP-14 cleavable peptide conjugate of azademethylcolchicine, a tumor vasculature-disrupting agent, for tumor-selective therapeutic delivery [34]. The probe allowed for simultaneous MRI imaging of TNP tumor accumulation and protease-specific drug activation. MRI scans following intravenous injection to MMP-14 positive, MMTV-

PyMT mammary tumor-bearing mice indicated significant accumulation of the theranostic probe at the tumor site, and a significant antitumor effect and tumor necrosis, with no detectable toxicity and MRI signal in healthy tissues. It is important to note, however, that the MRI images indicated TNP delivery but not drug activation.

Due to the abundance of hydrogen protons and the scarcity of intrinsic ^{19}F atoms in the body, ^{19}F MRI provides better contrast-to-noise ratio than ^1H MRI. Yuan *et al.* designed a ^{19}F nanoparticle contrast agent which self-assembles intracellularly in the presence of glutathione (GSH) and disassembles in the presence of legumain [35]. The 'off' and 'on' ^{19}F NMR/MRI signal was used to detect legumain activity in HEK 293T tumor-bearing zebrafish, which showed a strong signal compared with healthy zebrafish.

Optical imaging

Optical imaging detects photons emitted by fluorescent or bioluminescent contrast agents, and can simultaneously image multiple contrast agents depending on their excitation/emission spectra. Near infrared fluorescence (NIRF) imaging has become increasingly important for visualizing important *in vivo* processes occurring at the cellular and molecular levels [58]. NIRF offers several advantages over visible-range optical imaging, including lower light scattering and lower absorption by endogenous biomolecules that strongly absorb visible (e.g., hemoglobin) and infrared light (e.g., water and lipids), leading to deeper tissue penetration [59,60]. The specificity of NIRF imaging can be substantially improved by utilizing fluorescently quenched, peptide-based activatable probes. These probes emit little fluorescence in their native state, but become highly fluorescent in the presence of a target proteases [58]. The quality of an NIRF probe for imaging of *in vivo* proteolytic activity is determined by the efficiency of its quenching, its quantum yield, the target-to-background ratio, probe targeting and pharmacokinetics, protease specificity and the probe's photostability in physiological conditions [3,41]. The following section examines the various strategies to detect proteolytic activity *in vivo* utilizing optically active nanoprobe.

Prequenched fluorophores

The majority of probes developed for optical imaging of *in vivo* proteolytic activity utilize one or more fluorescence quenching effects that include self-quenching, fluorescence resonance energy transfer (FRET), or energy transfer between dye and nanoparticle surface to reduce the preactivation fluorescence signal. Fluorescence is recovered following release of the quencher or

dye by proteolytic activity. High quenching efficiency is essential for an effective probe.

FRET

FRET is a process in which an excited fluorophore (donor) transfers its excitation energy to a nearby chromophore (acceptor). The efficiency of FRET is strongly affected by the spectral overlap, dipole orientations and distance between the donor and acceptor. Separation of the two dyes causes a detectable change in signal, which is utilized to measure proteolytic activity [61]. Protease-activatable probes that employ FRET comprise an NIRF dye and quencher at both ends of a protease-specific peptide. Lin *et al.* developed two sets of ferritin protein cages, one with a fluorescently labeled MMP-specific peptide sequence (Cy5.5-GPLGVRGC) and another with black hole quencher (BHQ-3), that self-assemble to bring the energy donor and receptor into close proximity [14]. The ratio of donor and receptor that gave the highest fold increase in fluorescence following incubation with MMP was optimized and the probe validated following intratumoral injection *in vivo* against two MMP-positive cell lines, UM-SCC-22B and SCC-7.

Cathepsin B (CB), which normally remains in the intracellular lysosomal compartments, is secreted into the pericellular region in high amounts as cells gain metastatic potential [62]. Ryu *et al.* developed CB-activatable fluorogenic nanoprobe for early detection of metastases [36]. The nanoprobe was synthesized by conjugating a CB-responsive fluorogenic peptide substrate (GRRGKGG), which included a donor (Cy5.5) and a quencher (BHQ-3), onto the surface of tumor-targeting glycol chitosan nanoparticles. The probe displayed strong specificity to CB, compared with cathepsin L, cathepsin D and CB plus inhibitor, and was also able to discriminate metastases in liver, lung and peritoneal metastatic mouse models.

Simultaneous imaging of multiple proteolytic activities has the potential to provide a more complete map of disease progression. Park *et al.* developed various caspase substrate-linked fluorescent proteins immobilized on gold nanoparticles (AuNP-FPs) for real-time simultaneous detection of multiple caspase activities in cancer cells during apoptosis [37]. AuNP served as a broad-spectrum fluorescence quencher. As shown in Figure 3, AuNP-FPs were designed to release blue-, red- and yellow-fluorescent protein following activation by caspase-8 (IETD), caspase-9 (LEHD) and caspase-3 (DEVD), respectively, where the peptide sequence in brackets indicates the caspase cleavage site. While this is a promising approach to quantify multiple proteases, only *in vitro* results have been presented to date.

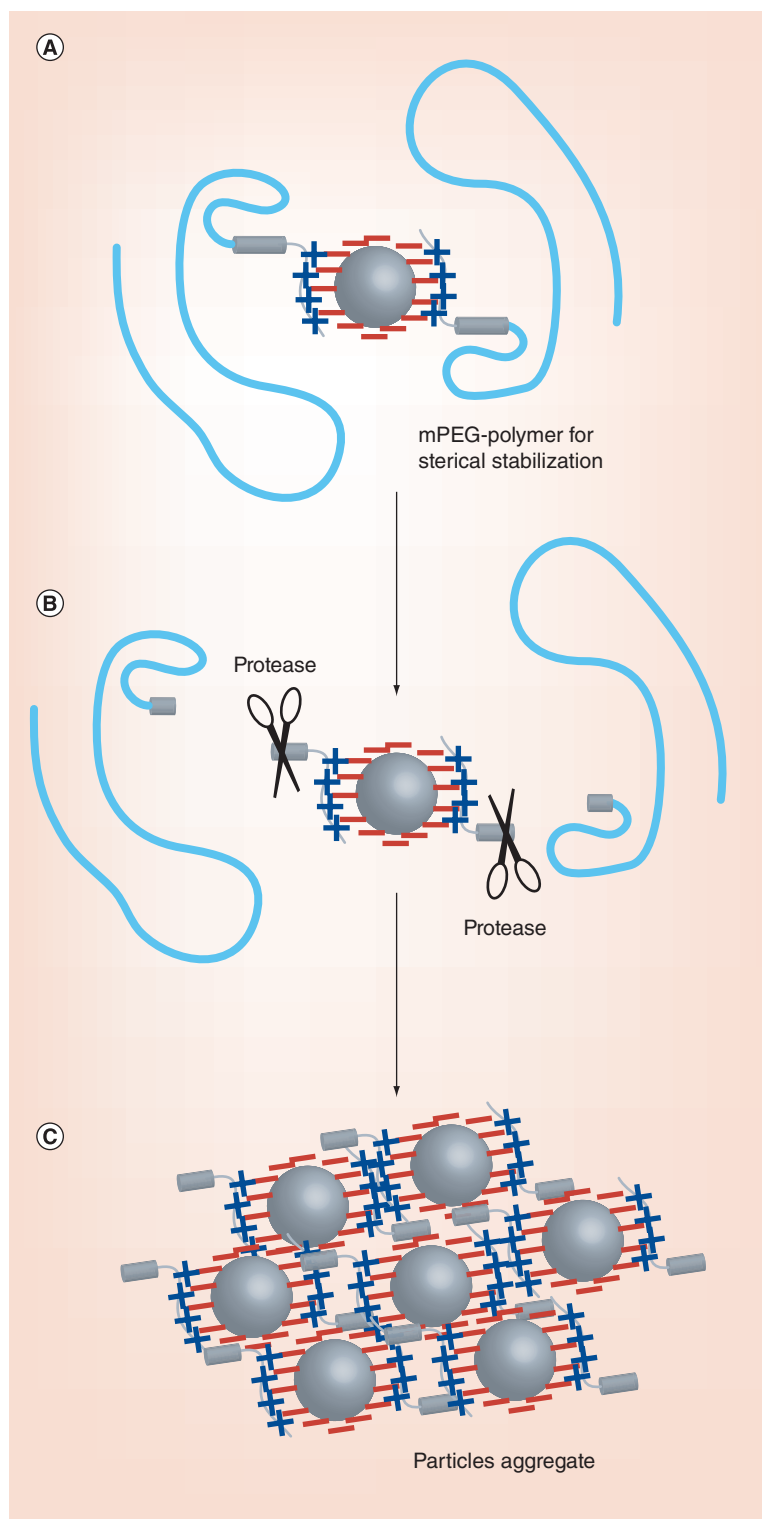


Figure 2. Sterically stabilized protease-specific iron oxide nanoparticles release peptide-mPEG in the presence of MMP-9, resulting in a loss of steric stabilization and enabling aggregation due to both magnetic attraction as well as electrostatic attraction between the positively charged arginine-rich coupling domain and the negatively charged citrate coat.

Reproduced with permission from [32].

Quenching by gold nanoparticles

Strong electronic interactions with chromophores near the surface make gold nanoparticles (AuNPs) very efficient quenchers of molecular excitation energy [63], with larger quenching distances (~20 nm) compared with FRET [39]. Deng *et al.* developed spherical and rod-shaped AuNPs for detection of *in vivo* matrilysin, a type II transmembrane epithelial serine protease which activates several proenzymes including urokinase plasminogen activator (uPA) and MMPs associated with several cancers [38]. The expression of matrilysin is known to correlate with tumor staging, making it an excellent target for molecular imaging. The molecular beacon comprised a fluorescent dye attached to AuNPs through a matrilysin cleavable peptide substrate linker (GRQSRAGC). NIRF images of mice bearing matrilysin-expressing HT-29 tumor xenografts showed enhanced fluorescence recovery following intratumoral injection of the molecular beacon.

The success of AuNPs that rely on the thiol-gold chemistry is hampered in an *in vivo* setting, due to off-target site activation in the thiol-rich blood. To overcome this limitation, flower-like Au-Fe₃O₄ nanocomposites with a single Au core and several Fe₃O₄ petals, were developed as an MMP activatable fluorescence imaging probe [39]. The nanocomposite sensor, which can be tuned for shape, size and composition, combines the robust surface chemistry of Fe₃O₄ for conjugation of an MMP-specific peptide-dye (Cy5.5-GPLGVRG), with the excellent quenching properties of nearby Au. The flower-like shape of Au-Fe₃O₄ creates an architecture whereby the fluorophores on the Fe₃O₄ petals are in close proximity to the Au core for efficient quenching. Separate groups of SCC-7 xenograft tumor-bearing mice received injections of flower-like activatable nanoparticles (FANPs), with and without preinjection of MMP inhibitor, or gold-based activatable nanoparticles (GANPs). NIRF images for the FANP group showed high signal at the tumor site after 30 min, which increased gradually up to 4 h postinjection. Preinjection of an MMP inhibitor significantly reduced the observed signal. Meanwhile, the GANP control group showed a weak optical signal in the tumor after 4 h (Figure 4).

Combination of different quenching mechanisms

The efficiency of quenching is enhanced by combining different quenching mechanisms into a single probe. In one example, self-quenching and FRET were combined in an MMP-responsive nanosensor for NIRF imaging of MMP [21]. The nanosensor comprised a self-assembled chitosan nanoparticle and an activatable MMP-specific peptide sequence with the NIRF dye Cy5.5 and dark

quencher BHQ3 (Cy5.5-GPLGVRGK(BHQ3)-GG) to create a FRET pair. NIRF of Cy5.5 was quenched by both the interaction of the dye with BHQ-3 and dye-dye self-quenching mechanism. High recovery of Cy5.5 fluorescence signal was observed *in vivo*, as evidenced by fluorescence tomography following intravenous administration of the nanosensor in an MMP-positive SCC-7 xenograft tumor and correlated with levels of active MMPs. Meanwhile, the signal was attenuated when animals were pretreated with an MMP-inhibitor. To determine response to tumor size, the nanosensor was intravenously injected into mice carrying SCC-7 tumors of varying sizes, between 3.5 and 381.5 mg. After 2 h, the animals were euthanized and the excised tumors analyzed by measuring fluorescence intensity, which was found to increase proportionally with tumor size (Figure 5A). MMP-2/9 activities were also quantified using gelatin zymography, and correlated strongly with the NIRF signal intensity (Figure 5B).

Lee and colleagues developed an MMP protease-sensitive probe with AuNPs and Cy5.5 linked together through an MMP-cleavable peptide substrate (Cy5.5-GPLGVRGC-amide) [40]. The combination of AuNP surface and close proximity of Cy5.5 induced a strong multi-quenching effect on the fluorescence of Cy5.5. Upon exposure to MMPs, the peptide was cleaved, releasing free Cy5.5 and recovering the NIRF signal, as shown in Figure 6.

In another example, self-assembled heterogeneous monolayers of fluorophore (Quasar 670) and dark quencher (BHQ-2)-labeled peptide were adsorbed onto 20 nm AuNPs as an activatable probe for the detection of trypsin and uPA [41]. Fluorescence, attenuated due to self-quenching and FRET between Quasar 670 and BHQ-2, is restored following proteolytic cleavage. The probe displayed high fluorescence image contrast in a subcutaneous tumor phantom model in athymic nude mice.

Bioluminescence

A luminescence 'turn ON'-/turn OFF' system based on protease-responsive organic nanoparticles was developed and comprised a tightly packed, semiconducting poly (phenylene ethynylene) (PPE) core bearing perylene units and randomly inserted far red emissive dye (perylene) [42]. The probe also had an external, hydrophilic hydrogel coating with reactive succinimide groups. Aggregation induced quenching by tuning of the π -associations in the PPE core was accomplished by reacting the succinimide groups with a protease-sensitive peptide (KCRPLALWRSK), which leads to cross-linking of the shells of the nanoparticles (strained OFF state). Quenched luminescence was recovered upon exposure to the protease trypsin, which leads to highly

fluorescent noncrosslinked nanoparticles (ON state) with a 15-fold increase in luminescence.

Bioluminescence resonance energy transfer (BRET) offers several advantages over FRET-based systems, including larger differences in the emission spectra between the BRET donor and acceptor, high sensitivity and low background emissions. Kim *et al.* utilized the strong quenching properties of AuNPs (BRET acceptor) to silence the bioluminescence emission of *Renilla* luciferase [43]. Bioluminescence was recovered *in vitro* following 1-h incubation with MMP-2 and subsequent cleavage of an MMP-2 peptide linker substrate (IPVSLRSG).

Lanthanide-doped upconversion nanoparticles (UCNPs) can sequentially absorb multiple low-energy excitation photons to generate higher energy anti-Stokes luminescence [64]. UCNPs offer strong photostability, large anti-Stokes shifts and sharp emission bandwidths. Zeng *et al.* developed biostable luminescence resonance energy transfer (LRET) based UCNPs through facile peptide-mediated phase transfer to image proteolytic activity [44]. Oleic acid on the surface of UCNPs was displaced by chimeric peptides containing a polyhistidine-tag and a caspase-3 cleavage domain (DEVD). (H)₆-GDEVDAK-TAMRA-coated, caspase-3 responsive UCNPs were used to monitor the therapeutic efficacy of doxorubicin in a tumor mouse model. The upconversion luminescence (UCL) signal, which was collected between 450 and 600 nm (under 980 nm excitation), gradually increased the expression of light over a period of 12 h in DOX-treated tumors, as opposed to saline-treated tumors.

Theranostic nanoparticles in optical imaging

Multifunctional nanoplatforms that integrate *in vivo* imaging and drug delivery into a single theranostic nanoparticle (TNP) enable simultaneous visualization of probe biodistribution, therapy and response to treatment [65]. Prodrugs, which exploit the unique characteristics of the tumor microenvironment such as overexpressed proteolytic activity or pH, could be delivered for selective treatment of cancer cells while minimizing off-target toxicity [66,67]. The addition of imaging capability enables direct monitoring of the delivery and activation of the prodrug in the tumor microenvironment [68]. In one example, doxorubicin (Dox) was conjugated to AuNPs via an MMP-2 cleavable peptide substrate (CPLGLAGG) [45]. Fluorescence of Dox was quenched by AuNPs, and recovered following exposure to MMP-2. This switchable fluorescence property allowed for imaging of the activity of MMP-2 in tumor sites *in vivo*.

One disadvantage of incorporating both drugs and imaging agents on a nanoparticle is the competition

for space, which can lead to a less than optimal surface density and reduced imaging and therapeutic efficacy. Moreover, drug incorporation adds to the cost and difficulty of synthesis and purification [65]. One alternative is to take advantage of the intrinsic therapeutic ability of several types of nanoparticles [46]. The efficient absorption of light by gold nanorods (AuNR) and the subsequent conversion of that energy to heat make these particles good candidates for photothermal therapy [69]. Yi *et al.* developed a theranostic probe based on MMP-sensitive gold nanorods (MMP-AuNR) for simultaneous cancer imaging and photothermal therapy, as shown in Figure 7A [46]. A Cy5.5-labeled MMP substrate (Cy5.5-GPLGVRGC) was conjugated onto the surface of AuNR, which quenched NIRF. NIRF tomographic images of SCC-7 tumor-bearing mice after intratumoral injection of MMP-AuNR with and without inhibitor were taken and significantly greater NIRF signal was observed in the case when no inhibitor was added (Figure 7B). Additionally, following laser irradiation, the temperature of MMP-AuNR injected tumors increased up to 45° after 4 min (Figure 7C), which is sufficient to damage cancer cells, and coincided with *in vitro* results.

Photoacoustic imaging

Photoacoustic imaging (PAI) is an emerging technology that has the ability to provide structural, functional and molecular information of target tissues. PAI was developed as a means to overcome the scatter of signal from a source within an animal [70], a problem that

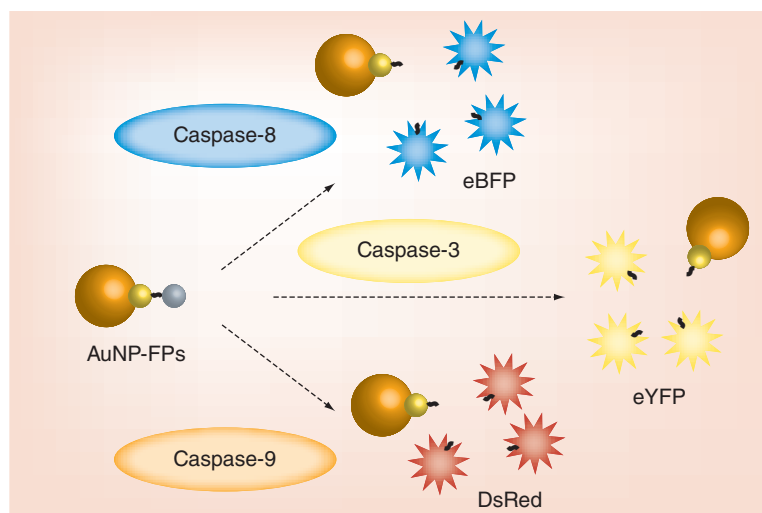


Figure 3. Fluorescent protein-conjugated gold nanoquenchers (AuNP-FPs) for simultaneous imaging of multiple caspase activities involved in apoptosis. AuNP-FPs were designed to release blue-, red- and yellow-fluorescent protein following activation by caspase-8, caspase-9 and caspase-3, respectively. Reproduced with permission from [37].

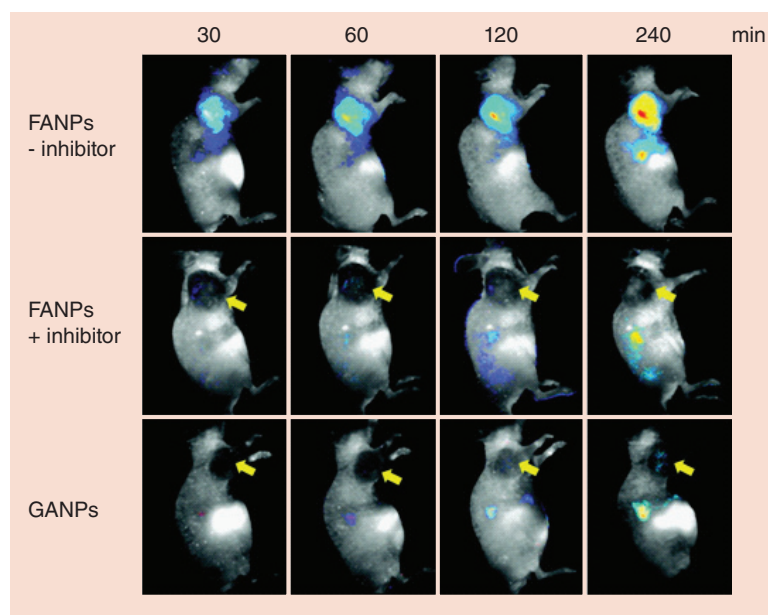


Figure 4. NIRF images following injection of flower-like activatable nanoparticles (FANPs), FANPs plus MMP inhibitor, or gold-based activatable nanoparticles (GANPs). The additional iron oxide phase incorporated into composite FANPs allowed higher loading of MMP-specific peptide-dye and better quenching properties, which resulted in higher NIRF signal in the tumor site. Reproduced with permission from [39].

dramatically reduces the resolution of optical imaging modalities. In general, PAI uses a focused excitation pulse to provide energy to target probes and cause them to enter the excited state. In doing so, the probes or endogenous molecules in tissue (e.g., hemoglobin) release a heat signature in the form of thermal expansion that results in an acoustic wave, which is detected by transducers and assembled by image reconstruction analysis [71].

Recently Yang and colleagues developed an activatable photoacoustic (PA) nanoprobe which comprised BHQ3 conjugated to 20 nm copper sulfide (CuS) nanoparticles via an MMP-cleavable peptide substrate (GPLGVRGKGG) [47]. The resulting CuS-peptide-BHQ3 (CPQ) probe displayed strong PA signals at 680 nm and 930 nm due to the strong optical absorbance of BHQ3 and CuS nanoparticles, respectively, which was used to distinguish the two components. It was hypothesized that MMP activity would disassociate BHQ3 from the CuS nanoparticles and lead to their rapid clearance from the tumor, due to their small size, while the larger CuS nanoparticles are retained. CPQ was intratumorally injected into mice bearing SCC7 tumors with and without MMP inhibitor. Ratiometric analysis of the PA signals (680/930 nm) showed MMP activity in the tumor; decreasing after 2 h in the case with no inhibitor, but remaining almost uniform when an MMP inhibitor was preinjected.

Other

NIRF signals obtained from *in vivo* lesions are a function of the intensity of incident light and the size and depth, from the surface, of the lesion. The observed signal will also depend on the proteolytic activity present in the lesion and the concentration of nanoprobe delivered, which complicates any attempt to quantify proteolytic activity *in vivo* [72]. A solution proposed by Scherer utilized a dual fluorochrome probe, in which polyamidoamine PAMAM-Generation 4 dendrimers were coupled to a Cy5.5 fluorophore-labeled, MMP7-cleavable peptide (RPLALWRS), to detect proteolysis (S, sensor) and AF750 as a noncleavable internal reference fluorophore, to monitor the total concentration (cleaved and uncleaved) of the reagent (R, reference), hence facilitating quantitative analysis [22]. The dye AF750 was also used as a quencher and its signal used to evaluate pharmacokinetics. The sensitivity of the probe was evaluated with two subcutaneous xenografted tumors on either flank of athymic nude mice that only differed in the expression of MMP7. Effective cleavage of Cy5.5 fluorophore in the tumor was calculated by dividing the sensor signal by that of the internal reference (S/R), a ratio that corrects for differences in the lesion size and depth. S/R increased over time and was consistently greater in MMP7 expressing tumors compared with control tumor.

Many of the probes discussed so far require post-synthesis modification, which causes variability in surface charge, payload and other characteristics. A controllable on-chip preparation of nanoprobe involved cadmium selenide quantum dot (CdSe QD) payload embedded into the hydrogel-like interior of MMP-responsive supramolecular gelatin nanoparticles (SGNs) to produce CdSe QDs encapsulated SGNs [73]. Self-assembly was done on a microfluidic device with hydrodynamic flow focusing, and the physiochemical properties were precisely controlled by changing the flow rates of the fluids. Degradation of the gelatin corona, upon exposure to MMP in the tumor, releases the QDs which can be subsequently internalized by cancer cells. *In vitro* cellular uptake by MMP secreting HT1080 cells was observed while addition of an MMP inhibitor decreased the fluorescence signal.

Thorek *et al.* utilized energy transfer between Cerenkov luminescence-emitting radionuclide and an activatable fluorescent AuNP probe for low background, secondary Cerenkov-induced fluorescent imaging (SCIFI) of MMP-2 activity [23]. The platform comprised FAM-labeled, MMP-2 cleavable peptide (IPVSLRSG) conjugated to AuNP, which quenched FAM fluorescence. Mice bearing SCC-7 xenografts were co-injected with [^{18}F]-FDG radionuclides and activatable AuNP. Cleavage of the peptide by MMP-2

at the tumor site releases the fluorophore, which is then excited by nearby [^{18}F]-FDG, leading to secondary Cerenkov-induced fluorescent conversion and detection by SCIFI.

Multimodal imaging

A growing trend in disease diagnosis is to synergistically combine several complimentary imaging modalities into a single platform, thus overcoming their individual limitations [24]. This has the potential to provide more complete information on disease pathology. Much research effort has been dedicated toward combining nanotechnology and molecular imaging to obtain a new generation of multimodal imaging nanoparticles. This section will look at the various multimodal, nanoparticle-based imaging probes developed thus far for imaging proteolytic activity *in vivo*.

MRI/optical

MRI provides excellent anatomical information and great tissue penetration but it has limited sensitivity, which hampers imaging of molecular events [53]. Optical imaging, on the other hand, provides excellent molecular imaging but weak anatomical information and limited tissue penetration [48,74]. Nanoprobes that can be imaged by both of these modalities could potentially provide excellent anatomical and molecular information. Iron oxide nanoparticles, which quench fluorescence, were fabricated with a thin silica coating (PCM-CS) that contained a Cy5.5-MMP substrate (Cy5.5-GPLGVRG) for MRI/NIRF dual imaging, with molecular (MMP) activity determined through optical imaging and anatomical information through MRI [53]. PCM-CS successfully visualized the tumor

regions in SC77 tumor-bearing xenografted mice using both imaging modalities. No NIRF signal was detectable in normal mice, whereas signal increased gradually in tumor-bearing mice up to 12 h, with NIRF intensity three- to four-times higher than in normal tissue. Administration of MMP-2 inhibitor 30 min before injection of PCM-CS significantly reduced NIRF signal. Noticeable darkening in T_2 -weighted MRI images appeared at 6-h postinjection in the tumor region as compared with the healthy muscle regions in the mice. While the decrease in MRI signal hit a maximum at 12 h, similar to the trend exhibited in the NIRF images, it should be noted that MRI and optical imaging were conducted on different mice.

Harris *et al.* developed a strategy for reversibly veiling a cell internalization domain on magnetofluorescent, dextran-coated iron oxide nanoparticles by shielding it with sterically protective, MMP-2 cleavable PEG (PEG-GK(TAMRA)GPLGVRGC) [12]. FITC was used to label the cell internalizing domain and thus track cellular internalization, while TAMRA-labeled peptide-PEG was used to measure MMP activity. Following administration to mice via tail-vein injection, unveiled controls cleared eight-times faster than veiled particles from the blood, and fluorescence molecular tomography and MRI showed that veiled particles accumulated to a greater extent in tumor xenografts.

A different shielding strategy was developed by Olson *et al.*, who instead of using PEG chains, used MMP cleavable polyanionic peptides to electrostatically neutralize short, cell-penetrating polycationic domains on the surface of dendrimeric nanoparticles [48]. Following cleavage of the cleavable linker (PLGCAG) by MMP, the polyanionic domain departs

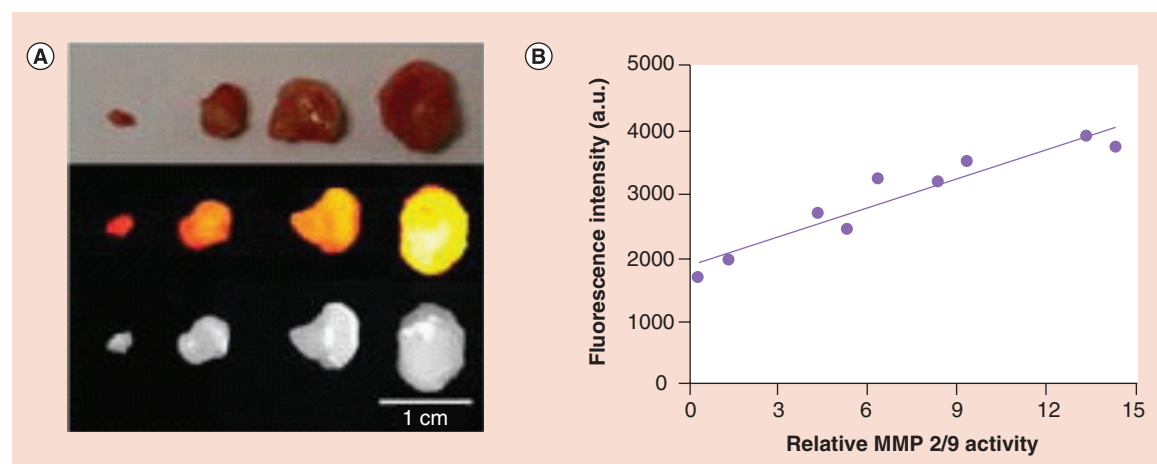


Figure 5. To distinguish different stages of tumors *in vivo*, a fluorescently quenched, peptide-based activatable nanosensor was intravenously injected into mice carrying MMP secreting SCC-7 tumors of varying sizes. (A) NIRF images of differently sized excised tumor tissues (3.5, 66.8, 172.0 and 381.5 mg), with overall signal increasing with tumor size. (B) Total fluorescent intensity (tumor grade) increased proportionally to MMP 2/9 activity, as measured by gelatin zymography.

Reproduced with permission from [21].

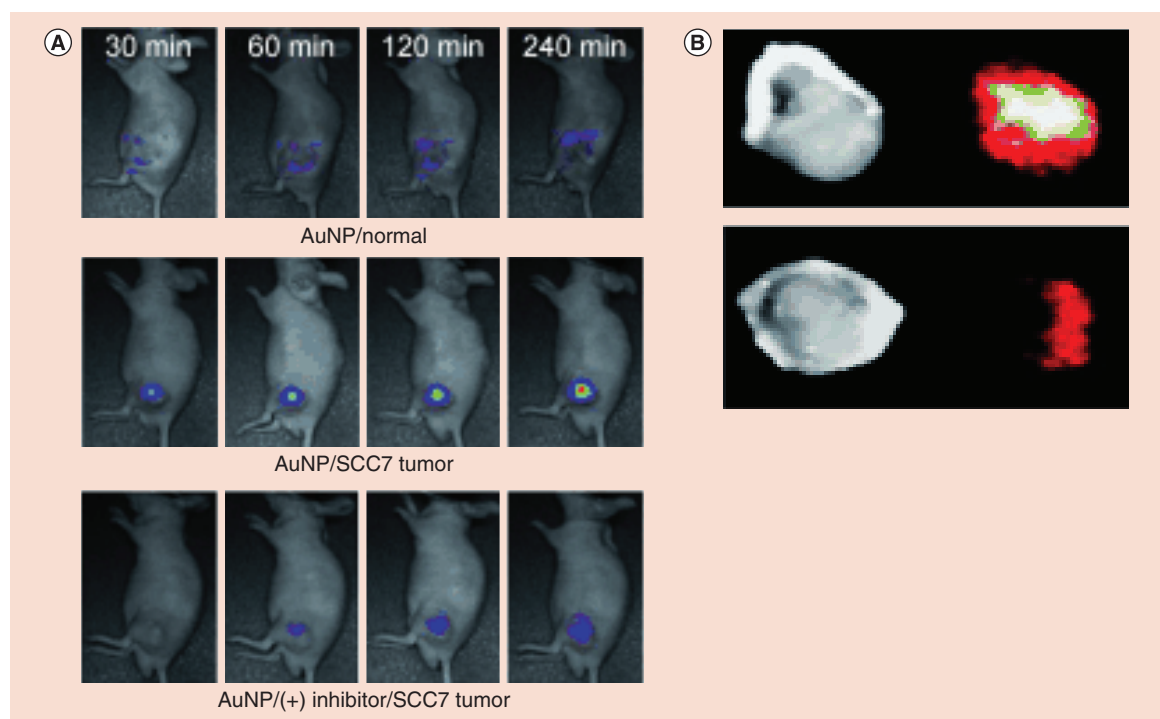


Figure 6. (A) A series of NIRF tomographic images of normal and SCC-7 tumor-bearing athymic nude mice after intratumoral injection of an MMP-sensitive gold nanoprobe (AuNP), with and without inhibitor. Clear visualization of MMP-2 activity was evident in tumor bearing mice. Signal diminished significantly in normal mice and in MMP-2 inhibitor-treated tumor-bearing mice. (B) *Ex vivo* validation: NIRF signals of excised tumors were significantly higher (upper image) compared with inhibitor-treated tumors (lower image). Reproduced with permission from [40].

from the polycation and associated nanoparticle, which are then able to penetrate cells in the immediate vicinity of the protease. Tracking of nanoparticle uptake in tumor-bearing mice by optical imaging and T_1 -weighted MRI was possible by labeling the cell-penetrating peptide with Cy5, gadolinium (Gd) or both. Residual tumor and metastasis as small as 200 μm was detected with optical imaging, while Gd-labeled nanoparticles deposited 30–50 μM of Gd in tumor parenchyma, which resulted in significant T_1 contrast that persisted for 2–3 days after injection.

PET/optical

PET provides tomographic images with excellent sensitivity and information on metabolic activities [49]. PET, unlike optical imaging, is limited in its ability to provide molecular information on proteolytic activity. As a result, combining PET imaging with optical imaging can provide vital information on tumor-targeting efficacy and proteolytic activity. Lee and co-workers prepared a PET/optical imaging probe by conjugating ^{64}Cu radiolabeled DOTA complex and activatable MMP-sensitive probe onto azide-functionalized glycol chitosan nanoparticles via copper-free click chemistry [49]. The ^{64}Cu -radiolabeled DOTA was used as

an ‘always on’ PET imaging agent, while the MMP-sensitive probe (Cy5.5-GPLGVRGK(BHQ-3)GG) was used as an ‘activatable’ optical imaging agent. The activity of MMP and the biodistribution of the probe following intravenous injection were successfully measured in tumor bearing mice by both NIRF and PET. NIRF signal could be detected in the tumor region 1 h after injection and kept increasing until it reached a maximum value after 6 h. Meanwhile, administration of an MMP inhibitor significantly reduced the NIRF signal. PET imaging enabled *in vivo* real-time visualization of tumor accumulation and biodistribution of the probe. Tumor accumulation continued to increase until it reached a plateau 24-h postinjection.

CT/optical

Combining both CT and NIRF functionalities onto the same probe enables simultaneous gathering of CT anatomical images with high spatial resolution and optical images with high sensitivity [75]. It is also a cheaper alternative to MRI fluorescence multimodal imaging [58]. Sun *et al.* developed a CT/optical imaging agent based on X-ray absorption and optical quenching properties of AuNPs [24]. To increase the physiological stability of AuNPs, they modified the

surface with biocompatible glycol chitosan (GC) polymers (GC-AuNPs). For fluorescence optical imaging of MMP activity, an MMP-specific activatable peptide probe (Cy5.5-GPLGVAGL-BHQ3) was conjugated to GC-AuNPs (MMP-GC-AuNPs), which resulted in combinatorial quenching effect of NIRF of Cy5.5 by the black hole quencher (BHQ-3) and AuNP surface. *In vivo* dual CT/optical imaging studies were performed with HT-29 tumor bearing mice to confirm the specific accumulation and MMP-responsive behavior of MMP-GC-AuNPs. CT images provided anatomical information of the tumor (Figure 8A), while the NIRF signal was detected in the tumor region 1 h after injection, and increased gradually until reaching a maximum value after 4 h. Meanwhile, administration of an MMP inhibitor intratumorally 30 min before injection significantly reduced the NIRF signal (Figure 8B).

Conclusion & future perspective

Genomics and proteomics have provided tremendous insight into the genetic, biochemical and cellular abnormalities that occur during cancer pathogenesis [4]. With this greater understanding, imaging of

in vivo proteolytic activity provides the potential for early detection and staging of cancer. It is especially advantageous due to the catalytic nature of proteases, which allows for signal amplification and for the design of activatable probes with minimal background noise and enhanced contrast. To be effective, the imaging probe must display excellent pharmacokinetic properties, minimal toxicity, specific tumor targeting capability, specificity and selectivity to a target protease, and high signal-to-noise ratio.

Nanoparticles possess unique physical and chemical properties that can be varied for optimal tumor targeting and recognition of proteolytic activity. While small molecule probes may be optimum for some applications, nanoprobe do offer some advantages over small molecule based systems. Small molecule-based probes tend to be unstable and distribute nonspecifically into tissue, yielding a high background noise. On the other hand, nanoparticles, with a high surface area to volume ratio, enable the incorporation of large peptide-dye payloads, which leads to enhanced target selectivity, increased sensitivity through signal amplification, and the potential for multimodal imaging of proteo-

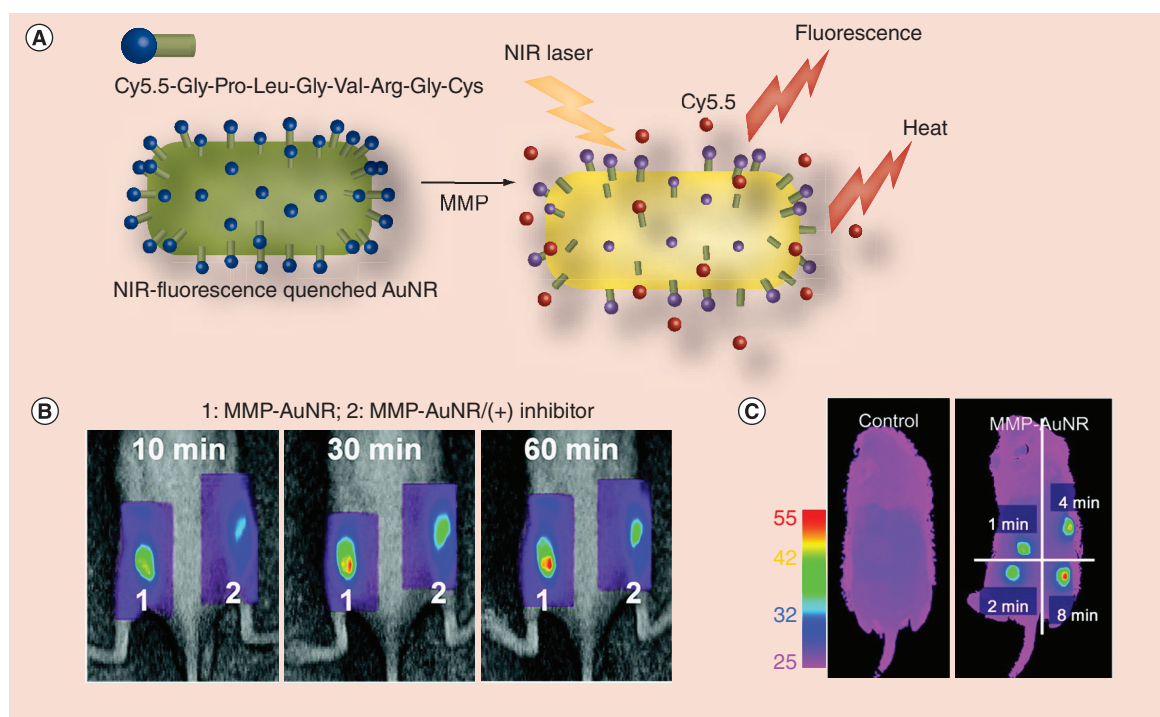


Figure 7. (A) Schematic of a theranostic probe based on MMP-sensitive gold nanorods (MMP-AuNR) for simultaneous cancer imaging and photothermal therapy. (B) NIRF tomographic images of SCC-7 tumor-bearing mice following intratumoral injection of MMP-AuNR without (1) and with (2) inhibitor were taken, showing a significantly enhanced NIRF signal in the tumor with no inhibitor added, compared with that treated with an inhibitor. (C) The hyperthermal therapeutic potential of MMP-AuNR was visualized through infrared thermal images of tumor-bearing mice and measured with a hypodermic thermocouple. Laser irradiation at various times was done after intratumoral injection of MMP-AuNR. The temperature increased up to 45° after 4 min of laser irradiation.

Reproduced with permission from [46].

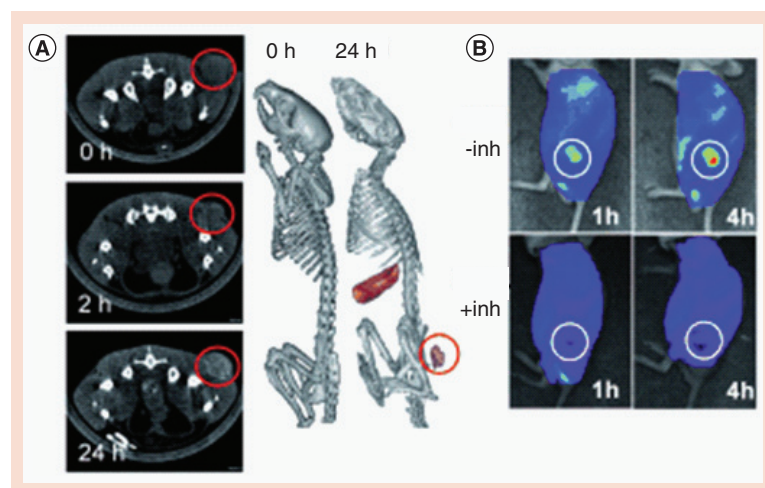


Figure 8. The potential of MMP-GC-AuNP as an *in vivo* CT/optical dual imaging agent was evaluated following intravenous injection of the probe into MMP-2 positive, HT-29 tumor-bearing mice. CT images confirmed the tumor-targeting efficacy of the probe, while the NIRF images confirmed its MMP-2-responsive.

Reproduced with permission from [24].

lytic activity, not possible with small molecule systems. Moreover, nanoparticles can also offer multifunctionality through their inherent unique optical, magnetic and therapeutic properties. However, while incorporating surface coatings, targeting ligands, imaging agents and therapeutics can yield desirable properties for diagnosis and therapy, the additional complexity could introduce challenges to large-scale production and batch-to-batch reproducibility – potentially hampering clinical translation and commercialization. This is a significant problem that hinders the production of nanoprobe, as opposed to small molecule imaging systems. Also, since even small changes in any one of the physiochemical properties (e.g., size, surface chemistry, etc.) tend to affect the pharmacokinetics, biodistribution and toxicity of nanoprobe, these systems are inherently difficult to optimize due to the large parameter space. However, given their enormous potential in both diagnosis and therapy, significant effort in their development continues.

Several biological, physical and regulatory barriers must be overcome prior to clinical translation and commercialization of nanoparticle-based proteolytic imaging probes. Unfortunately, only a small number of probes are able to provide quantitative rather than semi-quantitative information about proteolytic activity at the target site. Semi-quantitative information, where the only signal obtained is from the activated product, can be misleading since the probe does not accumulate uniformly throughout the body or even in the tumor volume [76]. Moreover, following activation by proteases, it is difficult to pinpoint the exact location of the probe. To overcome this issue, the con-

centration of both the probe and the activated product should be co-localized simultaneously and the signal ratio used to correct for lesion heterogeneity. While the dual fluorochrome probes and some of the multimodality probes discussed in this review are capable of providing quantitative information about proteolytic activity, much work remains to be done [77].

Another challenge in measurement of *in vivo* proteolytic activity is the shielding of the peptide sequence from preactivation prior to reaching the target site. This is a difficult challenge due to the variety of proteases present in serum, which can increase the background noise. Shielding of the peptide with PEG instills a stealth property that can reduce preactivation, but can also inhibit the action of the target proteases. Advancement in nanoprobe design requires fine balancing between the nanoparticle physiochemical properties and safety features with imaging sensitivity. The choice of protease is also very important. Proteases that are present in the tumor interstitium require extravasation and penetration of nanoparticles through the various barriers to reach the desired regions in the tumor interstitium, a slow and complex process that requires extended plasma half-life, which in turn could lead to high background noise. Moreover, fluorescent molecules tend to photobleach and destabilize over time. Proteases present in the angiogenic tumor vasculature may be an easier target as those probes do not require prolonged circulation or tissue penetration properties. Otherwise, further effort should be placed toward discovering more selective and sensitive shielding strategies and into the discovery of specific peptide substrates as these in large part determine the signal-to-noise ratio of the contrast agent.

There is also a limited understanding of the potential adverse effects of these nanoparticle-based systems, which could have drastically different toxicity profiles from their constituent components [58]. Many of the studies discussed in this review, for example, focus on enhanced tumor targeting without assessing the impact on other organs such as the liver. Obtaining a full toxicity profile, short-term and long-term, as well as nanoparticle biodistribution to critical organs and their clearance is essential.

Quantification of *in vivo* proteolytic activity promises to tremendously increase our knowledge of disease progression, potentially also leading to improved therapies. For this to become reality, however, the specificity, selectivity and sensitivity of probes need to be further developed, along with the computational methods necessary for data analysis. Such an effort will require a multidisciplinary effort with collaboration between engineers, chemists, biologists, physicists and clinicians.

Financial & competing interests disclosure

This material was partially supported by a Department of Defense FY2012 Prostate Cancer Research Program (PCRP) Idea Development Award (award #W81XWH-13-1-0288), funding from NIH (grant no. R01 HL114477) and by a fellowship from the Auburn University Research Initiative in Cancer (AURIC).

The authors have no other relevant affiliations or financial involvement with any organization or entity with a financial interest in or financial conflict with the subject matter or materials discussed in the manuscript apart from those disclosed.

No writing assistance was utilized in the production of this manuscript.

Executive summary**Molecular imaging of proteolytic activity in tumor models *in vivo***

- Identifying and quantifying molecular-level changes associated with tumorigenesis helps in early detection and estimation of malignant potential; necessary for effective cancer treatment.
- Several proteases, including matrix metalloproteinases, cathepsins and caspases, have been implicated in tumor invasiveness and metastasis and their expression is an indicator of tumor aggressiveness.
- Proteases can propagate signals through their catalytic activity; specifically cleave certain peptide sequences; and are present at the invasive front of tumors, regions that are more easily accessed by probes.
- Imaging probes have been developed with nanoparticle technology to provide a noninvasive measurement of proteolytic activity in tumor models at different stages of disease progression. Nanoparticles have unique physical and chemical properties; excellent *in vivo* characteristics; and a vast surface area to deliver a large number of imaging agents and tumor-targeting ligands.

Nanoparticles for MRI of proteolytic activity *in vivo*

- Magnetic nanoparticles used to image proteolytic activity rely on signal amplification due to cluster formation following proteolytic cleavage, which enhances magnetic susceptibility and r_2 relaxivity.
- The most commonly used design strategy utilizes two sets of complimentary, polyethylene glycol (PEG)-conjugated iron oxide nanoparticles that self-assemble (e.g., through neutravidin/biotin interactions) following proteolytic cleavage and release of PEG.
- A significant drawback of utilizing separate sets of nanoparticles is they face co-delivery issues *in vivo*.

Nanoparticles for optical imaging of proteolytic activity *in vivo*

- Optical imaging remains the most commonly used modality for imaging proteolytic activity *in vivo*. The majority of probes utilize one or more fluorescence quenching effects to reduce the preactivation fluorescence signal. Fluorescence is recovered following release of quencher by proteolytic activity.
- Several theranostic probes have been developed for simultaneous therapy and imaging of proteolytic activity.
- Other examples of optical imaging include bioluminescence resonance energy transfer, photoacoustic imaging and secondary Cerenkov-induced fluorescent imaging.

Nanoparticles for multimodal imaging of proteolytic activity *in vivo*

- Multimodality combines several complimentary imaging modalities, each with its own strengths and weaknesses, into a single platform, thus overcoming their individual limitations.
- MRI/optical dual imaging has been the most thoroughly investigated combination
- PET/optical and CT/optical dual probes have been developed as well.

References

Papers of special note have been highlighted as: • of interest; •• of considerable interest

- Bray F, Jemal A, Grey N, Ferlay J, Forman D. Global cancer transitions according to the Human Development Index (2008–2030): a population-based study. *Lancet Oncol.* 13(8), 790–801 (2012).
- Yang Y, Hong H, Zhang Y, Cai W. Molecular imaging of proteases in cancer. *Cancer Growth Metastasis* 2, 13–27 (2009).
- Luo S, Zhang E, Su Y, Cheng T, Shi C. A review of NIR dyes in cancer targeting and imaging. *Biomaterials* 32(29), 7127–7138 (2011).
- Seaman ME, Contino G, Bardeesy N, Kelly KA. Molecular imaging agents: impact on diagnosis and therapeutics in oncology. *Expert Rev. Mol. Med.* 12, e20 (2010).
- Sivasubramanian M, Hsia Y, Lo LW. Nanoparticle-facilitated functional and molecular imaging for the early detection of cancer. *Front. Mol. Biosci.* 1, 15 (2014).
- Mankoff DA. A definition of molecular imaging. *J. Nucl. Med.* 48(6), 18n, 21n (2007).
- Pysz MA, Gambhir SS, Willmann JK. Molecular imaging: current status and emerging strategies. *Clin. Radiol.* 65(7), 500–516 (2010).
- Albanese A, Tang PS, Chan WC. The effect of nanoparticle size, shape, and surface chemistry on biological systems. *Annu. Rev. Biomed. Eng.* 14, 1–16 (2012).
- Wong C, Stylianopoulos T, Cui J *et al.* Multistage nanoparticle delivery system for deep penetration into tumor tissue. *Proc. Natl Acad. Sci. USA* 108(6), 2426–2431 (2011).
- Yoon SM, Myung SJ, Kim IW *et al.* Application of near-infrared fluorescence imaging using a polymeric nanoparticle-based probe for the diagnosis and therapeutic monitoring of colon cancer. *Dig. Dis. Sci.* 56(10), 3005–3013 (2011).

- 11 Chien M-P, Thompson MP, Barback CV, Ku T-H, Hall DJ, Gianneschi NC. Enzyme-directed assembly of a nanoparticle probe in tumor tissue. *Adv. Mater.* 25(26), 3599–3604 (2013).
- 12 Harris TJ, Von Maltzahn G, Lord ME *et al.* Protease-triggered unveiling of bioactive nanoparticles. *Small* 4(9), 1307–1312 (2008).
- 13 Steeg PS. Tumor metastasis: mechanistic insights and clinical challenges. *Nat. Med.* 12(8), 895–904 (2006).
- 14 Lin X, Xie J, Zhu L *et al.* Hybrid ferritin nanoparticles as activatable probes for tumor imaging. *Angew. Chem. Int. Ed. Engl.* 50(7), 1569–1572 (2011).
- 15 Lee CM, Jang D, Cheong SJ *et al.* Optical imaging of MMP expression and cancer progression in an inflammation-induced colon cancer model. *Int. J. Cancer* 131(8), 1846–1853 (2012).
- 16 Yhee JY, Kim SA, Koo H *et al.* Optical imaging of cancer-related proteases using near-infrared fluorescence matrix metalloproteinase-sensitive and cathepsin B-sensitive probes. *Theranostics* 2(2), 179–189 (2012).
- 17 Lee S, Park K, Lee SY *et al.* Dark quenched matrix metalloproteinase fluorogenic probe for imaging osteoarthritis development *in vivo*. *Bioconjug. Chem.* 19(9), 1743–1747 (2008).
- 18 Jiang T, Olson ES, Nguyen QT, Roy M, Jennings PA, Tsien RY. Tumor imaging by means of proteolytic activation of cell-penetrating peptides. *Proc. Natl Acad. Sci. USA* 101(51), 17867–17872 (2004).
- 19 Bremer C, Tung CH, Weissleder R. *In vivo* molecular target assessment of matrix metalloproteinase inhibition. *Nat. Med.* 7(6), 743–748 (2001).
- 20 McIntyre JO, Fingleton B, Wells KS *et al.* Development of a novel fluorogenic proteolytic beacon for *in vivo* detection and imaging of tumour-associated matrix metalloproteinase-7 activity. *Biochem. J.* 377(Pt 3), 617–628 (2004).
- 21 Lee S, Ryu JH, Park K *et al.* Polymeric nanoparticle-based activatable near-infrared nanosensor for protease determination *in vivo*. *Nano Lett.* 9(12), 4412–4416 (2009).
- 22 Scherer RL, Vansaun MN, McIntyre JO, Matrisian LM. Optical imaging of matrix metalloproteinase-7 activity *in vivo* using a proteolytic nanobeacon. *Mol. Imaging* 7(3), 118–131 (2008).
- **A dual fluorochrome probe, with a signal and a reference fluorophore, was developed for quantitative imaging of MMP-7 activity with the ability to correct for variations of excitation light and depth of tumor lesion.**
- 23 Thorek DL, Ogirala A, Beattie BJ, Grimm J. Quantitative imaging of disease signatures through radioactive decay signal conversion. *Nat. Med.* 19(10), 1345–1350 (2013).
- 24 Sun IC, Eun DK, Koo H *et al.* Tumor-targeting gold particles for dual computed tomography/optical cancer imaging. *Angew. Chem. Int. Ed. Engl.* 50(40), 9348–9351 (2011).
- **Tumor-targeted gold nanoparticles were utilized for anatomical imaging with CT x-ray absorption and simultaneous visualization of MMP activity with optical imaging.**
- 25 Gallo J, Kamaly N, Lavdas I *et al.* CXCR4-targeted and MMP-responsive iron oxide nanoparticles for enhanced magnetic resonance imaging. *Angew. Chem. Int. Ed. Engl.* 53(36), 9550–9554 (2014).
- **Demonstrate enhanced T2 relaxivity due to the response of complimentary SPIONs to MMP 2/9 activity in tumor-bearing mice.**
- 26 Egusquiguirre SP, Beziere N, Pedraz JL, Hernandez RM, Ntziachristos V, Igartua M. Optoacoustic imaging enabled biodistribution study of cationic polymeric biodegradable nanoparticles. *Contrast Media Mol. Imaging* 10(6), 421–427 (2015).
- 27 McCarthy JR, Weissleder R. Multifunctional magnetic nanoparticles for targeted imaging and therapy. *Adv. Drug Deliv. Rev.* 60(11), 1241–1251 (2008).
- 28 Welch MJ, Hawker CJ, Wooley KL. The advantages of nanoparticles for PET. *J. Nucl. Med.* 50(11), 1743–1746 (2009).
- 29 Cole AJ, Yang VC, David AE. Cancer theranostics: the rise of targeted magnetic nanoparticles. *Trends Biotechnol.* 29(7), 323–332 (2011).
- 30 Shin SJ, Beech JR, Kelly KA. Targeted nanoparticles in imaging: paving the way for personalized medicine in the battle against cancer. *Integr. Biol. (Camb.)* 5(1), 29–42 (2013).
- 31 Von Maltzahn G, Harris TJ, Park JH *et al.* Nanoparticle self-assembly gated by logical proteolytic triggers. *J. Am. Chem. Soc.* 129(19), 6064–6065 (2007).
- 32 Schellenberger E, Rudloff F, Warmuth C, Taupitz M, Hamm B, Schnorr J. Protease-specific nanosensors for magnetic resonance imaging. *Bioconjug. Chem.* 19(12), 2440–2445 (2008).
- 33 Yan L, Gao Y, Pierce R, Dai L, Kim J, Zhang M. Development of Y-shaped peptide for constructing nanoparticle systems targeting tumor-associated macrophages *in vitro* and *in vivo*. *Mater. Res. Express* 1(2), 025007 (2014).
- 34 Ansari C, Tikhomirov GA, Hong SH *et al.* Development of novel tumor-targeted theranostic nanoparticles activated by membrane-type matrix metalloproteinases for combined cancer magnetic resonance imaging and therapy. *Small* 10(3), 566–575, 417 (2014).
- 35 Yuan Y, Ge S, Sun H *et al.* Intracellular self-assembly and disassembly of 19F nanoparticles confer respective “off” and “on” 19F NMR/MRI signals for legumain activity detection in zebrafish. *ACS Nano* 9(5), 5117–5124 (2015).
- 36 Ryu JH, Na JH, Ko HK *et al.* Noninvasive optical imaging of cathepsin B with activatable fluorogenic nanoprobe in various metastatic models. *Biomaterials* 35(7), 2302–2311 (2014).
- **Cathepsin B responsive nanoprobe were utilized to discriminate between liver, lung and peritoneal metastatic tumors in a rodent model.**
- 37 Park K, Jeong J, Chung BH. Cascade imaging of proteolytic pathways in cancer cells using fluorescent protein-conjugated gold nanoquenchers. *Chem. Commun. (Camb.)* 48(85), 10547–10549 (2012).

- **Simultaneous imaging of multiple caspases involved in cancer cell apoptosis was demonstrated with a fluorescent protein-conjugated gold nanoprobe.**
- 38 Deng D, Zhang D, Li Y, Achilefu S, Gu Y. Gold nanoparticles based molecular beacons for *in vitro* and *in vivo* detection of the matriptase expression on tumor. *Biosens. Bioelectron.* 49, 216–221 (2013).
- 39 Xie J, Zhang F, Aronova M *et al.* Manipulating the power of an additional phase: a flower-like Au-Fe₃O₄ optical nanosensor for imaging protease expressions *in vivo*. *ACS Nano* 5(4), 3043–3051 (2011).
- **A flower-like Au-Fe₃O₄ nanocomposite was utilized to detect MMP activity in tumors with increasing signal up to 4h.**
- 40 Lee S, Cha EJ, Park K *et al.* A near-infrared-fluorescence-quenched gold-nanoparticle imaging probe for *in vivo* drug screening and protease activity determination. *Angew. Chem. Int. Ed. Engl.* 47(15), 2804–2807 (2008).
- 41 Mu CJ, Lavan DA, Langer RS, Zetter BR. Self-assembled gold nanoparticle molecular probes for detecting proteolytic activity *in vivo*. *ACS Nano* 4(3), 1511–1520 (2010).
- 42 Cordovilla C, Swager TM. Strain release in organic photonic nanoparticles for protease sensing. *J. Am. Chem. Soc.* 134(16), 6932–6935 (2012).
- 43 Kim YP, Daniel WL, Xia Z, Xie H, Mirkin CA, Rao J. Bioluminescent nanosensors for protease detection based upon gold nanoparticle-luciferase conjugates. *Chem. Commun. (Camb.)* 46(1), 76–78 (2010).
- 44 Zeng T, Zhang T, Wei W *et al.* Compact, programmable, and stable biofunctionalized upconversion nanoparticles prepared through peptide-mediated phase transfer for high-sensitive protease sensing and *in vivo* apoptosis imaging. *ACS Appl Mater Interfaces* 7(22), 11849–11856 (2015).
- 45 Chen WH, Xu XD, Jia HZ *et al.* Therapeutic nanomedicine based on dual-intelligent functionalized gold nanoparticles for cancer imaging and therapy *in vivo*. *Biomaterials* 34(34), 8798–8807 (2013).
- 46 Yi DK, Sun IC, Ryu JH *et al.* Matrix metalloproteinase sensitive gold nanorod for simultaneous bioimaging and photothermal therapy of cancer. *Bioconjug. Chem.* 21(12), 2173–2177 (2010).
- **Describe the utilization of gold nanorods for simultaneous imaging of MMP activity and photothermal therapy.**
- 47 Yang K, Zhu L, Nie L *et al.* Visualization of protease activity *in vivo* using an activatable photo-acoustic imaging probe based on CuS nanoparticles. *Theranostics* 4(2), 134–141 (2014).
- 48 Olson ES, Jiang T, Aguilera TA *et al.* Activatable cell penetrating peptides linked to nanoparticles as dual probes for *in vivo* fluorescence and MR imaging of proteases. *Proc Natl Acad Sci USA* 107(9), 4311–4316 (2010).
- 49 Lee S, Kang SW, Ryu JH *et al.* Tumor-homing glycol chitosan-based optical/PET dual imaging nanoprobe for cancer diagnosis. *Bioconjug. Chem.* 25(3), 601–610 (2014).
- **A dual PET/NIRF imaging probe based on ⁶⁴Cu-radiolabeled chitosan nanoparticles was utilized for real-time visualization of tumor accumulation and for sensing of MMP activity.**
- 50 Veisheh O, Gunn JW, Zhang M. Design and fabrication of magnetic nanoparticles for targeted drug delivery and imaging. *Adv. Drug Deliv. Rev.* 62(3), 284–304 (2010).
- 51 Felton C, Karmakar A, Gartia Y, Ramidi P, Biris AS, Ghosh A. Magnetic nanoparticles as contrast agents in biomedical imaging: recent advances in iron- and manganese-based magnetic nanoparticles. *Drug Metab. Rev.* 46(2), 142–154 (2014).
- 52 Chertok B, Moffat BA, David AE *et al.* Iron oxide nanoparticles as a drug delivery vehicle for MRI monitored magnetic targeting of brain tumors. *Biomaterials* 29(4), 487–496 (2008).
- 53 Cha EJ, Jang ES, Sun IC *et al.* Development of MRI/NIRF ‘activatable’ multimodal imaging probe based on iron oxide nanoparticles. *J. Control. Release* 155(2), 152–158 (2011).
- 54 Lin S, Deng F, Huang P *et al.* A novel legumain protease-activated micelle cargo enhances anticancer activity and cellular internalization of doxorubicin. *J. Mater. Chem. B* 3(29), 6001–6012 (2015).
- 55 Liu C, Sun C, Huang H, Janda K, Edgington T. Overexpression of legumain in tumors is significant for invasion/metastasis and a candidate enzymatic target for prodrug therapy. *Cancer Res.* 63(11), 2957–2964 (2003).
- 56 Siveen KS, Kuttan G. Role of macrophages in tumour progression. *Immunol. Lett.* 123(2), 97–102 (2009).
- 57 Luo Y, Zhou H, Krueger J *et al.* Targeting tumor-associated macrophages as a novel strategy against breast cancer. *J. Clin. Invest.* 116(8), 2132–2141 (2006).
- 58 Hilderbrand SA, Weissleder R. Near-infrared fluorescence: application to *in vivo* molecular imaging. *Curr. Opin. Chem. Biol.* 14(1), 71–79 (2010).
- 59 Kim J, Piao Y, Hyeon T. Multifunctional nanostructured materials for multimodal imaging, and simultaneous imaging and therapy. *Chem. Soc. Rev.* 38 372–390 (2009).
- 60 Frangioni JV. New technologies for human cancer imaging. *J. Clin. Oncol.* 26(24), 4012–4021 (2008).
- 61 Sinha C, Arora K, Moon CS, Yarlagaadda S, Woodrooffe K, Naren AP. Forster resonance energy transfer – an approach to visualize the spatiotemporal regulation of macromolecular complex formation and compartmentalized cell signaling. *Biochim. Biophys. Acta* 1840(10), 3067–3072 (2014).
- 62 Mohamed MM, Sloane BF. Cysteine cathepsins: multifunctional enzymes in cancer. *Nat. Rev. Cancer* 6(10), 764–775 (2006).
- 63 Swierczewska M, Lee S, Chen X. The design and application of fluorophore-gold nanoparticle activatable probes. *Phys. Chem. Chem. Phys.* 13(21), 9929–9941 (2011).
- 64 Chen G, Qiu H, Prasad PN, Chen X. Upconversion nanoparticles: design, nanochemistry, and applications in theranostics. *Chem. Rev.* 114(10), 5161–5214 (2014).
- 65 Cheng Z, Al Zaki A, Hui JZ, Muzykantov VR, Tsourkas A. Multifunctional nanoparticles: cost versus benefit of adding targeting and imaging capabilities. *Science* 338(6109), 903–910 (2012).
- 66 Wang F, Wang YC, Dou S, Xiong MH, Sun TM, Wang J. Doxorubicin-tethered responsive gold nanoparticles facilitate

- intracellular drug delivery for overcoming multidrug resistance in cancer cells. *ACS Nano* 5(5), 3679–3692 (2011).
- 67 Calderon M, Welker P, Licha K *et al.* Development of efficient acid cleavable multifunctional prodrugs derived from dendritic polyglycerol with a poly(ethylene glycol) shell. *J. Control. Release* 151(3), 295–301 (2011).
 - 68 Tauro M, McGuire J, Lynch CC. New approaches to selectively target cancer-associated matrix metalloproteinase activity. *Cancer Metastasis Rev.* 33(4), 1043–1057 (2014).
 - 69 Xia K, Zhang L, Huang Y, Lu Z. Preparation of gold nanorods and their applications in photothermal therapy. *J. Nanosci. Nanotechnol.* 15(1), 63–73 (2015).
 - 70 Luke GP, Yeager D, Emelianov SY. Biomedical applications of photoacoustic imaging with exogenous contrast agents. *Ann. Biomed. Eng.* 40(2), 422–437 (2012).
 - 71 Wu D, Huang L, Jiang MS, Jiang H. Contrast agents for photoacoustic and thermoacoustic imaging: a review. *Int. J. Mol. Sci.* 15(12), 23616–23639 (2014).
 - 72 Kircher MF, Weissleder R, Josephson L. A dual fluorochrome probe for imaging proteases. *Bioconjug. Chem.* 15(2), 242–248 (2004).
 - 73 Xu JH, Gao FP, Liu XF *et al.* Supramolecular gelatin nanoparticles as matrix metalloproteinase responsive cancer cell imaging probes. *Chem. Commun. (Camb.)* 49(40), 4462–4464 (2013).
 - 74 Haris M, Singh A, Mohammed I *et al.* *In vivo* magnetic resonance imaging of tumor protease activity. *Sci. Rep.* 4, 6081 (2014).
 - 75 Lee DE, Koo H, Sun IC, Ryu JH, Kim K, Kwon IC. Multifunctional nanoparticles for multimodal imaging and theragnosis. *Chem. Soc. Rev.* 41(7), 2656–2672 (2012).
 - 76 Razgulin A, Ma N, Rao J. Strategies for *in vivo* imaging of enzyme activity: an overview and recent advances. *Chem. Soc. Rev.* 40(7), 4186–4216 (2011).
 - 77 Li C. A multifunctional targeted approach. *Nat. Mater.* 13(2), 110–115 (2014).



Article

Effects of Iron-Oxide Nanoparticle Surface Chemistry on Uptake Kinetics and Cytotoxicity in CHO-K1 Cells

Camille C. Hanot, Young Suk Choi, Tareq B. Anani, Dharsan Soundarrajan and Allan E. David *

Received: 24 November 2015; Accepted: 23 December 2015; Published: 31 December 2015

Academic Editors: Yuping Bao and Anna Cristina S. Samia

Department of Chemical Engineering, Auburn University, Auburn, AL 36849, USA;
thamarrys@hotmail.com (C.C.H.); yzc0036@auburn.edu (Y.S.C.); tba0008@tigermail.auburn.edu (T.B.A.);
dks0009@tigermail.auburn.edu (D.S.)

* Correspondence: aedavid@auburn.edu; Tel.: +1-334-844-8119

Abstract: Superparamagnetic iron-oxide nanoparticles (SPIONs) show great promise for multiple applications in biomedicine. While a number of studies have examined their safety profile, the toxicity of these particles on reproductive organs remains uncertain. The goal of this study was to evaluate the cytotoxicity of starch-coated, aminated, and PEGylated SPIONs on a cell line derived from Chinese Hamster ovaries (CHO-K1 cells). We evaluated the effect of particle diameter (50 and 100 nm) and polyethylene glycol (PEG) chain length (2k, 5k and 20k Da) on the cytotoxicity of SPIONs by investigating cell viability using the tetrazolium dye 3-(4,5-dimethylthiazol-2-yl)-2,5-diphenyltetrazolium bromide (MTT) and sulforhodamine B (SRB) assays. The kinetics and extent of SPION uptake by CHO-K1 cells was also studied, as well as the resulting generation of intracellular reactive oxygen species (ROS). Cell toxicity profiles of SPIONs correlated strongly with their cellular uptake kinetics, which was strongly dependent on surface properties of the particles. PEGylation caused a decrease in both uptake and cytotoxicity compared to aminated SPIONs. Interestingly, 2k Da PEG-modified SPIONs displayed the lowest cellular uptake and cytotoxicity among all studied particles. These results emphasize the importance of surface coatings when engineering nanoparticles for biomedical applications.

Keywords: superparamagnetic iron-oxide nanoparticles (SPIONs); PEGylated nanoparticles; aminated nanoparticles; reproductive toxicity; nanotoxicity; uptake kinetics; ROS generation

1. Introduction

Iron-oxide nanoparticles, and in particular superparamagnetic iron-oxide nanoparticles (SPIONs), have gained a fair amount of attention in recent years, accounting for more than 5900 publications over the last five years (PubMed database, quick search in December 2015 with the following keywords: “iron-oxide nanoparticle”). Their magnetic properties, combined with the possibilities afforded by optimization of their surface chemistry, promise potential applications in many fields, including nanomedicine [1–4]. Iron-oxide nanoparticle formulations have already been approved by the U.S. Food and Drug Administration and the European Commission as contrast agents for magnetic resonance imaging (MRI) [5]. Additional applications being pursued include MRI-based cell tracking of SPION-loaded cells, magnetic field-directed stem cells for regenerative therapies, therapeutic magnetofection-based delivery of drugs or genes, and anti-tumor treatment with magnetic hyperthermia [2,5]. However, safety concerns and manufacturing challenges remain as significant hurdles to their development and clinical translation [5,6].

Although the overall safety of iron-oxide nanoparticles is generally accepted [7], the core and surface properties have the potential to trigger cytotoxicity once in contact with cells. Indeed, side-effects were reported in up to 23% of patients receiving Ferumoxtran-10, a dextran-coated SPION,

as MRI contrast agent [8]. Although about 86% of cases were mild-to-moderate, some adverse reactions, such as anaphylactic shock, were life-threatening [9]. While the awareness of nanoparticle-induced toxicity is growing, toxicity studies represent only 11% of aforementioned publications on SPIONs over the last five years (PubMed, keywords' iron-oxide nanoparticle toxicity' in December 2015), and most of these studies were conducted with cancer cell lines. A thorough understanding of the physicochemical parameters underlying toxicity of SPIONs on normal systems is also essential, especially since repetitive administrations may be part of a diagnostic and/or treatment regimen.

Systematic studies are rare and the impact of SPIONs on the reproductive system in particular is poorly described. The number of results for the same quick search on PubMed with the following keywords: "iron-oxide nanoparticle toxicity reproductive" drops drastically to just 10 results. Moreover, toxicology data about the reproductive toxicity of SPIONs were mainly generated with *in vivo* studies using only dextran-coated SPIONs. Nevertheless, no effect on the fertility and reproductive performances of rats were observed with doses up to 17.9 mg Fe/kg/day of Ferumoxtran-10 (seven times the intended human clinical dose per administration) [10], but fetal skeletal and soft-tissue abnormalities were observed in rats and rabbits, and maternotoxicity in rabbits at doses above 15 mg Fe/kg/day [10]. In addition, bare ferric oxide nanoparticles, at concentrations above 10 mg Fe/L, have been shown to induce toxic effects on the early development of zebra fishes, causing hatchling delays, malformations, and mortality [11]. Mechanisms underlying these reproductive toxicities are poorly described, as is the actual distribution of SPIONs to reproductive organs.

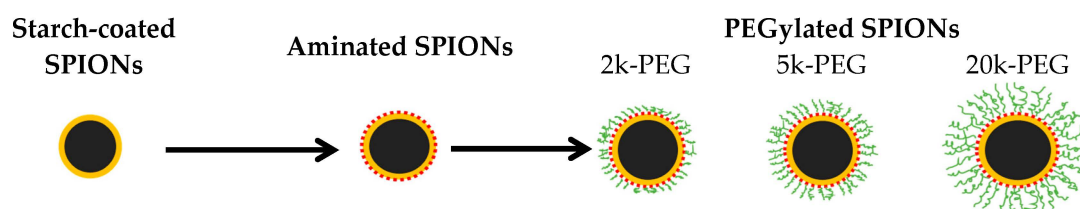
Surface modification of SPIONs can influence the interactions between nanoparticles and cells [12–15]. Using bare SPIONs and SPIONs coated with $-\text{COOH}$ or $-\text{NH}_2$, it was demonstrated that nanoparticle surface properties induce different responses between various cell types, such as cell lines derived from the heart, brain, and kidneys [16]. Introduction of poly(ethylene glycol) (PEG) moieties onto the surface of SPIONs through covalent binding is commonly used to improve biocompatibility and reduce immunogenicity [5]. PEG molecules provide stability between the particles via steric repulsion [17] and seem to decrease adsorption of plasma proteins [18]. *In vivo*, PEGylated SPIONs generally have a longer plasma circulation half-life [19,20]. Nevertheless, conflicting results exist about the cytotoxicity of PEGylated particles. In a recent study, 2k Da-PEG SPIONs were shown to be more toxic than bare dextran SPIONs [19]; they were also taken up by cells to a greater extent compared to dextran-coated SPIONs. In another study, the viability of bovine vascular smooth muscle cells was improved when incubated for 24 h with 2k Da-PEG SPIONs, when compared with bare citric acid-coated SPIONs and SPIONs coated with 10k Da-PEG [21]. The toxicity of particles in these studies appeared to correlate well with their extent of cellular uptake [19,21] and the uptake process was highly dependent upon physicochemical properties of the core and coating [22,23].

The objective of this study was to assess the *in vitro* toxicity of SPIONs, with varying surface properties, on a cell line derived from a reproductive organ: Chinese Hamster Ovary (CHO-K1) cells. SPIONs evaluated in this study included particles with mean hydrodynamic diameters of approximately 50 and 100 nm (nominal size), with surface coatings that included starch, aminated-starch, and PEG. To further evaluate the impact of PEG molecules, three molecular weights of PEG (*i.e.*, 2k, 5k, and 20k Daltons; hereafter simply specified as 2k-PEG, 5k-PEG, and 20k-PEG, respectively) were used in this study. Cytotoxicity was determined *in vitro* with the tetrazolium dye 3-(4,5-dimethylthiazol-2-yl)-2,5-diphenyltetrazolium bromide (MTT) and the sulforhodamine B (SRB) assays. The cytotoxicity was then correlated with the overall cellular uptake kinetics and the generation of ROS.

2. Results and Discussion

2.1. Physicochemical Properties of Superparamagnetic Iron-Oxide Nanoparticles (SPIONs) Are Modified through Surface Functionalization

In the present study, the starch coating of 50 and 100 nm SPIONs was crosslinked and coated with amine groups, and then functionalized with NHS-polyethylene glycol (PEG) of varying molecular weight (*i.e.*, 2k, 5k, or 20k Da) as shown in Scheme 1.



Scheme 1. Surface modification of starch-coated superparamagnetic iron-oxide nanoparticles (SPIONs) into aminated and PEGylated SPIONs.

PEG coatings are often utilized on nanoparticles for their good biocompatibility and favorable chemical properties that enable further modifications [24]. Since the coating itself may completely change the toxicity profile of SPIONs, SPIONs with a variety of surface coatings were tested, including starch-coated SPIONs, aminated SPIONs, and finally PEGylated SPIONs. Analysis of SPIONs by transmission electron microscopy (TEM) and Fourier transform infrared spectroscopy (FTIR), and measurement of their magnetic properties provided results similar to that already in the literature [20], confirming successful modification, and are not repeated here. Some physicochemical characteristics of the 10 different SPIONs tested, however, are summarized in Tables 1 and 2.

Table 1. Mean hydrodynamic diameter (HD) and ζ -potential (ZP) of superparamagnetic iron-oxide nanoparticles (SPIONs) in deionized water and in Ham's F-12K culture media supplemented with 10% FBS.

Sample	In Deionized Water, at 37 °C			In Supplemented Ham's F-12K Cultre Media, at 37 °C					
	HD (nm)	PdI	ZP (mV)	1 h		24 h		72 h	
				HD (nm)	PdI	HD (nm)	PdI	HD (nm)	PdI
50 nm SPIONs									
Starch-coated	47 ± 1	0.12	−23 ± 3	36 ± 1	0.25	68 ± 2	0.28	148 ± 4	0.30
Aminated	90 ± 2	0.18	+13 ± 1	57 ± 1	0.32	55 ± 5	0.38	50 ± 3	0.38
2k-PEG	72 ± 3	0.20	+36 ± 1	41 ± 1	0.30	40 ± 1	0.30	40 ± 1	0.31
5k-PEG	71 ± 1	0.20	+34 ± 1	37 ± 2	0.42	36 ± 2	0.41	36 ± 2	0.44
20k-PEG	72 ± 4	0.20	+33 ± 2	35 ± 1	0.48	36 ± 1	0.47	33 ± 2	0.47
100 nm SPIONs									
Starch-coated	92 ± 1	0.09	−4 ± 1	117 ± 1	0.29	461 ± 4	0.70	1133 ± 30	0.19
Aminated	127 ± 5	0.17	+43 ± 1	119 ± 4	0.30	110 ± 3	0.22	108 ± 3	0.22
2k-PEG	117 ± 2	0.14	+36 ± 1	93 ± 1	0.24	95 ± 3	0.23	95 ± 2	0.24
5k-PEG	126 ± 4	0.14	+37 ± 1	103 ± 2	0.25	102 ± 2	0.24	114 ± 2	0.29
20k-PEG	154 ± 5	0.12	+32 ± 1	122 ± 3	0.26	117 ± 3	0.26	146 ± 2	0.36

HD: hydrodynamic diameter (nm); ZP: ζ potential (mV); PdI: Polydispersity index; FBS: Fetal Bovine Serum; Results shown as mean ± std. error of mean.

The hydrodynamic diameters of both starch SPIONs were in close agreement with specifications provided by the manufacturer. After crosslinking of the starch coating and its amination, the mean hydrodynamic diameter of both 50 and 100 nm SPIONs increased significantly, possibly due to aggregation and/or due to loss of smaller particles during the processing. PEGylation further increased the hydrodynamic diameter as expected, but the effect of PEG molecular weight (2k, 5k, or 20k Da)

varied between the 50 and 100 nm SPIONs. The effect on 50 nm particles was especially non-uniform as the aminated particles yielded the largest size, possibly due to aggregation. The hydrodynamic diameters of SPIONs were also evaluated when suspended in supplemented Ham's F-12K culture media at 37 °C, the conditions employed for *in vitro* studies, with incubation times of 1, 24, and 72 h. The hydrodynamic diameters of starch-coated 50 and 100 nm SPIONs were observed to increase with time, whereas the size of aminated, 2k-PEG and 5k-PEG SPIONs, and 50 nm 20k-PEG SPIONs remained relatively constant over time. A moderate increase of the hydrodynamic diameter was noticed for 100 nm 20k-PEG SPIONs.

The surface charge of SPIONs gives an indication of their colloidal stability and may also further affect their cellular uptake. In one study, it was demonstrated that anionic nanoparticles, showing a high affinity for cell membranes, were captured more efficiently by cells than bare (dextran-coated) iron-oxide nanoparticles [25]. In deionized (DI) water, starch-coated SPIONs displayed a negative to near neutral ζ potential while the aminated and PEGylated particles showed a high positive surface charge. Surprisingly, a higher ζ potential was observed for the PEGylated 50 nm SPIONs compared to the aminated 50 nm SPIONs. The PEG layer would be expected to mask some of the surface charge and it is unclear why this was not observed, although measurements were repeated. Aggregation seen with the aminated SPIONs may have had some contribution to this result.

Interestingly, the aminated SPIONs and PEGylated SPIONs had a similar amine content that was significantly greater than that of starch SPIONs, as shown in Table 2. Conversely, some variation was observed in the PEG content, with a general trend of decreasing PEG concentration as the PEG molecular weight was increased, probably due to increasing steric hindrance with the larger molecules. This tendency, however, was less obvious with 100 nm SPIONs and the 2k and 5k Da PEGs.

Table 2. Amine- and PEG-content of SPIONs.

50 nm SPIONs			100 nm SPIONs		
Sample	Amine Content (mmol NH ₂ /mg Fe)	PEG Content (nmol PEG/mg Fe)	Sample	Amine Content (mmol NH ₂ /mg Fe)	PEG Content (nmol PEG/mg Fe)
Starch	0.14 ± 0.01	-	Starch	0.24 ± 0.01	-
Aminated	4.93 ± 0.01	-	Aminated	1.74 ± 0.01	-
2k-PEG	4.71 ± 0.01	244.5 ± 7.5	2k-PEG	1.56 ± 0.01	56.0 ± 0.5
5k-PEG	5.08 ± 0.01	5.4 ± 0.2	5k-PEG	2.26 ± 0.01	23.4 ± 0.2
20k-PEG	3.13 ± 0.01	0.2 ± 0.1	20k-PEG	1.76 ± 0.01	0.7 ± 0.1

2.2. Varying the Surface Coating of SPIONs Changes Its Toxicity Profile

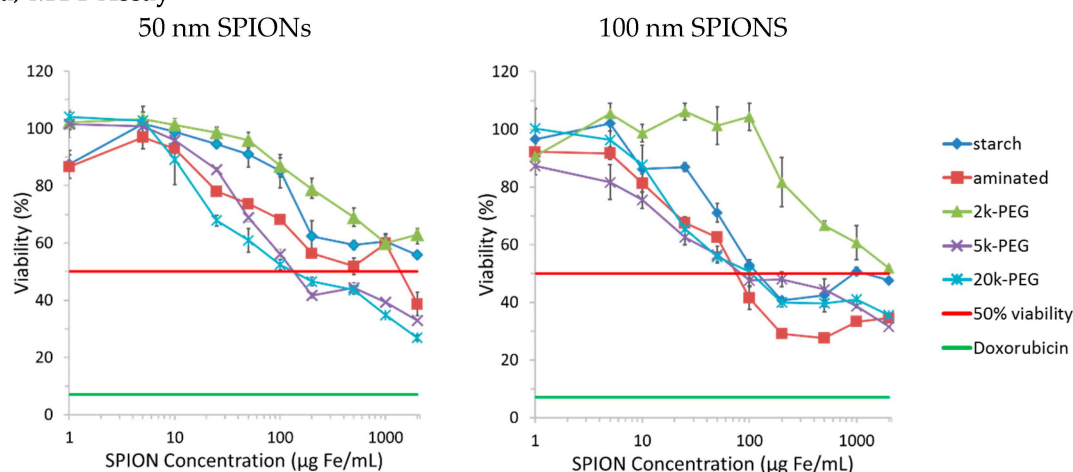
Toxicity studies were conducted in CHO-K1 cells with increasing concentrations of SPIONs, using the MTT and SRB assays. Preliminary results showed a time-dependent cytotoxicity with the greatest difference among tested SPIONs observed at 72 h, which was fixed as the incubation time for further studies. Cytotoxicity profiles of tested SPIONs are reported in Figure 1, with cell viability expressed relative to untreated, control cells whose viability is set as 100%. Doxorubicin (10 µM) was employed as a positive control for these experiments (green line). The half maximal inhibitory concentration (50% viability or IC₅₀) is indicated with a red line in all graphs. Mathematical regression was employed to approximate the IC₅₀ values for each particle with both the MTT and SRB assays; IC₅₀ values are reported in Table 3.

The MTT and SRB results showed similar cytotoxic tendencies. First, both 50 and 100 nm 2k-PEGylated SPIONs seemed to be better tolerated by CHO-K1 cells than the other coatings tested. The aminated 100 nm SPIONs, on the other hand, appeared to be the most toxic, except for the 50 nm SPIONs, as determined by their IC₅₀ values. It should also be pointed out that the aminated 50 nm SPION sample is the one that had the lower than expected ζ potential, although the amine content was high. The connection, if any, between this and the observed lower toxicity is not clear. An IC₅₀ value was not reached for 50 nm SPIONs with the starch and 2k Da PEG coatings, within the concentration range studied. In all cases, the 5k-PEG and 20k-PEG coated SPIONs were found to be significantly

more toxic than particles coated with the 2k Da PEG. A comparison of IC_{50} values, for both the MTT and SRB assays, also indicates that the 100 nm SPIONs present greater cytotoxicity than the 50 nm SPIONs. A greater range of mean SPION sizes needs to be tested to determine whether this is a linear trend or if there are SPION sizes that would yield a minimal and/or maximal toxicity.

Nanoparticle surfaces have been engineered to increase the *in vivo* circulation time [19,20,26]. Our results seem to indicate that PEG molecular weight and density could also be utilized to modulate the cytotoxicity of SPIONs. It should also be noted that surface chemistry plays a role in determining the composition of the protein corona that adsorbs onto the nanoparticle surface and, thus, also influences the uptake pathways followed by the particles [27].

(a) MTT Assay



(b) SRB Assay

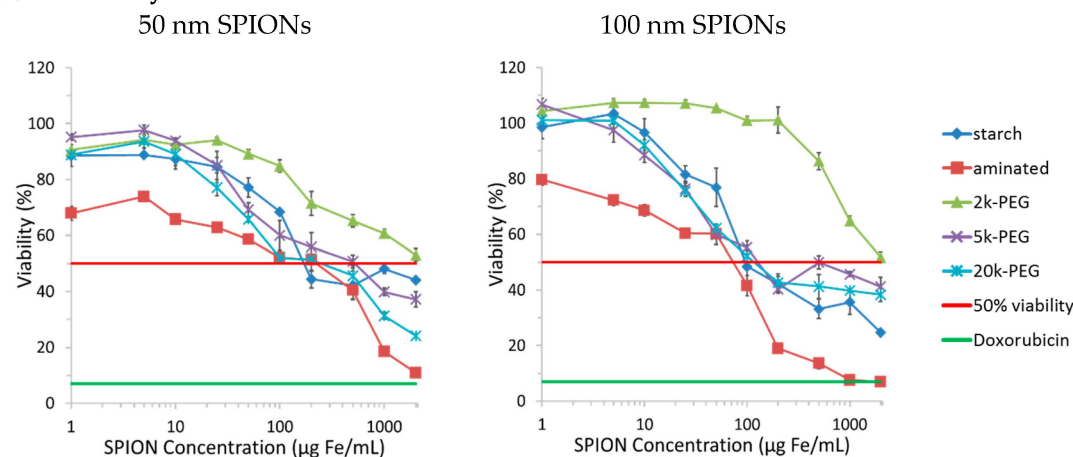


Figure 1. Cytotoxicity of superparamagnetic iron-oxide nanoparticles (SPIONs) in Chinese Hamster Ovary (CHO-K1) cells evaluated with the (a) tetrazolium dye 3-(4,5-dimethylthiazol-2-yl)-2,5-diphenyltetrazolium bromide (MTT) and (b) sulforhodamine B (SRB) assays. CHO-K1 cells were incubated with increasing concentrations of SPIONs for 72 h. The 50% viability of control cells (untreated) is represented by the red line. The viability of cells treated with 10 μM doxorubicin for 72 h (positive control) is shown by the green line.

Table 3. Half maximal inhibitory concentrations (IC₅₀) of SPIONs incubated with CHO-K1 cells.

Samples	IC ₅₀ (µg Fe/mL)			
	50 nm SPIONs		100 nm SPIONs	
	MTT	SRB	MTT	SRB
Starch	Not reached	621	436	124
Aminated	1119	252	69	35
2k-PEG	Not reached	1867	1796	1563
5k-PEG	217	483	66	351
20k-PEG	136	217	147	205

2.3. Exposure Time Affects the Observed SPION Toxicity

The *in vivo* blood half-life of SPIONs varies, depending on particle size and surface properties [20], from 2 h for dextran-coated 120–180 nm ferumoxide particles (Endorem[®], Feridex[®]) to 24–36 h for dextran-coated 15–30 nm ferumoxtran particles (Sinerem[®], Combidex[®]). In a recent study, the half-life of starch-coated SPIONs and those with 5k- and 2k-PEG coatings was found to be 0.12, 7.3, and 11.8 h, respectively, in male Fisher rats [20]. To mimic the potential *in vivo* contact time, CHO-K1 cells were incubated with SPIONs for a period of 24 h. The cytotoxicity was evaluated with the MTT assay after this contact time (Figure 2a). Alternatively, cells were also incubated with SPIONs for 24 h and then washed and cultured for another 48 h with fresh culture medium prior to analysis of cell viability (Figure 2b).

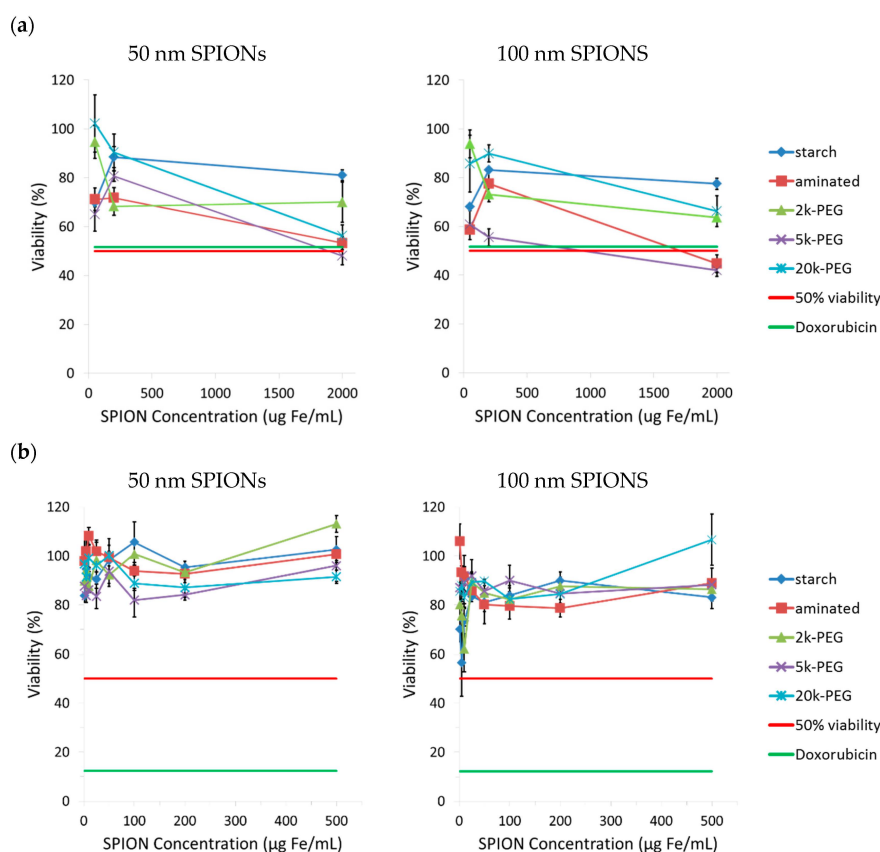


Figure 2. Assessment of the toxicity of SPIONs after, (a) 24 h incubation only, and (b) after 24 h incubation followed by 48 h of recovery in supplemented culture media; viability compared to untreated cells (control, 100% viability). The 50% viability of control cells (untreated) is represented by the red line. The viability of cells treated with 10 µM doxorubicin (positive control) is shown by the green line.

The viability of CHO-K1 cells varied between 100% and 50% when incubated 24 h with SPION concentrations up to 2000 $\mu\text{g Fe/mL}$ (Figure 2a). However, when cells were allowed a 48 h recovery period in complete fresh culture medium, cell viability remained above 80% for concentrations up to 500 $\mu\text{g Fe/mL}$. A few studies have shown that internalized SPIONs can be divided in daughter cells during cell division, and consequently decrease the iron content per cell [22]. The presence of exocytosis has also been reported [28]. The attenuation of toxicity due to reduction of intracellular SPION concentration by these mechanisms is a possible explanation for the different tendencies seen in Figure 2a,b, but more focused studies are needed to elucidate the true effects of these processes. Conversely, the viability of cells treated with 10 μM doxorubicin dropped from 50% to 11% despite washings and incubation in fresh culture media, probably due to permanent cellular damage. The extrapolation of these results to *in vivo* conditions is difficult because CHO-K1 cells are an immortalized cell line, which is not the case for normal cells from ovaries. Our *in vitro* studies with CHO-K1 cells, however, has shown that the tested SPIONs cause reversible, dose- and time-dependent toxicity in rapidly dividing cells.

2.4. The Cellular Uptake Kinetics of SPIONs in Chinese Hamster Ovary (CHO-K1) Cells Is Dependent on Their Surface Coating

Despite the large number of cellular uptake studies that have been performed with SPIONs of various size and coating, it remains unclear which physicochemical characteristics provide optimal uptake in non-phagocytic cells. A saturable time- and concentration-dependent uptake has been demonstrated in astrocytes for dimercaptosuccinate-coated SPIONs [29], and charge-dependent uptake in non-phagocytic T-cells [30] for different sizes of dextran-coated SPIONs. Moreover, aminated aminosilane-coated SPIONs showed the highest iron uptake in six different cell lines, compared to silica, dextran, or bare SPIONs [12]. However, only few studies have studied the cellular uptake kinetics of SPIONs [12], and none for cells derived from a reproductive organ.

Here, cell associated SPIONs were stained with Prussian blue and the intensity categorized into 5 grades, with grade 0 (orange/red, referring to the safranin staining of the cell membranes) showing no overt visible iron uptake in cells and grade 4 (dark blue, referring to the blue color obtained from Prussian blue staining of iron) showing maximum uptake. Average grades were assigned by grading all cells observed in 10 optical images taken at high magnification (400 \times). Thus, histograms in Figure 3 represent the uptake distribution and kinetics of SPIONs in CHO-K1 cells.

The pattern observed with staining of SPIONs in cells indicates that particles are found almost exclusively in the cytoplasm of cells (*i.e.*, not detectable in the nucleus). However, the staining employed does not differentiate between intracytoplasmic organelles, such as lysosomes. Once internalized, degradation of SPIONs through the lysosomal pathway is indeed considered the common metabolic pathway. The low pH environment in lysosomes is favorable for the solubilization of iron contained in SPIONs [31], releasing free iron ions in the cytoplasm.

While the uptake kinetics varied between tested SPIONs, the results indicate that surface properties have a greater influence on uptake than the particle size (at least between 50 and 100 nm SPIONs). Particles coated with 2k-PEG displayed the lowest rate of cellular uptake, followed by the starch SPIONs. Surprisingly, aminated, 5k- and 20k-PEG SPIONs showed similar uptake kinetics, although aminated and 20k-PEG SPIONs were taken up to a greater extent. It is interesting to note that the aminated SPIONs and the 5k- and 20k-PEGylated SPIONs all showed a similar trend in particle uptake, regardless of particle size. Each of these particles showed labeling of almost all cells within a 4 h incubation period and continued accumulation over 72 h. The 50 nm starch-coated particles, on the other hand, were only taken up by a few cells over 24 h and then all cells were lightly labeled after 72 h. The 100 nm starch-coated particles showed slightly faster kinetics with all cells labeled within the first 24 h and further accumulation over 72 h. SPIONs modified with the 2k Da PEG, on the other hand, exhibited very different cellular uptake kinetics with the CHO-K1 cells. While between 10%–15% of cells were labeled by 2k-PEG SPIONs in the first 30 min, this level of labeling remained fairly constant

over the entire 72 h incubation period after which only 26% and 9% of cells were labeled for the 50 and 100 nm SPIONs, respectively. It should be noted that these results correlate well with the toxicity results presented in Figure 1. The kinetic studies were carried out with SPION concentrations of 10 $\mu\text{g Fe/mL}$, a concentration at which no appreciable toxicity is observed with the 2k-PEG SPIONs but at which toxicity begins to appear with the other particles. Ongoing studies are being carried out to clarify the processes governing the behavior of these particles and to determine the cause for this dramatic difference in their interaction with the cells.

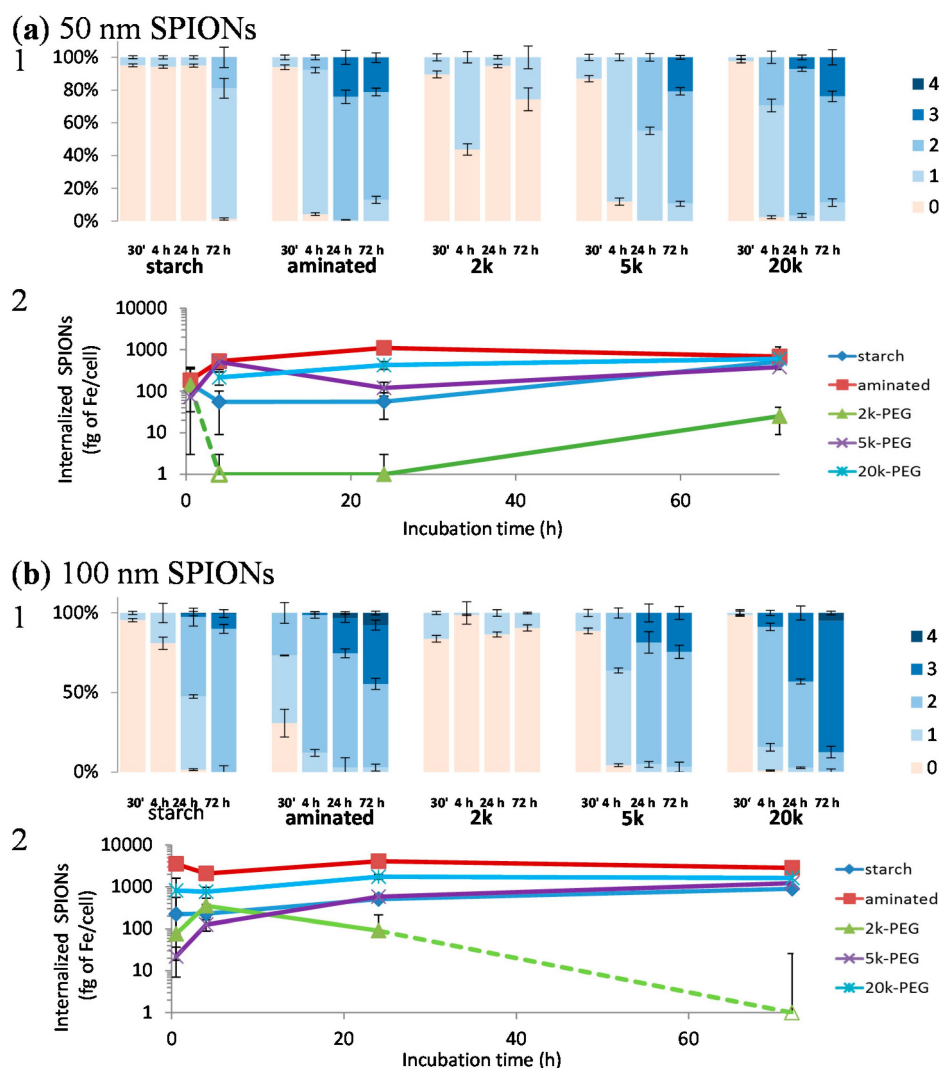


Figure 3. Kinetics of (a) 50 and (b) 100 nm SPION uptake by CHO-K1 cells, represented by (1) Average grading of particles, after 30 min, 4, 24, and 72 h of incubation. Grade 0 = no blue color, grade 1 = faint blue staining in cytoplasm, grade 2 = dense blue color in minor portions of cytoplasm (less than 50%), grade 3 = deep blue staining in most cytoplasm (>50%) and grade 4 = cell filled with intense, dark blue throughout; and (2) Quantification of internalized iron using a ferrozine assay is reported below the histograms, with evolution of the quantitative uptake over time. Hollow markers indicate concentrations below the detection limit of the assay (*i.e.*, zeros).

In the literature, the presence of positively charged amine groups on the coating of polyvinyl alcohol (PVA)-functionalized SPIONs has been shown to increase uptake in human melanoma cells, compared to PVA alone, carboxylate-, or thiol-PVA groups [29]. Moreover, the uptake of SPIONs can also be affected by variations in the protein corona that coats the particle upon addition to culture

media or exposure to serum proteins [27]. It has also been shown that SPION uptake can be inhibited by plasma proteins that coat the particles [30]. While the SPIONs showed varying rates of initial cellular uptake, over the 72 h period they appeared to approach the same maximum uptake regardless of surface coating; although the maximum approached was different for the 50 and 100 nm particles and the 2k-PEG SPIONs remained significantly lower than all other particles.

To further determine whether the observed variation in SPION toxicity is due to differences in particle properties or because of differences in cellular uptake, the results from the kinetic study were correlated with those from the cytotoxicity studies. IC₅₀ values from the SRB assay were used here as the MTT assay did not yield IC₅₀ values for two particles (*i.e.*, starch and 2k-PEG coated). As seen in Figure 4, there is an exponential decrease (*i.e.*, greater toxicity) in measured IC₅₀ values with increasing concentrations of internalized SPIONs, indicating that their internalization is an important step in the triggering of cell toxicity. The trend indicated that the toxicity of SPIONs, after 72 h incubation, approached the 35 µg Fe/mL IC₅₀ value of the 100 nm, aminated SPIONs.

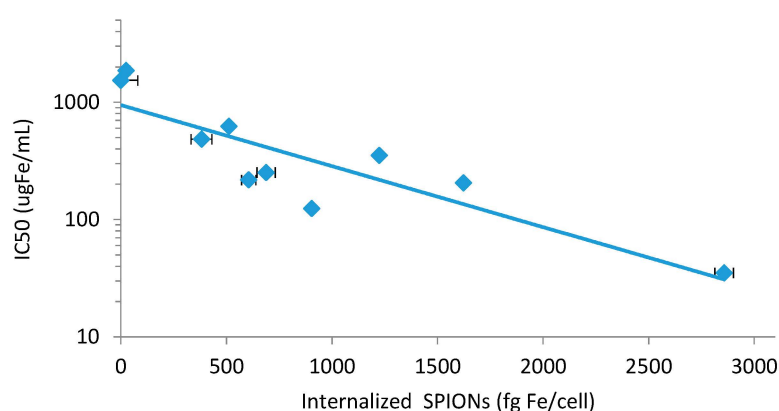


Figure 4. Correlation of the uptake kinetic of all type of SPIONs and their respective toxicity (represented by their IC₅₀ values calculated from the SRB assay) after 72 h incubation with CHO-K1 cells.

2.5. The Coating Affects the Generation of Reactive Oxygen Species (ROS) by SPIONs in CHO-K1 Cells

The production of reactive oxygen species (ROS) is often reported as the source of nanoparticle-associated toxicities [31,32]. Consequently, to further evaluate the mechanism of SPION cytotoxicity, H2DCFDA assay was performed to detect the generation of intracellular ROS. While it was clear that SPIONs did indeed generate significant ROS within CHO-K1 cells, in comparison to control, the study was unable to detect differences between the SPION particles due to signal saturation (Figure 5). Additional studies must be conducted to better quantify this process and its contribution to the observed cytotoxicity.

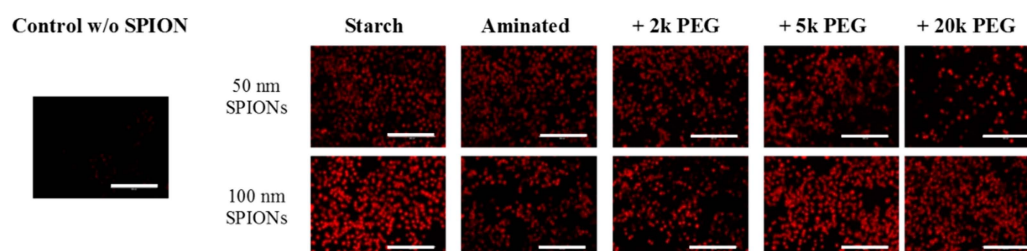


Figure 5. ROS production (red) in CHO-K1 cells following incubation with SPIONs was confirmed with the H2DCFDA assay. Control cells underwent the same assay but were not exposed to SPIONs. Scale bar = 200 µm.

2.6. Surface Properties Are Key to Determining the Cytotoxicity of SPIONs in CHO-K1 Cells

In this study, the uptake kinetics and cytotoxicity of starch, aminated and PEGylated SPIONs were determined in CHO-K1 cells. Taken together, the results suggest that the cytotoxicity of the tested SPIONs were due to the generation of ROS upon internalization of the particles. Since surface properties were found to significantly affect the kinetics and extent of internalization, the toxicity of SPIONs were found to be most dependent on the surface modification. It should, however, also be noted that toxicity of 100 nm SPIONs were generally greater than that of the corresponding 50 nm SPION with the same coating. This is interesting as at a given SPION concentration, on a mass of iron basis, the total surface area of the 50 nm particles will be expected to be approximately four-fold greater than that of the same iron mass of 100 nm SPIONs; although the specific surface area of the 100 nm SPIONs is greater on a per particle basis. Therefore, although surface effects seem to drive SPION toxicity, the effects of particle size cannot be ignored.

3. Experimental Section

3.1. Surface Modification of Starch-Coated SPIONs

Two different sizes of starch magnetite core nanoparticles (FluidMAG-D, autoclaved aqueous dispersion) were purchased from chemicell GmbH (Berlin, Germany). Manufacturer specifications indicated average hydrodynamic diameters of 50 and 100 nm, respectively, for the two SPIONs. Cross-linking of the starch coating, amination, and PEGylation of the particles was performed according to methods described by Cole *et al.* [20]. The physical properties of the SPIONs were confirmed to be in accordance with results published by Cole *et al.*, to which the readers are referred to for more details, but are not reproduced here for brevity. Briefly, starch moieties on the surface of iron-oxide nanoparticles were crosslinked with epichlorohydrin at room temperature for 24 h. The dialyzed product was then aminated with ammonium hydroxide (28%–30%) for 24 h at room temperature. After a second dialysis against water, one quarter of the product was labeled as aminated SPIONs. The remaining product was PEGylated using m-PEG-NHS (Nanocs, New York, NY, USA) in pH 8 phosphate buffer/DMSO solution incubated overnight. mPEG molecules with molecular weights of 2k, 5k, and 20k Da were used in this study. Ultrafiltration of the product was performed using a 10,000 molecular weight cut-off (MWCO) Slide-A-Lyzer dialysis cassette until PEG was no longer detectable in the washes using the Barium-Iodine assay described below.

3.2. Characterization of Starch-Coated, Aminated and PEGylated SPIONs

Hydrodynamic diameter and ζ potential of each SPION sample was determined by Dynamic Light Scattering (Zeta Sizer Nano-ZS from Malvern Instruments, Malvern, UK). SPIONs were dispersed in DI water or in phenol red-free culture media (Ham's F-12K Ultra Pure, Crystalgen, NY, USA), supplemented with fetal bovine serum (10%) and antibiotics (penicillin/streptomycin 1%). All DLS measurements were performed at 37 °C.

Measurement of amine content was performed using the fluorescamine assay [20]. A standard curve was established using solutions with known ethanolamine concentrations, starch SPIONs, and fluorescamine.

A barium iodine assay was used to quantify the average concentration of PEG attached on SPIONs. SPIONs were first dissolved in 1.4 HCl overnight prior to analysis. Standard curves were generated with starch-coated SPIONs (50 or 100 nm) and varying concentrations of free PEG molecules (2k, 5k, or 20k Da PEG).

All measurements for the physicochemical characterization of SPIONs were performed in triplicate, and results are expressed as the mean and standard error of mean.

3.3. Cell Line

The CHO-K1 cell line was obtained from Rajesh Amin, Department of Drug Discovery and Development, Auburn University, Auburn, AL, USA. Authentication of the cell line was complimentary confirmed by the National Institute of Standards and Technology, using a multiplex PCR assay (non commercial assay). Cells were maintained in Ham's F-12K Nutrient Mixture with L-glutamine (Corning cellgro, Manassas, VA, USA), supplemented with 10% fetal bovine serum and 1% penicillin/streptomycin, incubated at 37 °C in 5% CO₂.

3.4. Cell-Viability Assays

Cells were plated into 96-well flat-bottom plates at a starting density of 10⁴ cells per well. After an equilibration time of 12 to 24 h, until they reached 70%–80% confluency, culture media was removed and cells were treated in triplicate with increasing concentrations (1, 5, 10, 25, 50, 100, 200, 500, 1000, and 2000 µg Fe/mL) of the 10 different SPIONs suspended in culture media. Cell viability was then determined with 3-(4,5-dimethylthiazol-2-yl)-2,5-diphenyltetrazoliumbromide (MTT assay; AMRESCO, Solon, OH, USA) and sulforhodamine B (SRB; CytoScan™ SRB Cytotoxicity Assay kit, G Biosciences, St. Louis, MO, USA) assays. The MTT assay determines the viability of cells according to their metabolic activity, whereas the SRB assay non specifically detects the total protein content in cells.

Briefly, the MTT assay was conducted by incubating cells with a 2 mg/mL solution of MTT (50 µL) for 4 h. The supernatant was then aspirated and 150 µL of dimethyl sulfoxide (DMSO) was applied to the cells to solubilize the formed formazan crystals. Plates were agitated and then centrifuged (3000 rpm for 10 min) to pellet the SPIONs. Finally, 100 µL of the supernatant was collected and transferred into a clean 96-well flat-bottom plate. Absorbance was measured at 540 nm using a microplate reader (SpectraMax i3 multi-mode platform, Molecular Devices, Sunnyvale, CA, USA).

The SRB assay was conducted in accordance to instructions provided with the commercial kit, except that cells were washed twice with 1 × PBS prior to fixing of cell. Absorbance was measured at 540 nm using a microplate reader (SpectraMax i3 multi-mode platform, Molecular Devices).

3.4.1. Overall Toxicity after 72 h of Incubation

The overall toxicity of SPIONs were tested using the cell viability assay. CHO-K1 cells were incubated 72 h with particles and viability was assessed with MTT and SRB assays. For both assays, a positive control was also added to verify the response of the cell line (Doxorubicin 10 µM) [33]. Results are reported as the percentage of viable cells compared to untreated cells (negative control, by definition considered 100% viable). Cell-viability results are presented as means ± standard error of the mean (SEM) of triplicates for each concentration tested. Results are reported in Figure 1.

3.4.2. Toxicity in Conditions that Mimic *in Vivo* Contact Time of SPIONs

To mimic potential contact time of SPIONs in the body, CHO-K1 cells were seeded in 96-well plates at 10⁴ cells/well and equilibrated overnight. They were incubated for 24 h at 37 °C with SPIONs at the following concentrations: 50, 200, and 2000 µg Fe/mL. Alternatively, CHO-K1 cells were incubated with 1, 5, 10, 25, 50, 100, 200, and 500 µg Fe/mL, then washed and cultured in fresh culture medium for another 48 h. Cytotoxicity was evaluated with the MTT assay (described above). Doxorubicin (10 µM) was employed as a positive control for the experiment (wells containing Doxorubicin were also washed after 24 h). Results are presented in Figure 2.

3.5. Characterization of SPION Uptake by CHO-K1 Cells

3.5.1. Uptake Kinetics

To determine the uptake characteristics of tested SPIONs in CHO-K1 cells, qualitative and quantitative measurements were performed based on the detection of iron in SPIONs. First, the

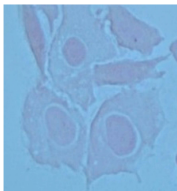
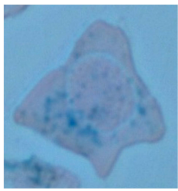
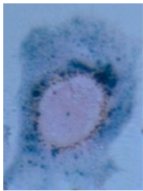
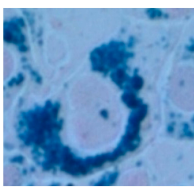
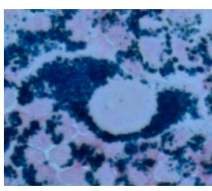
presence of iron inside cells was visually detected by staining iron with Prussian blue. The presence of iron in cells was also quantified using a ferrozine assay, as previously described [34].

3.5.2. Direct Microscopic Examination

Briefly, CHO-K1 cells were plated in a 24-well plate at a starting density of 5×10^4 cells per well. After overnight equilibration, the culture media was removed and the cells incubated with SPIONs at $10 \mu\text{g Fe/mL}$, for 30 min, 4, 24, or 72 h. Cells were then washed twice with $1 \times$ PBS, and stained with a Prussian blue staining solution (2% potassium ferrocyanide and 2% hydrochloric acid, Electron Microscopy Sciences, Hatfield, PA, USA) for 20 min at room temperature. After washing five times with PBS $1 \times$, cells were then counterstained with safranin for 2 min. The cell membranes were stained red/orange, whereas iron was stained in blue. To ensure good representation of samples, uptake was assessed with 10 images acquired at $400\times$ magnification from various areas of two different wells.

A scoring system (detailed in Table 4) was established to characterize the amount of iron internalized in each cell. This scoring system is derived from a protocol described in Human and Veterinary Medicine to assess hemosiderosis in alveolar macrophages [35,36]. All entire cells found within an acquired image were graded. Sample names were blinded prior to analysis but 10 pictures from one sample type were graded at the same time. Results are presented in Figure 3.

Table 4. Scheme for scoring of cellular uptake of SPIONs. The following set of images are illustrative of the grading used to quantify SPION uptake by CHO-K1 cells. Cells were stained with Prussian blue (blue spots that indicate presence of iron) and Safranin (pinkish coloration of cellular membranes). Cells shown are representative of those seen at $400\times$ magnification. A scale bar is not provided since these are only representative cell images that were digitally extracted from original images that contained many cells with varying SPION uptake.

Grade 0	Grade 1	Grade 2	Grade 3	Grade 4
No blue color	Faint blue staining in cytoplasm	Dense blue color in $<50\%$ of cytoplasm	Deep blue staining in $>50\%$ of cytoplasm	Cell cytoplasm filled with intense dark blue
				

Determination of Internalized Iron Concentration Using the Ferrozine Assay

The amount of internalized iron was quantified with a ferrozine-based assay [34], normalized against the number of cells and the iron physiologically present in cells under normal conditions. A preliminary study was performed to establish a standard curve that correlates the CHO-K1 cell number and the result of the Bradford assay (colorimetric assay). Results of iron taken up by cells were also in accordance to previous evaluations (data shown in Figure 3).

3.6. Overall Reactive Oxygen Species (ROS) Generation

The CM-H2DCFDA kit purchased from Invitrogen was used for the measurement of overall ROS levels. Briefly, 2.5×10^4 cells were plated in 24-well plates in duplicate. After overnight equilibration, cells were treated with tested SPIONs for 48 h at a final concentration of $200 \mu\text{g Fe/mL}$. Prior to the end of treatment, culture media was removed and DCFDA in PBS $1 \times$ was added to each well at a final concentration of $7 \mu\text{M}$ and incubated in the dark at 37°C for 45 min. After treatment, the fluorescence intensity of CM-H2DCFDA in cells was evaluated using a fluorescence cell imaging system (Evos[®], ThermoFisher Scientific, Waltham, MA, USA). Data shown in Figure 5.

4. Conclusions

CHO-K1 cells internalize SPIONs with various types of coating in a concentration-dependent manner. The toxicity profiles observed for the SPIONs suggest the plausibility of saturable uptake kinetics, as previously described in astrocytes [37]. Several physicochemical parameters are described in literature as potential variables affecting uptake and, consequently, cytotoxicity. Assessing and understanding their impact is vital to the development of novel, targeted cellular delivery carriers. While size is an important parameter, the effects were less than expected, although only two mean particle sizes with potential overlapping size distributions were studied. Surface charge can have a significant impact on the rate and route of SPION uptake. It is generally accepted that the negative charge of cell plasma membranes leads to strong interactions with positively charged nanoparticles and their increased uptake [38]. In this study, positively-charged, aminated SPIONs were indeed found to be taken up the most rapidly and to the greatest extent, followed by 20k-PEGylated SPIONs and 5k-PEGylated SPIONs. Surprisingly, 2k-PEGylated SPIONs had a positive surface charge similar to that of the 20k- and 5k-PEGylated SPIONs but were taken up to a lesser extent. Cytotoxicity results showed that the 2k-PEG SPIONs were the best tolerated at all concentrations studied. Similarly, starch SPIONs seemed to be better tolerated at concentrations below 100 µg Fe/mL compared to the 5k- and 20k-PEGylated SPIONs, possibly attributed to lower uptake induced by their slightly negative charge. The 2k-PEG coating, which yielded the densest surface coating of SPIONs among the PEGs tested, showed the least degree of cytotoxicity against CHO-K1 cells. Overall, the correlation between surface properties of SPIONs and their cellular uptake, and the correlation between their uptake and cytotoxicity, suggests a means to modulate the disposition and biocompatibility of nanoparticles. Further studies need to be conducted to better characterize the nature of the interaction between these particles and cells, and also to elucidate their subcellular localization. It will also be important to study their effects on the reproductive system using *in vivo* models.

Acknowledgments: This material was partially supported by the National Science Foundation under Grant No. EPS-1158862 Subagreement 34-21530-200-76190, by a Department of Defense FY2012 Prostate Cancer Research Program (PCRP) Idea Development Award (Award #W81XWH-13-1-0288), and by a grant from the Auburn University Research Initiative in Cancer (AURIC). The authors would also like to thank R. Amin and S. Mouli (Auburn University, Harrison School of Pharmacy, Department of Drug Discovery and Development) for reagents and advice; and J. Almeida (NIST) for the complimentary authentication of the CHO-K1 cell line.

Author Contributions: Camille C. Hanot, Young Suk Choi and Allan E. David conceived and designed the experiments; Camille C. Hanot, Young Suk Choi and Tareq B. Anani performed the experiments; Camille C. Hanot, Allan E. David and Young Suk Choi analyzed the data; Young Suk Choi, Allan E. David and Dharsan Soundarrajan contributed reagents/materials/analysis tools; Camille C. Hanot and Allan E. David wrote the paper.

Conflicts of Interest: The authors declare no conflict of interest.

References

1. Liu, G.; Gao, J.; Ai, H.; Chen, X. Applications and potential toxicity of magnetic iron oxide nanoparticles. *Small* **2013**, *9*, 1533–1545. [CrossRef] [PubMed]
2. Wu, W.; Wu, Z.; Yu, T.; Jiang, C.; Kim, W.S. Recent progress on magnetic iron oxide nanoparticles: Synthesis, surface functional strategies and biomedical applications. *Sci. Technol. Adv. Mater.* **2015**, *16*, 023501. [CrossRef]
3. Neuwelt, A.; Sidhu, N.; Hu, C.-A.A.; Mlady, G.; Eberhardt, S.C.; Sillerud, L.O. Iron-based superparamagnetic nanoparticle contrast agents for MRI of infection and inflammation. *AJR Am. J. Roentgenol.* **2015**, *204*, W302–W313. [CrossRef] [PubMed]
4. Lam, T.; Pouliot, P.; Avti, P.K.; Lesage, F.; Kakkar, A.K. Superparamagnetic iron oxide based nanoprobes for imaging and theranostics. *Adv. Colloid Interface Sci.* **2013**, *199–200*, 95–113. [CrossRef] [PubMed]
5. Cortajarena, A.L.; Ortega, D.; Ocampo, S.M.; Gonzalez-García, A.; Couleaud, P.; Miranda, R.; Belda-Iniesta, C.; Ayuso-Sacido, A. Engineering iron oxide nanoparticles for clinical settings. *Nanobiomedicine* **2014**. [CrossRef]
6. Wang, Y.-X.J. Superparamagnetic iron oxide based MRI contrast agents: Current status of clinical applicatio. *Quant. Imaging Med. Surg.* **2011**, *1*, 35–40. [PubMed]

7. Levya, M.; Luciania, N.; Alloyeaud, D.; Elgrablic, D.; Deveauxd, V.; Pechoux, C.; Chate, S.; Wangb, G.; Vatsa, N.; Gendronf, F.; *et al.* Long term *in vivo* biotransformation of iron oxide nanoparticles. *Biomaterials* **2011**, *32*, 3988–3999. [CrossRef] [PubMed]
8. Bernd, H.; de Kerviler, E.; Gaillard, S.; Bonnemain, B. Safety and tolerability of ultrasmall superparamagnetic iron oxide contrast agent: Comprehensive analysis of a clinical development program, a dextran-coated ultrasmall superparamagnetic ferumoxytol nanoparticle. *Investig. Radiol.* **2009**, *44*, 336–342. [CrossRef] [PubMed]
9. Kurata, T.; Tanimoto, A.; Shinmoto, H.; Yuasa, Y.; Kuribayashi, S. Questionnaire survey of acute and delayed adverse reactions to ferumoxides. *Radiat. Med.* **2005**, *23*, 468–473. [PubMed]
10. Bourrinet, P.; Bengel, H.H.; Bonnemain, B.; Dencausse, A.; Idee, J.M.; Jacobs, P.M.; Lewis, J.M. Preclinical safety and pharmacokinetic profile of ferumoxtran-10, an ultrasmall superparamagnetic iron oxide magnetic resonance contrast agent. *Investig. Radiol.* **2006**, *41*, 313–324. [CrossRef] [PubMed]
11. Zhu, X.; Tian, S.; Cai, Z. Toxicity assessment of iron oxide nanoparticles in Zebrafish (*Danio rerio*) early life stages. *PLoS ONE* **2012**, *7*, e46286. [CrossRef] [PubMed]
12. Zhu, X.M.; Wang, Y.-X.J.; Leung, K.C.-F.; Lee, S.-F.; Zhao, F.; Wang, D.-W.; Lai, J.M.-Y.; Wan, C.; Cheng, C.H.-K.; Ahuja, A.T. Enhanced cellular uptake of aminosilane-coated superparamagnetic iron oxide nanoparticles in mammalian cell lines. *Int. J. Nanomed.* **2012**, *7*, 953–964.
13. Levy, M.; Lagarde, F.; Maraloiu, V.A.; Blanchin, M.G.; Gendron, F.; Wilhelm, C.; Gazeau, F. Degradability of superparamagnetic nanoparticles in a model of intracellular environment: Follow-up of magnetic, structural and chemical properties. *Nanotechnology* **2010**, *21*, 395103. [CrossRef] [PubMed]
14. Mahon, E.; Hristov, D.L.; Dawson, K.A. Stabilising fluorescent silicananoparticles against dissolution effects for biological studies. *Chem. Commun.* **2012**, *48*, 7970–7972. [CrossRef] [PubMed]
15. Fleischer, C.C.; Payne, C.K. Secondary structure of corona proteins determines the cell surface receptors used by nanoparticles. *J. Phys. Chem. B* **2014**, *118*, 14017–14026. [CrossRef] [PubMed]
16. Mahmoudi, M.; Laurent, S.; Shokrgozar, M.A.; Hosseinkhani, M. Toxicity evaluations of superparamagnetic iron oxide nanoparticles: Cell “vision” versus physicochemical properties of nanoparticles. *ACS Nano* **2011**, *5*, 7263–7276. [CrossRef] [PubMed]
17. Park, Y.; Whitaker, R.D.; Nap, R.J.; Paulsen, J.L.; Mathiyazhagan, V.; Doerrer, L.H.; Song, Y.Q.; Hurlimann, M.D.; Szleifer, I.; Wong, J.Y. Stability of superparamagnetic iron oxide nanoparticles at different pH values: experimental and theoretical analysis. *Langmuir* **2012**, *28*, 6246–6255. [CrossRef] [PubMed]
18. Laurent, S.; Forge, D.; Port, M.; Roch, A.; Robic, C.; Vander Elst, L.; Muller, R.N. Magnetic iron oxide nanoparticles: Synthesis, stabilization, vectorization, physicochemical characterizations, and biological applications. *Chem. Rev.* **2008**, *108*, 2064–2110. [CrossRef] [PubMed]
19. Mojica Piscioti, M.L.; Lima, E., Jr.; Vasquez Mansilla, M.; Tognoli, V.E.; Troiani, H.E.; Pasa, A.A.; Creczynski-Pasa, T.B.; Silva, A.H.; Gurman, P.; Colombo, L.; *et al.* *In vitro* and *in vivo* experiments with iron oxide nanoparticles functionalized with dextran or polyethylene glycol for medical applications: Magnetic targeting. *J. Biomed. Mater. Res. Part B* **2014**, *102B*, 860–868. [CrossRef] [PubMed]
20. Cole, A.J.; David, A.E.; Wang, J.; Galbán, C.J.; Hill, H.L.; Yang, V.C. Polyethylene glycol modified, cross-linked starch-coated iron oxide nanoparticles for enhanced magnetic tumor targeting. *Biomaterials* **2011**, *32*, 2183–2193. [CrossRef] [PubMed]
21. Park, Y.C.; Smith, J.B.; Pham, T.; Whitaker, R.D.; Sucato, C.A.; Hamilton, J.A.; Bartolak-Suki, E.; Wong, J.Y. Effect of PEG molecular weight on stability, T_2 contrast, cytotoxicity, and cellular uptake of superparamagnetic iron oxide nanoparticles (SPIONs). *Colloids Surf. B Biointerfaces* **2014**, *119*, 106–114. [CrossRef] [PubMed]
22. Gu, J.L.; Xu, H.F.; Han, Y.H.; Dai, W.; Hao, W.; Wang, C.Y.; Gu, N.; Xu, H.Y.; Cao, J.M. The internalization pathway, metabolic fate and biological effect of superparamagnetic iron oxide nanoparticles in the macrophage-like RAW264.7 cell. *Sci. China Life Sci.* **2011**, *54*, 793–805. [CrossRef] [PubMed]
23. Gupta, A.K.; Gupta, M. Cytotoxicity suppression and cellular uptake enhancement of surface modified magnetic nanoparticles. *Biomaterials* **2005**, *26*, 1565–1573. [CrossRef] [PubMed]
24. Rivet, C.J.; Yuan, Y.; Borca-Tasciuc, D.A.; Gilbert, R.J. Altering iron oxide nanoparticle surface properties induce cortical neuron cytotoxicity. *Chem. Res. Toxicol.* **2012**, *25*, 153–161. [CrossRef] [PubMed]

25. Wilhelm, C.; Billotey, C.; Roger, J.; Pons, J.N.; Bacri, J.C.; Gazeau, F. Intracellular uptake of anionic superparamagnetic nanoparticles as a function of their surface coating. *Biomaterials* **2003**, *24*, 1001–1011. [CrossRef]
26. Klibanov, A.L.; Maruyama, K.; Torchilin, V.P.; Huang, L. Amphipathic polyethyleneglycols effectively prolong the circulation time of liposomes. *FEBS Lett.* **1990**, *268*, 235–237. [CrossRef]
27. Fleischer, C.C.; Payne, C.K. Nanoparticle–Cell interactions: Molecular structure of the protein corona and cellular outcomes. *Acc. Chem. Res.* **2014**, *47*, 2651–2659. [CrossRef] [PubMed]
28. Oh, N.; Park, J.H. Endocytosis and exocytosis of nanoparticles in mammalian cells. *Int. J. Nanomed.* **2014**, *9*, 51–63.
29. Petri-Fink, A.; Chastellain, M.; Juillerat-Jeanneret, L.; Ferrari, A.; Hofmann, H. Development of functionalized superparamagnetic iron oxide nanoparticles for interaction with human cancer cells. *Biomaterials* **2005**, *26*, 2685–2694. [CrossRef] [PubMed]
30. Petri-Fink, A.; Steitz, B.; Finka, A.; Salaklang, J.; Hofmann, H. Effect of cell media on polymer coated superparamagnetic iron oxide nanoparticles (SPIONs): Colloidal stability, cytotoxicity, and cellular uptake studies. *Eur. J. Pharm. Biopharm.* **2008**, *68*, 129–137. [CrossRef] [PubMed]
31. Skotland, T.; Sontum, P.C.; Oulie, I. *In vitro* stability analyses as a model for metabolism of ferromagnetic particles (Clariscan™), a contrast agent for magnetic resonance imaging. *J Pharm Biomed Anal.* **2002**, *28*, 323–329. [CrossRef]
32. Lane, D.J.R.; Merlot, A.M.; Huang, M.-L.H.; Bae, D.H.; Jansson, P.J.; Sahni, S.; Kalinowski, D.S.; Richardson, D.R. Cellular iron uptake, trafficking and metabolism: Key molecules and mechanisms and their roles in disease. *Biochim. Biophys. Acta* **2015**, *1853*, 1130–1144. [CrossRef] [PubMed]
33. Aroui, S.; Mili, D.; Brahim, S.; de Waard, M.; Kenani, A. Doxorubicin coupled to penetratin promotes apoptosis in CHO cells by a mechanism involving c-Jun NH2-terminal kinase. *Biochem. Biophys. Res. Commun.* **2010**, *396*, 908–914. [CrossRef] [PubMed]
34. Riemer, J.; Hoepken, H.H.; Czerwinska, H.; Robinson, S.R.; Dringen, R. Colorimetric ferrozine-based assay for the quantitation of iron in cultured cells. *Anal. Biochem.* **2004**, *331*, 370–375. [CrossRef] [PubMed]
35. Golde, D.W.; Drew, W.L.; Klein, H.Z.; Finley, T.N.; Cline, M.J. Occult pulmonary haemorrhage in leukaemia. *Br. Med. J.* **1975**, *2*, 166–168. [CrossRef] [PubMed]
36. Doucet, M.Y.; Viel, L. Alveolar macrophage graded hemosiderin score from bronchoalveolar lavage in horses with exercise-induced pulmonary hemorrhage and controls. *J. Vet. Intern. Med.* **2002**, *16*, 281–286. [CrossRef] [PubMed]
37. Geppert, M.; Hohnholt, M.C.; Thiel, K.; Nurnberger, S.; Grunwald, I.; Rezwani, K.; Dringen, R. Uptake of dimercaptosuccinate-coated magnetic iron oxide nanoparticles by cultured brain astrocytes. *Nanotechnology* **2011**, *22*, 145101. [CrossRef] [PubMed]
38. Sun, Z.; Yathindranath, V.; Worden, M.; Thliveris, J.A.; Chu, S.; Parkinson, F.E.; Hegmann, T.; Miller, D.W. Characterization of cellular uptake and toxicity of aminosilane-coated iron oxide nanoparticles with different charges in central nervous system-relevant cell culture models. *Int. J. Nanomed.* **2013**, *8*, 961–970. [CrossRef] [PubMed]



Article

Exploiting Size-Dependent Drag and Magnetic Forces for Size-Specific Separation of Magnetic Nanoparticles

Hunter B. Rogers ¹, Tareq Anani ¹, Young Suk Choi ¹, Ronald J. Beyers ² and Allan E. David ^{1,*}

¹ Department of Chemical Engineering, Auburn University, 212 Ross Hall, Auburn, AL 36849, USA; E-Mails: hunterrogers2014@u.northwestern.edu (H.B.R.); tba0008@tigermail.auburn.edu (T.A.); yzc0036@auburn.edu (Y.S.C.)

² Auburn University MRI Research Center, Auburn, AL 36849, USA; E-Mail: rjb0018@auburn.edu

* Author to whom correspondence should be addressed; E-Mail: aedavid@auburn.edu; Tel.: +1-334-844-8119.

Academic Editor: O. Thompson Mefford

Received: 30 June 2015 / Accepted: 10 August 2015 / Published: 21 August 2015

Abstract: Realizing the full potential of magnetic nanoparticles (MNPs) in nanomedicine requires the optimization of their physical and chemical properties. Elucidation of the effects of these properties on clinical diagnostic or therapeutic properties, however, requires the synthesis or purification of homogenous samples, which has proved to be difficult. While initial simulations indicated that size-selective separation could be achieved by flowing magnetic nanoparticles through a magnetic field, subsequent *in vitro* experiments were unable to reproduce the predicted results. Magnetic field-flow fractionation, however, was found to be an effective method for the separation of polydisperse suspensions of iron oxide nanoparticles with diameters greater than 20 nm. While similar methods have been used to separate magnetic nanoparticles before, no previous work has been done with magnetic nanoparticles between 20 and 200 nm. Both transmission electron microscopy (TEM) and dynamic light scattering (DLS) analysis were used to confirm the size of the MNPs. Further development of this work could lead to MNPs with the narrow size distributions necessary for their *in vitro* and *in vivo* optimization.

Keywords: field-flow fractionation; iron oxide nanoparticles; size separation; magnetic nanoparticles; nanomedicine

1. Introduction

Nanomedicine is a broad area of research focused on the utilization of nanomaterials for the diagnosis, treatment, and prevention of diseases [1]. Biomedical applications present a unique opportunity to create engineered nanomaterials with highly controlled properties and functions that are comparable in scale to biological molecules and structures [2]. This is especially relevant for the fields of biomimetic nanomaterials, targeted drug delivery systems, and diagnostic imaging agents [3,4]. In contrast to the ever-growing list of nanomaterials researched for medical applications, the number of technologies actually approved for clinical use is relatively small. This is, in part, due to an overall paucity of fundamental knowledge and a lack of understanding of how the physical and chemical properties of nanomaterials affect their interactions with biological systems, and the associated uncertainty in their safety and toxicity profiles [5].

It is known that the behavior of nanomaterials within biological environments, including their stability and biodistribution, is dependent on their chemical composition and physical properties, such as size and geometry [6]. For nanomaterials to achieve their full potential in clinical applications, the fundamental principles governing their physio-chemical properties and the effects of these properties on physiological processes must be determined. However, obtaining nanoparticles of homogenous composition, either by finely controlled synthesis or through separation processes, has proven to be challenging. Particle size, in particular, can have a significant effect on the fate of nanoparticles once introduced into the body. For example, it has been shown that nanomaterials smaller than 6 nm are filtered out by the kidneys while those larger than 200 nm are more avidly taken up by macrophages and found to accumulate within the liver and spleen [7–9]. The biodistribution and pharmacokinetics of nanomaterials can also be affected by disease states. With cancer, for example, tumors typically possess a leaky vasculature and altered lymphatic drainage that results in the enhanced permeability and retention (EPR) effect, which enables extravasation of nanomaterials into the tumor microenvironment, with particles of size less than 200 nm typically providing greatest tumor penetration [10,11].

Magnetic nanoparticles (MNPs), specifically those composed of iron oxide, have been studied extensively for use in a variety of applications in nanomedicine, especially in the area of drug delivery and biomedical imaging [12–15]. In fact, several MNP formulations have been approved for clinical application as imaging contrast agents (e.g., Feridex[®]/Endorem[®], Resovist[®]/Cliavist[®], and Sinarem[®]/Combidx[®]) but commercial production has been halted due to poor clinical performance [16–18]. An improved understanding of the structure-property-performance relationships of MNPs could significantly improve their clinical application. While synthesis of iron oxide nanoparticles having monodisperse diameters less than 30 nm is well established, the synthesis of larger, monodisperse, iron oxide nanoparticles has proved challenging and greatly limited their optimization for biomedical applications. [19–21]. Batch-to-batch variability in nanoparticle production and broad size distributions raise safety concerns for clinical application due to the dependence of pharmacokinetics and biodistribution on the particle's physical and chemical properties [22]. In order to promote the clinical translation of MNPs, methods must be developed that either allow for synthesis of homogenous nanoparticles or enable their size-selective fractionation post-synthesis.

One potential solution to this problem is the use of magnetic field-flow fractionation (mFFF). This process, based on the separation of particles via the combined effects of the size-dependent drag

and magnetic forces, was first reported in 1980 by Vickrey and Garcia-Ramirez who wrapped Teflon tubing around a small electromagnet in an attempt to separate nickel complexes of bovine serum albumin from a fluid [23]. While a number of studies in literature report the use of various mFFF approaches, these primarily focus on the use of mFFF for characterizing small volumes of micro- or nano-particles or for the separation of magnetic particles from non-magnetic materials [24–26]. Very little attention has been given to mFFF as a size-specific separation technique for magnetic nanoparticles, especially for nanoparticles within the size range relevant for biomedical applications. The use of high gradient magnetic separation (HGMS) has been used by several groups to separate colloid suspensions of large magnetic nanoparticles, but the focus was not necessarily on the sorting of a polydisperse MNP suspension into multiple samples having narrower and controlled size distributions [27,28]. Beveridge *et al.* did report the use of a differential magnetic catch and release as a size-selective separation technique; however, their work focused on magnetic nanoparticles with diameters less than 20 nm [29]. The focus of this study is on the separation of MNPs with a hydrodynamic diameter in the range of 50–400 nm, which have potential biomedical application. Several prototypes for MNP separation were tested and the polydisperse MNPs ultimately separated into fractions having a narrower size distribution. This ability to separate magnetic nanoparticles according to their size ultimately enables the fundamental studies required to advance the use of magnetic nanoparticles in medicine.

2. Theory

Magnetic nanoparticles introduced into a mFFF system experience drag and magnetic forces in proportion to particle size. Very small particles, such as those on the nanoscale, also exhibit random Brownian motion, which can significantly affect nanoparticle behavior. For small, spherical particles in a fluid possessing a small Reynolds number ($Re < 1$), the drag force F_D can be described using Stokes drag, which is defined as:

$$F_D = 6\pi\eta rv \quad (1)$$

where η is the fluid viscosity, r is the hydrodynamic radius of the particle, and v is the fluid velocity [30]. The drag force is therefore directly proportional to the hydrodynamic radius of the particle. The magnetic force \vec{F}_M experienced by a magnetic particle within an applied magnetic field \vec{B} is given by the following equation:

$$\vec{F}_M = (\vec{m} \cdot \nabla) \vec{B} \quad (2)$$

where \vec{m} is the magnetic moment of the particle, calculated using the equation:

$$\vec{m} = \rho V \vec{M} \quad (3)$$

where ρ is the particle density, V is the volume of magnetic material in the particle, and \vec{M} is the magnetization of the particle [31]. According to Equation (3), the magnetic force experienced by a particle is proportional to $\sim r^3$ —increasing with size of the MNP, while the magnitude of the drag force (Equation (1)) is proportional to r . This dependence of the drag and magnetic forces on particle size provides a means to manipulate magnetic nanoparticles in a size-dependent manner.

As mentioned previously, for very small particles in a fluid, molecular collisions result in a source of diffusion known as Brownian motion. The Brownian diffusion length, L_D , traversed by a particle in two-dimensions over some time interval dt is approximated by the equation:

$$L_D = \sqrt{4D \, dt} \quad (4)$$

where D is the particle-specific diffusion coefficient, defined as:

$$D = \frac{k_B T}{6\pi\eta r} \quad (5)$$

where k_B is the Boltzmann's constant and T is the absolute temperature [32]. This relation shows that diffusion due to Brownian motion is also size-dependent and that the rate of diffusion decreases with increasing particle size. Taken together, these equations can be used to predict the movement of MNPs under the influence of drag and magnetic forces and Brownian motion.

3. Results and Discussion

3.1. Modeling the Effects of Drag and Magnetic Forces

A Matlab simulation was developed to study the feasibility of separating magnetic nanoparticles of sizes between 50 and 400 nm using the proposed approach. The simulation was based on a proposed experimental design that included 1.6 mm I.D. tubing of length 60 mm running parallel to a magnet, as shown in Figure 1. A Y-split at the end of the tubing ($x = 60$ mm) facilitated separation of MNPs based on their y -position. If the final y -position of a particle was greater than zero (center of the channel is at $y = 0$) then it was considered to be in Fraction 1, while those at or below the line were considered to be in Fraction 2. The magnetic field was derived from a series of five $\frac{1}{4}$ " diameter \times $\frac{1}{4}$ " length cylindrical neodymium magnets (Cat No.: D44-N52, K & J Magnetics, Pipersville, PA, USA) spaced 7.5 mm apart, as shown in Figure 2a. The magnetic flux density map (Figure 2a) was generated using data provided by the manufacturer and assuming non-interacting magnets.

Simulation of Particle Trajectories

Particle trajectories were predicted by force balance, to determine acceleration and velocity, on a single particle at some coordinate ($x_{MNP}(t)$, $y_{MNP}(t)$). The new position of the particle, after a time-step dt , was determined using the following equations:

$$x_{MNP}(t + dt) = x_{MNP}(t) + L_{Dx} + \left[\frac{v_x(t) + v_x(t + 1)}{2} \right] dt \quad (6)$$

$$y_{MNP}(t + dt) = y_{MNP}(t) + L_{Dy} + \left[\frac{v_y(t) + v_y(t + 1)}{2} \right] dt \quad (7)$$

where L_{Dx} and L_{Dy} refer to the diffusion length in the x and y -direction, respectively, and v_x and v_y are the respective velocities in the x and y -directions. At each time step, the Brownian diffusion of particles was determined by assigning a random fraction of the size-dependent diffusion length, L_D , to the x - and y -directions.

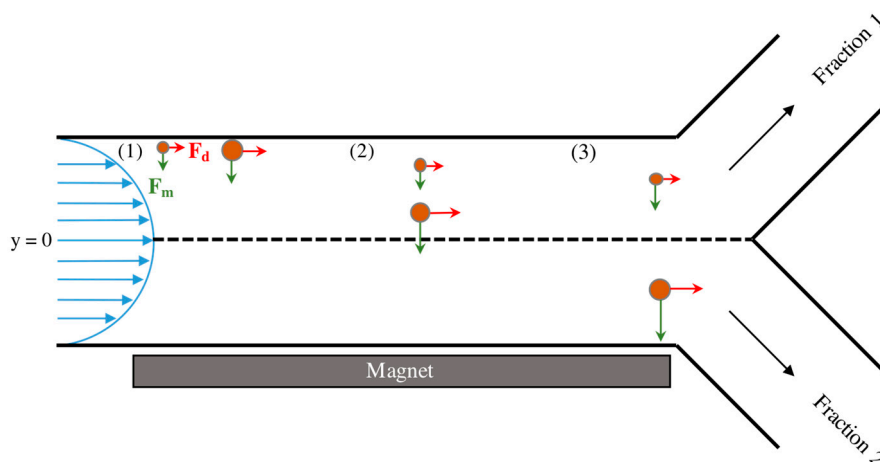


Figure 1. Illustration of the proposed experimental setup and the force balances experienced by two differently sized magnetic nanoparticles as they flow through the system. Green arrows represent the magnetic force (F_M) and red arrows represent the drag force (F_D). At position (1), the two MNPs are introduced to magnetic field in flow at the wall opposite the magnet. At a later time, the two particles reach position (2) and have separated from each other in the y -direction due to the increased magnetic force experienced by the larger MNP. Upon reaching the end of the channel at position (3), the larger of the two particles has traversed past the midline of the channel ($y = 0$) and will therefore be collected in Fraction 2. The smaller particle remains above $y = 0$ and will be collected in Fraction 1.

To mimic the injection of particles through a small capillary tube, the model initially located MNPs at randomly generated distances no greater than 100 μm from the wall opposite the magnets. Each simulation run consisted of 100 nanoparticles, with the particle size distribution determined by data obtained using DLS (Figure 2b).

Using this model, it was predicted that magnetic nanoparticles within the size range of interest could indeed be manipulated in a size-dependent manner using flow through a magnetic field. Three conditions, with the tubing placed 7.5, 10.0, and 11.5 mm from the magnet pole face, were simulated with the fluid velocity and viscosity kept constant at 0.018 m/s and 1.005 mPa·s, respectively. This spacing was predicted to give three distinct size separations, as seen in Figure 2c–e. At a magnet distance of 7.5 mm, a majority of the nanoparticles with sizes between 50 and 100 nm would be in Fraction 1, while larger sized particles will be collected in Fraction 2. Comparatively, at a distance of 11.5 mm it is predicted that nanoparticles with sizes between 50 and 150 nm will be collected in Fraction 1 and the majority of nanoparticles between 200 and 400 nm will end up in Fraction 2. Based on these results, we then attempted to validate our model by replicating the simulation conditions experimentally.

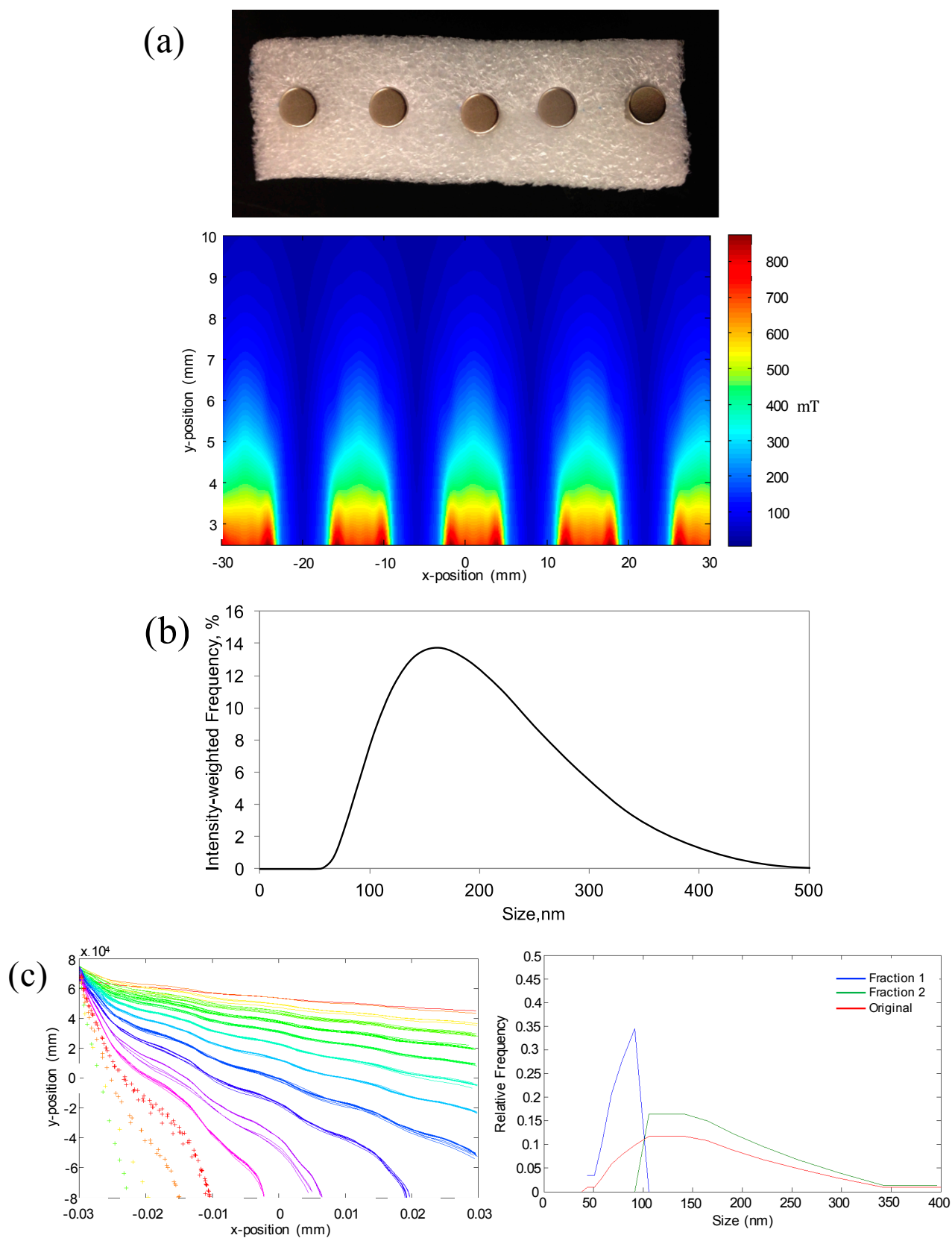


Figure 2. Cont.

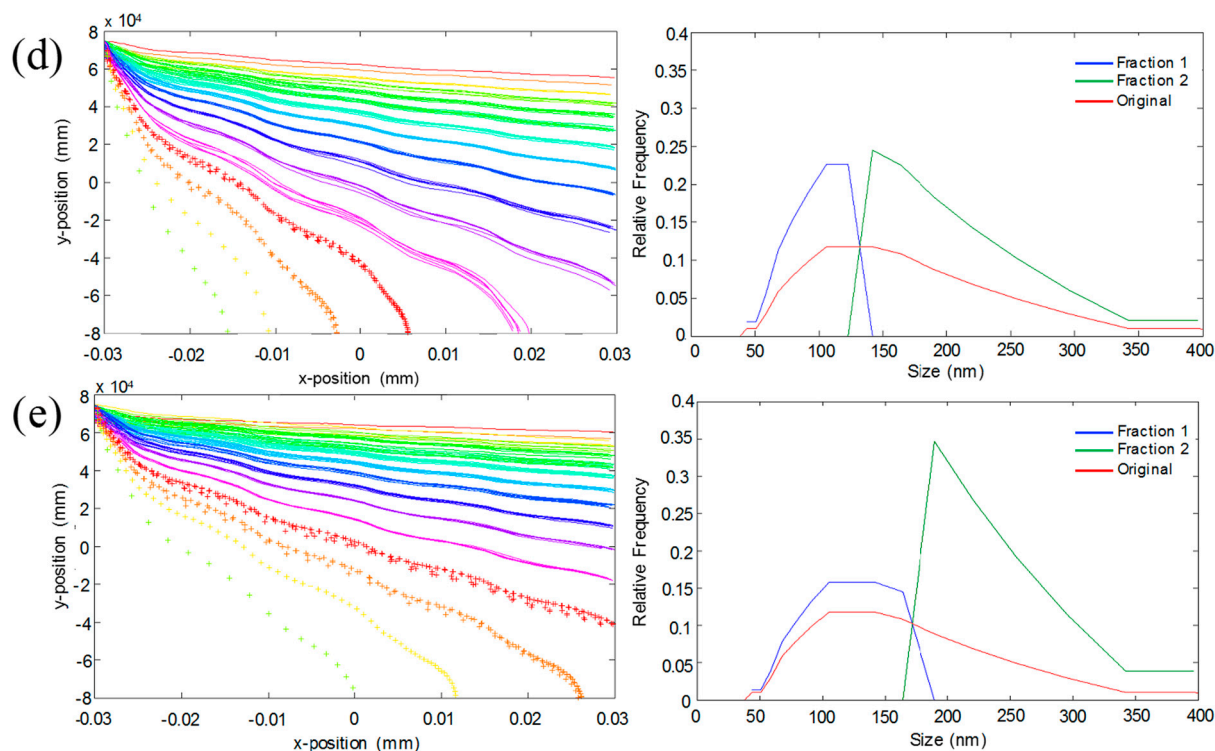


Figure 2. (a) Digital image of the sequence of magnets used for the simulation and validation experiments and the magnetic field map generated, using data from the manufacturer, for a series of five non-interacting ¼" diameter cylindrical magnets; (b) DLS size distribution of original iron oxide nanoparticle suspension; Predicted particle trajectories and resulting size distributions for original MNP (red), Fraction 1 (blue) and Fraction 2 (green) for magnet distances of (c) 7.5 mm; (d) 10 mm; and (e) 11.5 mm. Particle trajectory data sets based on MNP size of -44, -51, -59, -68, -79, -91, -106, -122, -142, -164, -190, -220, +255, +295, +342 and +396 nm.

3.2. Experimental Validation of the Mathematical Model

A magnetic separation prototype, as seen in Figure 3a, was developed to reproduce the conditions of the simulation. As with the mathematical model, 1.6 mm I.D. tubing was used to replicate the 2D channel and 100 µm I.D. tubing was used to inject MNPs into the mobile phase at the wall opposite the magnets. Similar to conditions used in the simulation, the magnetic block was placed at distances of 7.5, 10, and 11.5 mm away from the center of the tubing, and a steady fluid flow velocity of 0.018 m/s was maintained using two syringe pumps.

Repeating the simulated runs with the experimental setup, we obtained the samples pictured in Figure 3b. A clear visual difference was observed in the samples taken from Fraction 1 (left column) and Fraction 2 (right column) for the three runs that seemed to coincide with the predicted behavior. For example, in the case of the magnets placed 11.5 mm from the center of the tube (pictured top), it was predicted that a majority of the particles would be found in Fraction 1, with only the larger particles (>200 nm) being found in Fraction 2. Images in Figure 3b seem to agree with this result with the concentration in Fraction 1 apparently higher than that of Fraction 2, as evidenced by the increased coloration. Analysis of the samples using DLS, however, showed that all samples having sufficient

particle concentration for measurement (*i.e.*, the colored samples) possessed size distributions nearly identical to that of the original solution, as seen in Figure 3c–e. Samples not showing the yellow coloration (*i.e.*, Fraction 2 for 11.5 mm and Fraction 1 for 7.5 mm) were found to be too dilute to obtain a reliable DLS measurement.

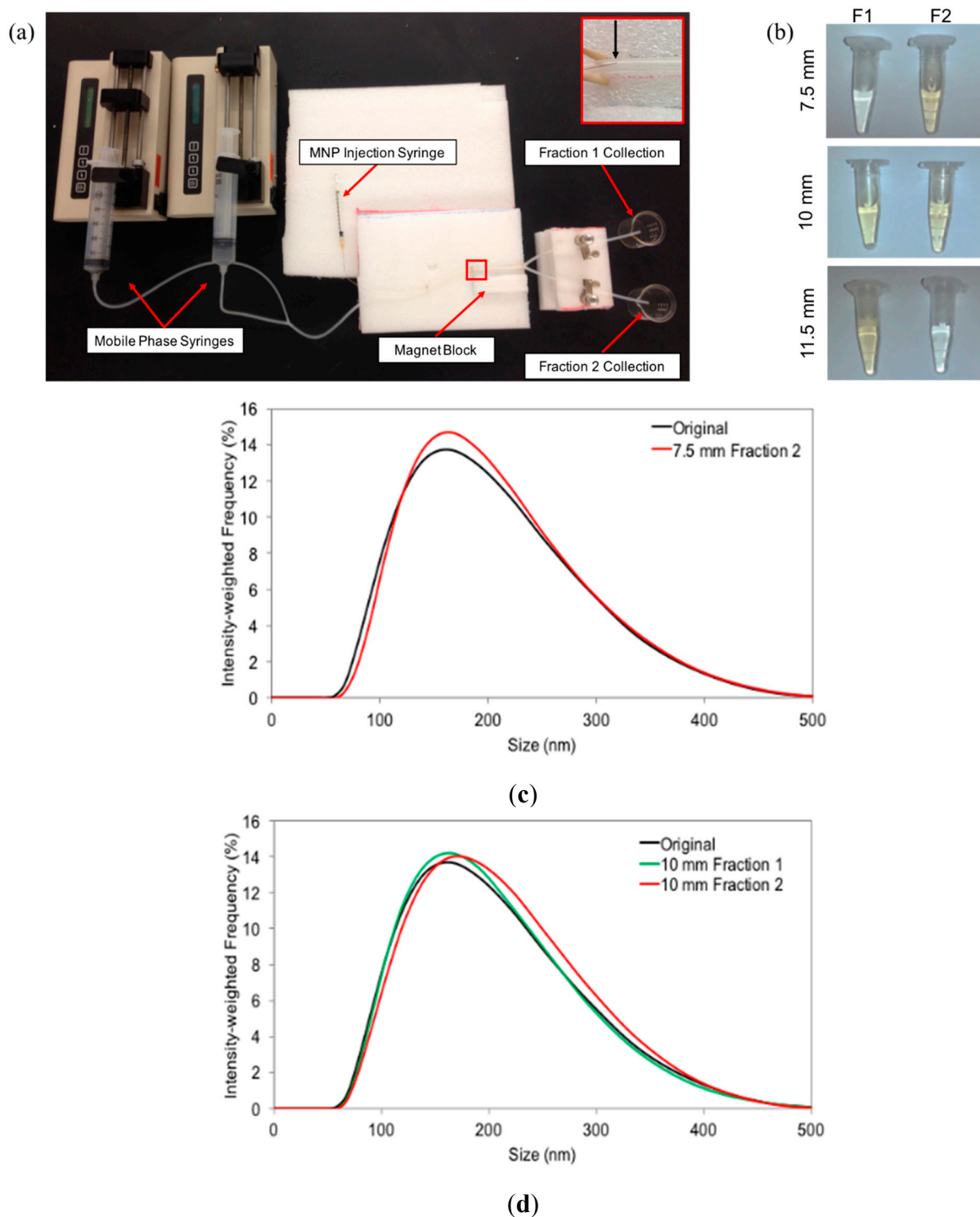
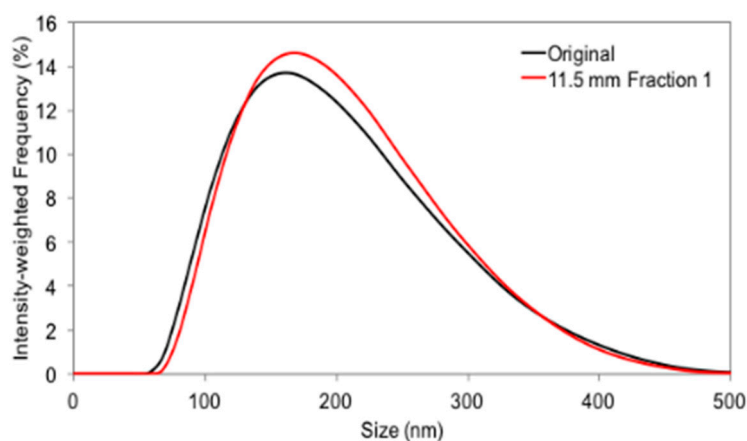


Figure 3. Cont.



(e)

Figure 3. (a) Digital image of magnetic separation prototype developed to replicate the conditions of the MATLAB simulation; (b) Digital image of Fraction 1 (**left**) and Fraction 2 (**right**) samples collected from the magnet distances of, from top to bottom, 11.5, 10, and 7.5 mm; (c–e) Size distributions of the obtained samples using distances of 7.5, 10, and 11.5 mm compared to that of the original MNP suspension.

As mentioned, the MATLAB simulation was created as a simple model of the proposed system and it therefore did not account for particle-particle interactions and used a system of magnets assumed to be non-interacting for simplicity. In reality, interactions between the magnets would certainly be present and would alter the magnetic forces experienced by MNPs. Additionally, it is well established that increasing particle concentrations lead to a decrease in inter-particle distance and an increase in particle–particle interactions [33]. In this study, the concentration of MNP suspension injected into the mobile phase was significantly concentrated to ensure final concentrations obtained were appropriate for DLS analysis. This resulted in the particles behaving as a ferro-fluid rather than individual particles and limited size-specific separation. Repetition of these studies at lower MNP concentrations, where particle-particle interactions would be minimized, on the other hand, yielded samples too dilute for characterization. Therefore, it was concluded that magnetic separation of particles suspended in a flow field is unlikely to produce the desired separation on a reasonable scale using this approach.

3.3. Successful Size-Selective Elution of Iron Oxide Nanoparticles from an Applied Magnetic Field

Due to the failure of the initial experiments, we then reversed the approach and used flow fields to elute MNPs that were held by a magnetic field. Since the magnetic force is dependent on nanoparticle size, the force required to counteract the magnetic force on two differently-sized MNPs will be lower for the smaller particle. In this case, the counteracting force is the fluid drag force, which is modulated by adjusting the flow rate of the mobile phase.

This was accomplished by creating a simple experimental setup, called the MagCoil, composed of a 18.5" length of 1/8" I.D. tubing wrapped around the entire 2" length of a Grade N42 diametrically magnetized neodymium cylinder (Model No.: ND039-0, Applied Magnets, Plano, TX, USA), as seen in Figure 4a. An inlet for both the MNP suspension and mobile phase were included at the top and a single outlet at the bottom was used for the collection of samples.

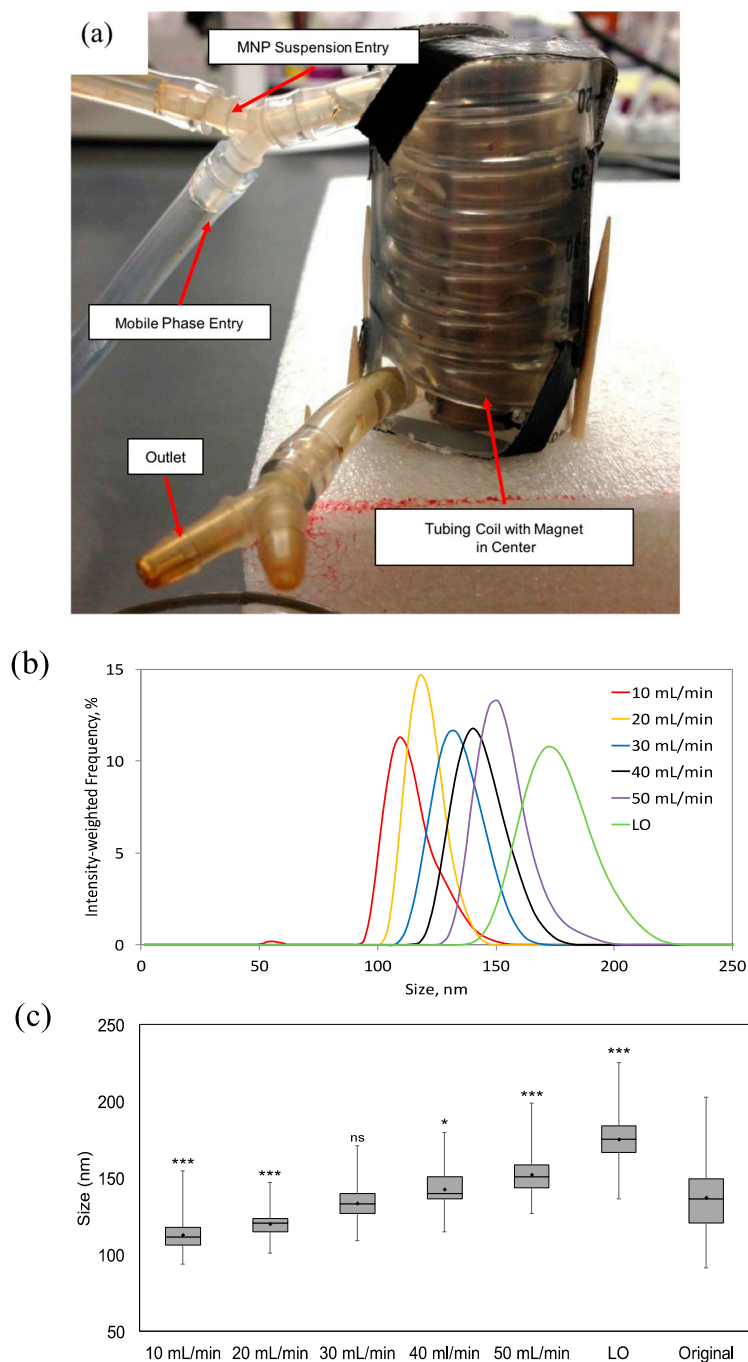


Figure 4. (a) Digital image of MagCoil magnetic separation prototype composed of 1/8" I.D. tubing wrapped around the length of a 2" diametrically magnetized cylinder encased in a plastic column for stability; (b) Average size distributions obtained using the MagCoil prototype and flow rates of 10, 20, 30, 40, and 50 mL/min, as well as the flushed particles (LO) calculated from the results of three separate experimental runs; (c) Box-and-whisker plot comparing the size distributions obtained using the MagCoil, at the varying flowrates, to the original size distribution. Horizontal lines indicate the mean diameter (nm), while the bar indicates standard deviation, and the vertical line the range. Significance determined using a two-tailed, two sample *t*-test ($n = 90$; *** $p < 0.001$; * $p < 0.05$; ns—not significant). The large sampling size of DLS (>100 k particle counts/s) leads to a statistically significant result between samples that would seem to be identical otherwise.

After filling the tubing with nanoparticle suspension and allowing them to reach a steady state level of accumulation at the inner wall of the tubing, an initial low flow rate of 0.25 mL/min was introduced to wash away any nanoparticles remaining suspended. DLS measurements of the recovered nanoparticles showed a size distribution similar to the original suspension of nanoparticles (data not shown). A series of increasing flow rates from 10 to 50 mL/min was then applied and samples collected using each of the flow rates for characterization. “Left over” particles, labeled “LO”, that remained in the MagCoil after application of the highest flow rate were then released by removing the magnet and again applying the 50 mL/min flow rate. All experiments were performed in triplicate and the resulting DLS measurements, shown in Figure 4b, are presented as the mean of three experiments. Figure 4c shows the mean hydrodynamic diameter, as well as the standard deviation, range and statistical significance, for each of the size distributions separated out of the original MNP suspension. Samples collected at flowrates of 10, 20, 40 and 50 mL/min and the LO sample, all were statistically different (at least $p < 0.05$) from the original suspension. While the 30 mL/min sample (133 ± 10 nm) could not be distinguished from the original sample (137 ± 21 nm), it should be noted that the separated sample has a four-fold smaller variance (σ^2). It should also be noted that while the DLS technique typically “counts” more than 100 k samples/s for several seconds, an n -value of 90 was used for statistical analysis.

To confirm the DLS measurements with TEM, samples were again collected with applied flow rates of 10, 40 mL/min, and LO. As shown in Figure 5a, DLS analysis of samples collected from the 10, 40 mL/min, and LO applied flow rates were found to be of size 96.3 ± 9.0 , 123.6 ± 7.9 , and 141.5 ± 10.8 nm, respectively. These samples were labeled as MNP-96, MNP-124, and MNP-142, respectively. TEM analysis was then performed to both confirm the occurrence of size-dependent separation of the original MNP suspension and for comparison with the obtained DLS results. Figure 5b shows a TEM image of the original suspension, designated as MNP-O. The average size of the original suspension was found to be 75.4 ± 47.7 nm using TEM compared to 137.2 ± 20.8 nm determined using DLS. It is important to note that apparent discrepancy in size is because TEM measurements provide the size of the core diameter while DLS measures the hydrodynamic diameter, which includes the core, surface coating, and any bound solvent. Representative images of each MNP-96, MNP-124, and MNP-142 are given in Figure 5c–e. Analysis of the TEM images showed the average core diameters to be 62.6 ± 27.2 , 80.7 ± 45.1 , and 104.6 ± 62.3 nm, respectively. A comparison of the measured sizes using both TEM and DLS are given in Table 1.

Table 1. Comparison of average hydrodynamic diameters measured using DLS and average core diameters determined using TEM for MNP-O, MNP-96, MNP-124, and MNP-142 distributions.

Sample	DLS (nm)	TEM (nm)
MNP-O	137.21 ± 20.8	75.4 ± 47.7
MNP-96	96.3 ± 9.0	62.6 ± 27.2
MNP-124	123.6 ± 7.9	80.7 ± 45.1
MNP-142	141.5 ± 10.8	104.6 ± 62.3

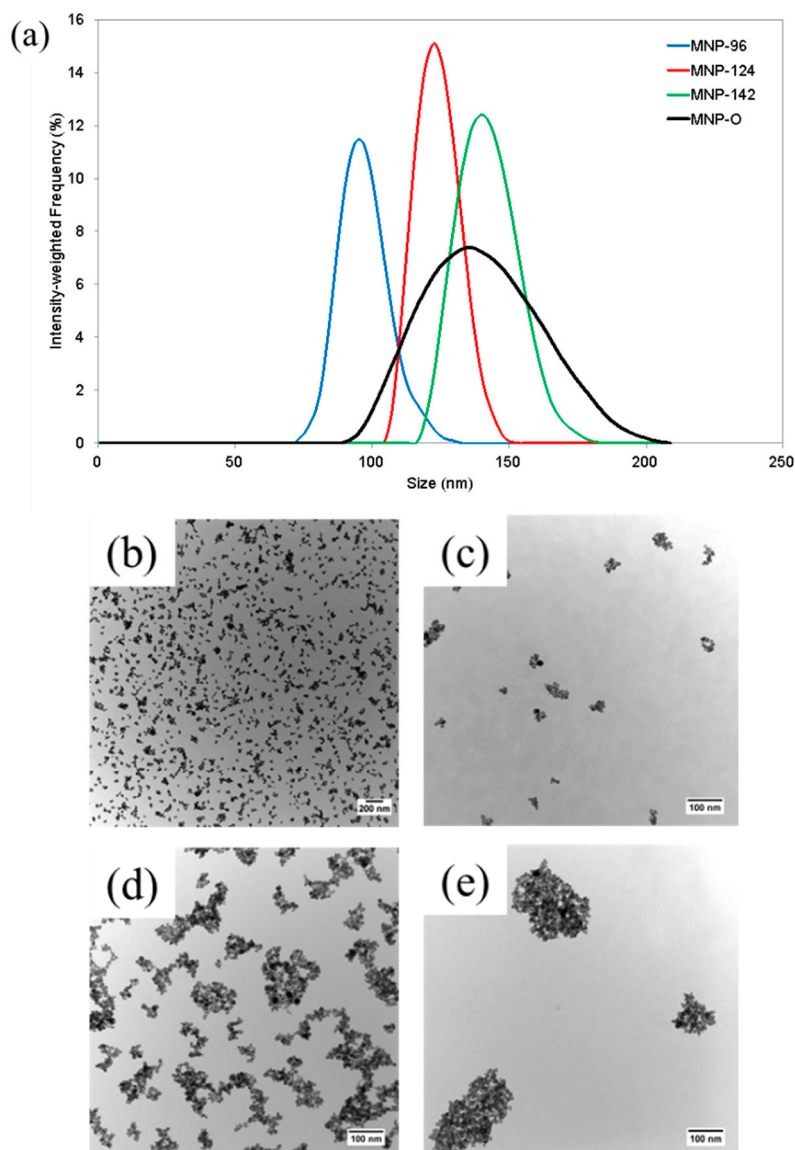


Figure 5. (a) Size distributions obtained from the original nanoparticle suspension (MNP-O) at flow rates of 10 mL/min (MNP-96), 40 mL/min (MNP-124), and LO (MNP-142); (b) Representative TEM image at 12.5 K magnification of original nanoparticle suspension, MNP-O, before separation; (c–e) Representative TEM images of MNP-96, MNP-124, and MNP-142 particle samples, respectively, at 85 K magnification.

3.4. Size-Dependent Relaxometric Properties of MNP Suspensions

The transverse relaxation time (T_2), which is the decay constant for the magnetization vector (M_t) perpendicular to the applied magnetic field in MRI, was used to characterize the magnetic properties of fractionated particles obtained using the mFFF approach. Tested samples included the original unseparated suspension (MNP-O; hydrodynamic diameter 137.2 ± 20.8 nm) and separated particles, designated MNP-95 and MNP-151, possessing average diameters of 94.8 ± 7.7 and 151.2 ± 11.2 nm, respectively. A series of dilutions were made of each sample and the relaxivities ($R_2 = 1/T_2$) of each sample determined by fitting of MRI data to the equation:

$$M_t = M_0 e^{-t/T_2} \quad (8)$$

Preliminary data, shown in Figure 6, indicates that as the average hydrodynamic diameter of the MNPs increased, the transverse proton relaxation time also increased. Considering the inverse relaxation times at the highest concentration used, the R_2 values increased from 11.2 to 51.05 s^{-1} as the MNP size increased from 95 to 151 nm. This size-dependent behavior is similar to that previously reported for magnetic particles of hydrodynamic sizes less than 100 nm [34]. Additionally, it is interesting to note that the R_2 values of the MNP-O samples, which contain particles of the same size as both MNP-95 and MNP-151, as well as sizes between the two distributions, were consistently between the R_2 values of MNP-95 and MNP-151. For example, the R_2 value for the MNP-O sample with an iron concentration of 0.009 mg/mL was determined to be 14.3 s^{-1} compared to the values of MNP-95 and MNP-151 at the same concentration of 5.2 and 27.87 s^{-1} , respectively.

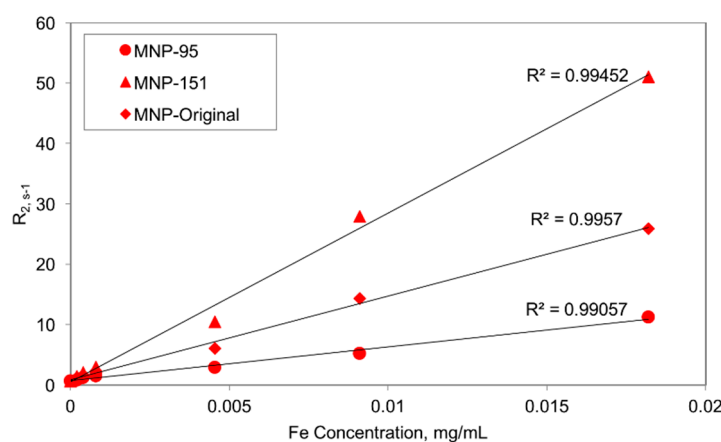


Figure 6. Transverse relaxivity R_2 values for the MNP-95, MNP-151, and MNP-O distributions with respect to iron concentration. R^2 values determined using linear trend line.

4. Experimental Section

4.1. Materials

fluidMAG-D (starch-coated magnetite (Fe_3O_4)) iron oxide nanoparticles (75 mg/mL) were obtained from Chemicell® GmbH (Berlin, Germany). Succinimidyl polyethylene glycol (mPEG-NHS) of molecular weight 5 kDa was obtained from Nanocs (New York, NY, USA). Dimethyl sulfoxide ($(\text{CH}_3)_2\text{SO}$, 99.9%) was obtained from BDH Chemicals. Epichlorohydrin ($\text{C}_3\text{H}_5\text{ClO}$, 99%) was obtained from Alfa Aesar (Ward Hill, MA, USA). Sodium hydroxide (NaOH , 97%) was obtained from BDH chemicals. Ferrozine iron reagent, monohydrate was obtained from J.T. Baker (Center Valley, PA, USA). Neocuproine hydrochloride monohydrate ($\text{C}_{14}\text{H}_{12}\text{N}_2 \cdot \text{HCl} \cdot \text{H}_2\text{O}$, 99%) was obtained from Acros. Ammonium acetate, ACS ($\text{CH}_3\text{COONH}_4$, 97% min) was obtained from Alfa Aesar. L-ascorbic acid ($\text{C}_6\text{H}_8\text{O}_6$) was obtained from BDH. Iron standard solution (1.00 mg/L as Fe) was obtained from HACH. Deionized water ($\text{DI-H}_2\text{O}$) was obtained using an ELGA PURELAB Flex water purification system.

4.2. Surface Modification of Iron Oxide Nanoparticles

The IO-MNPs were cross-linked, aminated, and PEGylated according to previously established methodology [35]. First, 2 mL of MNP suspension (42 mg/mL) was incubated with 2.6 mL 6 M NaOH for 15 min. Epichlorohydrin (1.3 mL) was then added and the mixture incubated for 24 h at 25 °C with shaking. After incubation, the solution was thoroughly dialyzed against DI-H₂O using a 8–10 kDa MWCO Float-A-Lyzer[®] G2 dialysis device (Spectrum Laboratories, Inc., Rancho Dominguez, CA, USA). The purified product was then incubated with 2 mL of concentrated NH₄OH (30% ammonia) for a period of 24 h at 25 °C with shaking. The aminated-MNP suspension was then sufficiently dialyzed against DI-H₂O and the final product was concentrated using a Sphero[™] Fleximag Separator (Spherotech, Lake Forest, IL, USA).

The PEGylation of the MNPs was achieved by utilizing NHS chemistry. First, 15 mg of mPEG-NHS was dissolved in a mixture of 320 µL of DMSO, 320 µL of DI-H₂O, and 320 µL of pH 8 phosphate buffer. 320 µL of aminated-MNP solution was then added and the mixture was incubated at 25 °C with shaking. At the completion of incubation, the solution was diluted to ~7 mL with DI-H₂O, placed on the magnetic separator, and then subjected to several washes with fresh DI-H₂O. After washing, the PEG-MNP solution was diluted to the final desired concentration.

4.3. Characterization of MNPs

Dynamic Light Scattering (DLS)—Dynamic light scattering was used to measure the intensity-weighted size (hydrodynamic diameter) distribution of nanoparticles. Measurements were taken in triplicate using a ZetaSizer Nano ZS90 sizing instrument (Malvern, Worcestershire, UK).

Transmission Electron Microscopy (TEM)—A Zeiss EM 10 TEM operating at a voltage of 60 kV was used to determine size distributions of MNPs. TEM samples were prepared by placing a single drop of a MNP solution onto a carbon type B, 300 mesh grid. The grid was then placed in a petri dish and allowed to dry at ambient conditions. Size distributions were obtained using ImageJ software to size a sufficient number of MNPs from multiple TEM images taken of each sample.

Iron Content Assay—The iron content of MNP solutions was determined using a ferrozine assay. Briefly, a 200 µL dilution (typically 1:1000) of the MNP sample was obtained in combination with 1 M HCl. 230 µL of KMnO₄/HCl was added to the sample and mixed via pipette. The KMnO₄/HCl solution was made by mixing equal volumes of 4.5% w/v KMnO₄ with 1.4 M HCl. The mixture was then incubated for 2 h at 60 °C followed by a 10 min cooling period. The sample was then mixed and transferred to a well plate via two 180 µL aliquots. Thirty microliters of prepared ferrozine solution was then added to the samples, mixed, and incubated at ambient conditions for 30 min. The prepared ferrozine solution was composed of 6.5 mM ferrozine, 6.5 mM neocuprine, 2.5 M ammonium acetate, and 1 M ascorbic acid dissolved in DI-H₂O. The absorbance of the samples at 550 nm was then measured using a SpectraMax i3 plate reader (Molecular Devices, Sunnyvale, CA, USA). Standard curves were created using an iron standard solution.

4.4. Magnetic Separation Prototype Operation

The magnetic separation prototype was created using styrofoam to create a block for the five cylindrical magnets and a platform for the tubing. 1/16" I.D. silicone tubing (VWR) was used to replicate the 2D channel in the simulation. 100 μm flexible fused silica capillary tubing (Molex, Lisle, IL, USA) was used to inject the nanoparticle solution into the mobile phase at the wall opposite the magnets. This tubing was connected to a 1 mL syringe fitted with a 30 G needle via a small section of 0.011" ID polyethylene tubing (Clay Adams, Sparks, MD, USA). The mobile phase was supplied by two syringe infusion pumps (KD Scientific, Holliston, MA, USA) in order to control the flow rate of the system.

For a typical run, the desired flow rate of the mobile phase was set to 0.036 mL/s using the syringe pumps and infusion was started. The concentrated nanoparticle suspension was then injected into the mobile phase by applying a small amount of pressure to the syringe plunger. The nanoparticle suspension was continually injected until the desired volume (approximately 0.1 mL) had been run through the magnetic separation prototype. After this, infusion of the mobile phase was terminated and the two obtained fractions were characterized. The whole system was flushed sufficiently with DI water to ensure no cross-contamination between runs.

4.5. Field-Flow Fractionation Prototype Operation

For all field-flow fractionation experiments, the desired volume of concentrated nanoparticle suspension was injected into 1/8" ID silicone tubing (VWR, Radnor, PA, USA) in the absence of flow from the mobile phase. The nanoparticles were then allowed to collect at the wall of the tubing closest to the magnet for a period of 15 min to allow for a steady-state distribution of particles at the tubing wall. The mobile phase was then introduced at a low initial flow rate using a peristaltic pump (Thermo Fisher Scientific, Waltham, MA, USA) in order to wash away any MNPs that had not collected at the tubing wall. After the entire volume of the silicone tubing was washed, flow from the pump was stopped, the sample volume was removed from the collection vessel for characterization, and then the collection vessel was rinsed with DI water and placed at the outlet. A higher flow rate was then introduced into the system and another sample was collected. This process was repeated for all desired flow rates supplied by the pump. Lastly, MNPs remaining in the tubing were removed by flushing with DI water after removal of the magnetic field.

4.6. Relaxometric Property Determination Using MRI

Relaxometry measurements were performed using a Siemens Verio Open-Bore 3T Scanner to determine the transverse proton relaxation times of solutions of iron oxide nanoparticles via spin-echo pulse sequences. For measurements of aqueous MNP solutions, samples were placed in either 0.6 or 1.6 mL plastic microfuge tubes and the tubes submerged in water spiked with copper sulfate (CuSO_4) to control background noise. The relaxation times of each sample were determined by plotting the magnitude of the measured MR signal at each of the echo times used in the spin-echo sequence and using a curve-fitting MATLAB script.

5. Conclusions

For the full potential of magnetic nanoparticles in nanomedicine to be realized, methods must be developed that allow for the distinct control of their physical and chemical properties so that particles may be optimized for specific applications. One of the most important factors that determines the behavior of magnetic nanoparticles *in vivo* is their size; however, current synthesis methods do not allow for sufficient size control for iron oxide nanoparticles of diameters greater than 30 nm. While initial Matlab simulations indicated that size-selective separation could be achieved by using magnetic fields to isolate MNPs from a liquid flow field, subsequent experiments were unable to confirm the results predicted by the model. Since a ferrofluid-type behavior was observed, the discrepancy between the theoretical and experimental results could be due to the assumption that particle-particle interactions were not significant within the model. Further improvements to both the model and the experimental setup are ongoing to validate this approach for the size-selective separation of magnetic nanoparticles. Despite this initial failing, an approach utilizing mechanisms similar to magnetic field-flow fractionation was found to be an effective method for the separation of polydisperse suspensions of iron oxide nanoparticles with diameters greater than 20 nm. While similar methods have been previously used to separate magnetic nanoparticles, there has been very little reported on the separation of particles in the size range of 50–400 nm. TEM and DLS analysis of particles obtained using this approach confirmed that particles of varying size and lower polydispersity can indeed be obtained within this size range.

An advantage of the magnetic separation approach used here is its simplicity and use of basic laboratory equipment, not requiring, for example, the special membranes required for cross-flow FFF. With a simple neodymium magnet, tubing, and a source of variable flow, this approach is easily adoptable to other laboratories. Ongoing studies are further refining the separation efficiency and scaling-up the approach to generate higher concentration of particles required for *in vivo* studies. These studies and further optimization of the system presented in these investigations could allow for the production of very narrow size distributions of magnetic nanoparticles within the size range relevant for biomedical applications in a very simple and economic manner. This could substantially improve the potential for clinical translation of these particles by enabling the fundamental studies necessary to understand the disposition of these particles *in vivo*.

Acknowledgments

Hunter B. Rogers is a recipient of a fellowship from the Alabama EPSCoR Graduate Research Scholars Program. This material is also partially supported by the National Science Foundation under Grant No. EPS-1158862 Subagreement 34-21530-200-76190, by a Department of Defense FY2012 Prostate Cancer Research Program (PCRP) Idea Development Award (Grant #PC120946), and by a grant from the Auburn University Research Initiative in Cancer (AURIC). Additionally, Tareq Anani has been partially supported by an AURIC Graduate Fellowship.

Author Contributions

Hunter B. Rogers and Allan E. David conceived and designed the experiments; Hunter B. Rogers, Tareq Anani, Ronald J. Beyers and Young Suk Choi performed the experiments; Hunter B. Rogers, Ronald J. Beyers and Allan E. David analyzed the data; Hunter B. Rogers and Allan E. David wrote the paper.

Conflicts of Interest

The authors declare no conflict of interest.

References

1. Freitas, R.A., Jr. *Nanomedicine, Volume I: Basic Capabilities*; Landes Bioscience: Georgetown, TX, USA, 1999.
2. Kim, B.Y.S.; Rutka, J.T.; Chan, W.C.W. Nanomedicine. *N. Engl. J. Med.* **2010**, *363*, 2434–2443.
3. Cho, K.; Wang, X.; Nie, S.; Shin, D. Therapeutic nanoparticles for drug delivery in cancer. *Clin. Cancer Res.* **2008**, *14*, 1310–1316.
4. Lee, J.H.; Jun, Y.W.; Yeon, S.I.; Shin, J.S.; Cheon, J. Dual-mode nanoparticle probes for high-performance magnetic resonance and fluorescence imaging of neuroblastoma. *Angew. Chem.* **2006**, *118*, 8340–8342.
5. Doane, T.L.; Burda, C. The unique role of nanoparticles in nanomedicine: Imaging, drug delivery and therapy. *Chem. Soc. Rev.* **2012**, *41*, 2885–2911.
6. Moghimi, S.M.; Hunter, A.C.; Murray, J.C. Nanomedicine: Current status and future prospects. *FASEB J.* **2005**, *19*, 311–330.
7. Choi, H.; Liu, W.; Misra, P.; Tanaka, E.; Zimmer, J.; Ipe, B.; Bawendi, M.; Frangioni, J. Renal clearance of quantum dots. *Nat. Biotechnol.* **2007**, *25*, 1165–1170.
8. Hillaireau, H.; Couvreur, P. Nanocarriers' entry into the cell: Relevance to drug delivery. *Cell. Mol. Life Sci.* **2009**, *66*, 2873–2896.
9. Moghimi, S.; Porter, C.; Muir, I.; Illum, L.; Davis, S. Non-phagocytic uptake of intravenously injected microspheres in rat spleen: Influence of particle size and hydrophilic coating. *Biochem. Biophys. Res. Commun.* **1991**, *177*, 861–866.
10. Fang, C.; Shi, B.; Pei, Y.; Hong, M.; Wu, J.; Chen, H. *In vivo* tumor targeting of tumor necrosis factor- α -loaded stealth nanoparticles: Effect of MePEG molecular weight and particle size. *Eur. J. Pharm. Sci.* **2006**, *27*, 27–36.
11. Perrault, S.D.; Walkey, C.; Jennings, T.; Fischer, H.C.; Chan, W.C. Mediating Tumor Targeting Efficiency of Nanoparticles Through Design. *Nano Lett.* **2009**, *9*, 1909–1915.
12. Gao, J.; Gu, H.; Xu, B. Multifunctional magnetic nanoparticles: Design, synthesis, and biomedical applications. *Acc. Chem. Res.* **2009**, *42*, 1097–1107.
13. Thorek, D.L.; Chen, A.K.; Czupryna, J.; Tsourkas, A. Superparamagnetic iron oxide nanoparticle probes for molecular imaging. *Ann. Biomed. Eng.* **2006**, *34*, 23–38.

14. Laurent, S.; Forge, D.; Port, M.; Roch, A.; Robic, C.; Vander Elst, L.; Muller, R.N. Magnetic iron oxide nanoparticles: Synthesis, stabilization, vectorization, physicochemical characterizations, and biological applications. *Chem. Rev.* **2008**, *108*, 2064–2110.
15. Gupta, A.K.; Naregalkar, R.R.; Vaidya, V.D.; Gupta, M. Recent advances on surface engineering of magnetic iron oxide nanoparticles and their biomedical applications. *Nanomedicine* **2007**, *2*, 23–39.
16. Josephson, L.; Rudin, M. Barriers to clinical translation with diagnostic drugs. *J. Nucl. Med.* **2013**, *54*, 329–332.
17. Lavik, E.; von Recum, H. The role of nanomaterials in translational medicine.pdf. *ACS Nano* **2011**, *5*, 3419–3424.
18. Wang, Y.X. Superparamagnetic iron oxide based MRI contrast agents: Current status of clinical application. *Quant. Imaging Med. Surg.* **2011**, *1*, 35–40.
19. Hufschmid, R.; Arami, H.; Ferguson, R.; Gonzales, M.; Teeman, E.; Brush, L.; Browning, N.; Krishnan, K. Synthesis of phase-pure and monodisperse iron oxide nanoparticles by thermal decomposition. *Nanoscale* **2015**, *7*, 11142–11154.
20. Hyeon, T. Chemical synthesis of magnetic nanoparticles. *Chem. Commun.* **2003**, *8*, 927–934.
21. Park, J.; An, K.; Hwang, Y.; Park, J.-G.; Noh, H.-J.; Kim, J.-Y.; Park, J.-H.; Hwang, N.-M.; Hyeon, T. Ultra-large-scale syntheses of monodisperse nanocrystals. *Nat. Mater.* **2004**, *3*, 891–895.
22. Gu, L.; Fang, R.; Sailor, M.; Park, J. *In vivo* clearance and toxicity of monodisperse iron oxide nanocrystals. *ACS Nano* **2013**, *6*, 4947–4954.
23. Vickrey, T.M.; Garcia-Ramirez, J.A. Magnetic field-flow fractionation: Theoretical basis. *Sep. Sci. Technol.* **1980**, *15*, 1297–1304.
24. Bi, Y.; Pan, X.; Chen, L.; Wan, Q.-H. Field-flow fractionation of magnetic particles in a cyclic magnetic field. *J. Chromatogr. A* **2011**, *1218*, 3908–3914.
25. Carpino, F.; Moore, L.; Chalmers, J.; Zborowski, M.; Williams, P. Quadrupole magnetic field-flow fractionation for the analysis of magnetic nanoparticles. *J. Phys. Conf. Ser.* **2005**, *17*, 174–180.
26. Latham, A.H.; Freitas, R.S.; Schiffer, P.; Williams, M.E. Capillary magnetic field flow fractionation and analysis of magnetic nanoparticles. *Anal. Chem.* **2005**, *77*, 5055–5062.
27. Moeser, G.D.; Roach, K.A.; Green, W.H.; Alan Hatton, T.; Laibinis, P.E. High-gradient magnetic separation of coated magnetic nanoparticles. *AIChE J.* **2004**, *50*, 2835–2848.
28. Ditsch, A.; Lindenmann, S.; Laibinis, P.E.; Wang, D.I.; Hatton, T.A. High-gradient magnetic separation of magnetic nanoclusters. *Ind. Eng. Chem. Res.* **2005**, *44*, 6824–6836.
29. Beveridge, J.; Stephens, J.; Williams, M. Differential magnetic catch and release: Experimental parameters for controlled separation of magnetic nanoparticles. *Analyst* **2011**, *136*, 2564–2571.
30. Bird, R.; Stewart, W.; Lightfoot, E. *Transport Phenomena*; John Wiley & Sons: Hoboken, NJ, USA, 1960.
31. Shevkoplyas, S.S.; Siegel, A.C.; Westervelt, R.M.; Prentiss, M.G.; Whitesides, G.M. The force acting on a superparamagnetic bead due to an applied magnetic field. *Lab Chip* **2007**, *7*, 1294–1302.
32. Berg, H. *Random Walks in Biology*; Princeton University Press: Princeton, NJ, USA, 1993.
33. Kourki, H.; Famili, M.H.N. Particle sedimentation: Effect of polymer concentration on particle–particle interaction. *Powder Technol.* **2012**, *221*, 137–143.

34. Roca, A.G.; Veintemillas-Verdaguer, S.; Port, M.; Robic, C.; Serna, C.J.; Morales, M.P. Effect of nanoparticle and aggregate size on the relaxometric properties of MR contrast agents based on high quality magnetite nanoparticles. *J. Phys. Chem. B* **2009**, *113*, 7033–7039.
35. Cole, A.J.; David, A.E.; Wang, J.; Galbán, C.J.; Hill, H.L.; Yang, V.C. Polyethylene glycol modified, cross-linked starch-coated iron oxide nanoparticles for enhanced magnetic tumor targeting. *Biomaterials* **2011**, *32*, 2183–2193.

© 2015 by the authors; licensee MDPI, Basel, Switzerland. This article is an open access article distributed under the terms and conditions of the Creative Commons Attribution license (<http://creativecommons.org/licenses/by/4.0/>).